

AD-A085 725

SCIENCE APPLICATIONS INC EL SEGUNDO CALIF
AIRBLAST ATTENUATION EXPERIMENTS FOR THE M-X TRENCH. (U)

F/G 18/3

DEC 78 D T HOVE, J E CRAIG

DNA001-77-C-0280

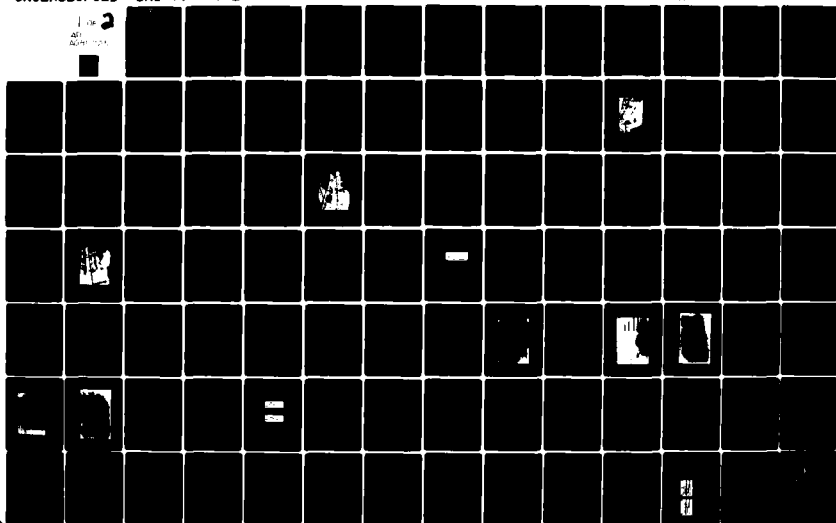
UNCLASSIFIED

SAI-79-546-LA

DNA-4677T

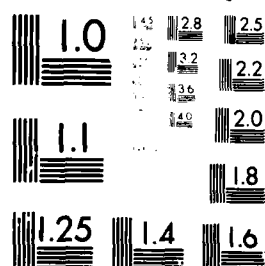
NL

1 of 2
AD-A085 725



1 OF 2

AD
A085725



MICROCOPY RESOLUTION TEST CHART
NATIONAL BUREAU OF STANDARDS 1963-A

LEVEL III

(12)
P.S.

AP-E 300798

DNA 4677T

AIRBLAST ATTENUATION EXPERIMENTS FOR THE M-X TRENCH

Science Applications, Inc.
101 Continental Boulevard, Suite 310
El Segundo, California 90245

31 December 1978

Topical Report for Period 5 July 1977-31 December 1978

CONTRACT No. DNA 001-77-C-0280

APPROVED FOR PUBLIC RELEASE;
DISTRIBUTION UNLIMITED.

THIS WORK SPONSORED BY THE DEFENSE NUCLEAR AGENCY
UNDER RDT&E RMSS CODES B344077462 H35HAXSX35540 AND
B344078462 H35KAXSX35521 H2590D.

DTIC
ELECTE
JUN 20 1980
S D

Prepared for
Director
DEFENSE NUCLEAR AGENCY
Washington, D. C. 20305

80 4 28 112

ADA 085725

DDC FILE COPY

Destroy this report when it is no longer
needed. Do not return to sender.

PLEASE NOTIFY THE DEFENSE NUCLEAR AGENCY,
ATTN: STTI, WASHINGTON, D.C. 20305, IF
YOUR ADDRESS IS INCORRECT, IF YOU WISH TO
BE DELETED FROM THE DISTRIBUTION LIST, OR
IF THE ADDRESSEE IS NO LONGER EMPLOYED BY
YOUR ORGANIZATION.



UNCLASSIFIED

SECURITY CLASSIFICATION OF THIS PAGE (When Data Entered)

REPORT DOCUMENTATION PAGE		READ INSTRUCTIONS BEFORE COMPLETING FORM
1. REPORT NUMBER DNA 4677T ✓	2. GOVT ACCESSION NO. AD-A085 725	3. RECIPIENT'S CATALOG NUMBER
4. TITLE (and Subtitle) AIRBLAST ATTENUATION EXPERIMENTS FOR THE M-X TRENCH		5. TYPE OF REPORT & PERIOD COVERED Topical Report for Period 5 Jul 77—31 Dec 78
		6. PERFORMING ORG. REPORT NUMBER SAI-79-546-LA ✓
7. AUTHOR(s) Duane T. Hove James E. Craig		8. CONTRACT OR GRANT NUMBER(s) DNA 001-77-C-0280 ✓
9. PERFORMING ORGANIZATION NAME AND ADDRESS Science Applications, Inc. ✓ 101 Continental Boulevard, Suite 310 El Segundo, California 90245		10. PROGRAM ELEMENT, PROJECT, TASK AREA & WORK UNIT NUMBERS Subtask H35HAXSX355-40 Subtask H35KAXSX355-21
11. CONTROLLING OFFICE NAME AND ADDRESS Director Defense Nuclear Agency Washington, D.C. 20305		12. REPORT DATE 31 December 1978
		13. NUMBER OF PAGES 150
14. MONITORING AGENCY NAME & ADDRESS (if different from Controlling Office)		15. SECURITY CLASS (of this report) UNCLASSIFIED
		15a. DECLASSIFICATION/DOWNGRADING SCHEDULE
16. DISTRIBUTION STATEMENT (of this Report) Approved for public release; distribution unlimited.		
17. DISTRIBUTION STATEMENT (of the abstract entered in Block 20, if different from Report)		
18. SUPPLEMENTARY NOTES This work sponsored by the Defense Nuclear Agency under RDT&E RMSS Codes B344077462 H35HAXSX35540 and B344078462 H35KAXSX35521 H2590D.		
19. KEY WORDS (Continue on reverse side if necessary and identify by block number) M-X Trench Airblast Shock Propagation Ducts Laser Optics		
20. ABSTRACT (Continue on reverse side if necessary and identify by block number) A series of experiments were performed in the NASA Ames Electric Arc Shock Tube to investigate the propagation of strong shock waves in tubes with trans- verse ribs. The experiments were designed to measure shock attenuation, end wall reflected pressures, wall drag and flowfield structure to provide a basis for development of computer models for analysis of blast wave propagation in the M-X trench.		

UNCLASSIFIED

SECURITY CLASSIFICATION OF THIS PAGE (When Data Entered)

UNCLASSIFIED

SECURITY CLASSIFICATION OF THIS PAGE(When Data Entered)

20. ABSTRACT (Continued)

Shock attenuation was found to be dependent on shock strengths but apparently not strongly dependent on rib design. Entrance region effects appeared to play a strong role in the attenuation; no effect of flow Reynolds number was observed. Laser shadowgrams and interferograms revealed a complex two-dimensional flowfield in the vicinity of the shock with no indication of fully developed pipe flow seven diameters behind the shock. Wall drag measurements exceeded estimates from steady flow theory; a simple wave drag model gave estimates somewhat closer to the measurements. End wall measurements were initially higher than expected from conventional reflection factors presumably due to the nonuniform flowfields.

Test data should be applicable to the prototype trench since scale effects were not observed. Two-dimensional flowfield calculations are required to understand the entrance region and shock attenuation process. Design tools developed for prototype assessment should be able to predict the experimental shock wave time of arrival, strength attenuation, and waveforms.

Accession For	
NTIS GRA&I	<input checked="checked" type="checkbox"/> <input type="checkbox"/> <input type="checkbox"/>
DDC TAB	
Unannounced	
Justification	
By	
Distribution/	
Availability Codes	
Dist.	Avail and/or special
A	

UNCLASSIFIED

SECURITY CLASSIFICATION OF THIS PAGE(When Data Entered)

PREFACE

This program was conducted for the Defense Nuclear Agency under contract DNA001-77-C-0280 to provide experimental data on shock attenuation in the M-X trench. The effort was sponsored by the Strategic Structures Division of the Shock Physics Directorate and was performed during the period 5 July 1977 to 31 December 1978. Dr. George Ullrich was the DNA Technical Representative.

The SAI Program Manager was Duane Hove. Dr. James Craig conducted the shock tube tests and performed the data analysis. Dr. Raad Issa developed the one-dimensional computer code used for test predictions, and Dr. Kenneth Haines directed the optical measurements team.

We are grateful to Dr. Robert Dannenberg of the NASA Ames Research Center for continuing cooperation and suggestions.

TABLE OF CONTENTS

	<u>Page</u>
PREFACE	1
LIST OF FIGURES	4
LIST OF TABLES	6
NOMENCLATURE	7
1.0 INTRODUCTION	9
1.1 Objectives	10
1.2 Scope	10
2.0 DESIGN REQUIREMENTS	11
2.1 M-X Trench Configuration	11
2.2 Shock Propagation	11
2.2.1 Empirical Prediction Methods	13
2.2.2 One-Dimensional Computational Models	14
2.2.3 Two-Dimensional Computational Models	16
2.3 Experimental Requirements	17
3.0 SHOCK TUBE TEST PROGRAM	19
3.1 Facility Description	19
3.2 Models and Instrumentation	27
3.3 Data Recording and Processing	40
3.4 Test Matrix	40
4.0 EXPERIMENT RESULTS	44
4.1 Pressure Waveforms	44
4.2 Shock Attenuation	47
4.2.1 Reynolds Number Effect on Shock Attenuation	51
4.2.2 Shock Strength and Rib Geometry Effects on Shock Attenuation	54

TABLE OF CONTENTS (CONT'D)

	Page
4.3 Optical Flowfield Measurements.	59
4.4 Wall Drag	69
4.5 End Wall Reflected Pressures.	72
4.6 Shock Attenuation Comparison with Predictions .	75
5.0 SUMMARY.	79
5.1 Conclusions	79
5.2 Recommendations	80
6.0 REFERENCES	82
APPENDIX A.	A-1
APPENDIX B.	B-1
APPENDIX C.	C-1

LIST OF FIGURES

	<u>Page</u>
Figure 1. M-X trench design	12
Figure 2. Resistance formula for rough pipes.	15
Figure 3. East facility	20
Figure 4. NASA Ames electric arc shock tube schematic .	21
Figure 5. Arc heated driver	22
Figure 6a. Shock tube schematic.	24
Figure 6b. Shock tube x-t diagram.	24
Figure 7. Shock tube performance for 1.36 meter cylindrical driver.	26
Figure 8. Shock attenuation test arrangement.	29
Figure 9. Rib geometries.	30
Figure 10. Pressure transducer mounting.	31
Figure 11a. Initial entrance region design.	32
Figure 11b. Final entrance region design.	32
Figure 12. Pressure transducer stations.	34
Figure 13. Load cell arrangement	35
Figure 14. Optical test section.	37
Figure 15. Optical port in test section.	38
Figure 16. Optical test arrangement.	39
Figure 17. Sample pressure waveform (26.2 atm/div and 500 μ sec/div)	45
Figure 18. Typical pressure histories.	46
Figure 19. Shock TOA for M-X ribs ($P_{21} = 80$)	48
Figure 20. Shock TOA for DD&M ribs ($P_{21} = 80$).	49

LIST OF FIGURES (CONT'D)

	<u>Page</u>
Figure 21. Shock TOA for M-X ribs ($P_{21} = 700$)	50
Figure 22. Shock attenuation by M-X ribs	52
Figure 23. Reynolds number effect on shock attenuation.	53
Figure 24. Shock attenuation at $P_{21_i} = 80$	55
Figure 25. Shock attenuation at $P_{21_i} = 300$	56
Figure 26. Shock attenuation at $P_{21_i} = 700$	57
Figure 27. Shock attenuation from preliminary tests	58
Figure 28. Laser shadowgram of shock/rib interactions	60
Figure 29. The main features of the shock propagation	62
Figure 30. Holographic interferogram of shock/rib interactions	63
Figure 31. Density profile one rib spacing behind shock ($\rho_1 = 9.03 \times 10^{-4}$ gm/cm ³)	64
Figure 32. Laser Shadowgram of quasi-steady flow	66
Figure 33. Holographic interferogram of quasi-steady flow	67
Figure 34. Density profiles in the quasi-steady flow ($\rho_1 = 9.03 \times 10^{-4}$ gm/cm ³)	68
Figure 35. M-X liner load histories (10 Klbs/div x 1.0 msec/div)	70
Figure 36. End wall pressure measurements	73
Figure 37. End wall pressure measurements	74
Figure 38. Comparison of Porzel model with typical data set	77
Figure 39. One dimensional RIST code predictions.	78

LIST OF TABLES

	<u>Page</u>
Table 1. Shock attenuation test conditions.	42
Table 2. Optical test series.	43
Table 3. Load cell measurements	71

NOMENCLATURE

A	Sound speed
C_S	Shock velocity
C_f	Friction coefficient
D	Tube diameter
E	Energy
k	Roughness height
L	Length
m	Molecular weight
M	Mach number
P	Pressure
Pr	Prandtl number
R	Tube radius
R	Dimensionless velocity at roughness height
Re_D	Reynolds number based on diameter
S	Spacing
St	Stanton number
T	Temperature
U	Velocity
V	Volume
X	Distance
γ	Ratio of specific heats
Γ	Acoustic impedance
ν	Kinematic viscosity
ρ	Fluid density
τ	Shear stress

Subscripts

i	Initial
s	Sandgrain or shock
w	Wall
1,2,3,4	Shock tube region defined in Figure 6
∞	Freestream

1.0 INTRODUCTION

As an alternative to fixed based concepts, the USAF is considering locating an advanced missile (M-X) in multiple trench bases to increase the ability of the force to survive preemptive attack. Success of this approach relies on designing a cost effective basing system with sufficient hardness to nuclear attack such that an aggressor would have to exhaust his arsenal to achieve assured destruction.

Airblast from a nuclear weapon presents a critical design environment for the M-X trench. Blast waves will propagate in the trench due to loading during the cratering process, due to loading of a previously breached trench or due to a burst in the trench. The latter case presents the most severe attack, albeit the least likely. Airblast loading could be particularly acute if the trench acts as a shock tube thereby extending (in the absence of significant attenuation) the range to a given overpressure beyond the usual spherical shock range. Thus, it is important to understand the propagation of a blast wave in the trench to insure that airblast does not impose excessive loads on the missile.

A number of phenomena will attenuate the blast wave as it propagates in the trench. Among these are wall ablation, heat transfer and momentum (shear) loss to the walls, shock interactions with trench wall ribs, wall expansion and venting. Trench airblast environments were predicted by numerical code calculations primarily by Allen Kuhl of TRW (Reference 1) and Charles Needham of AFWL (Reference 2). Kuhl modeled the effects of wall shear, expansion and venting in a pseudo one-dimensional calculation while Needham performed two-dimensional calculations of the shock interactions with internal ribs.

Models and assumptions in the codes must be verified by experiment to gain confidence in the predictions. One-dimensional calculations are convenient and inexpensive to run but ignore the physics involved in two-dimensional shock interactions and

thin boundary layers. Two-dimensional finite difference calculations on the other hand do not include the effects of viscosity. Since both approaches were being used to predict the airblast environment in the trench, an experimental program was undertaken as a baseline for evaluating the two methods.

Experimental data for shock propagation in ribbed tubes was nonexistent in the literature at the outset of this study, and only limited data were available for sandgrain roughened tubes at lower shock strengths than of interest to MX. In the formulation phase of the present program, some square rib shock attenuation tests performed by TRW and Martin Marietta (Reference 3) came to our attention. Questions as to the adequacy of these experiments were addressed in the present study.

1.1 Objectives

The present program was undertaken to provide shock attenuation test data in ribbed tubes for evaluation of computer code predictions. Specific tests were designed to investigate the influence of Reynolds number, shock strength and rib design on shock attenuation. End wall reflected pressure measurements were made to determine the effect of the ribs on the blast plug loads.

As the program progressed, it became apparent that additional diagnostic measurements were necessary to resolve issues surfacing in the airblast modeling community. Consequently, the program was expanded to measure the wall drag and to provide an optical description of the flowfield behind the shock.

1.2 Scope

A shock tube test program was conducted at the NASA Ames Research Center Electric Arc Shock Tube. To aid in test design, a one-dimensional shock propagation computer code was developed. Test sections were fabricated, instrumentation (including custom built diagnostics for wall drag and optical measurements) was assembled, and approximately 65 test runs were conducted.

2.0 DESIGN REQUIREMENTS

M-X trench vulnerability to nuclear attack was dictated by the need to provide adequate protection for the missile against the airblast environment. Vulnerability assessments require the confident prediction of airblast propagation within the trench, and a test program was undertaken to provide a baseline for evaluation of computer code models.

2.1 M-X Trench Configuration

The proposed M-X trench system consists of a number of unmanned mobile transporters making random concealed movements in long trenches (tubes) below ground. Airblast protection within the trench is achieved by means of blast plugs carried along by the transporter, and the design of these plugs is a pacing item for the trench concept. The baseline M-X trench design consists of a 4 meter (13 feet) diameter fiber reinforced concrete cylinder with 0.15 meter (0.5 feet) high internal ribs spaced 1.5 meters (5 feet) center-to-center (Figure 1). The ribs provide reaction support for the airblast plug as well as attenuation of the airblast. Missile launch is achieved by erecting the missile canister through the roof, and the concrete cylinder has longitudinal and transverse joints to ease the breakout process. The joints provide strength only in compression; the roof is held in place by the mass of the concrete wall and the soil overburden.

2.2 Shock Propagation Analyses

System performance studies indicate that the blast plug must survive a shock environment of 4×10^6 Pascals (600 psi) which occurs for a 1 MT surface burst at a range of 565m (1800 feet). In the

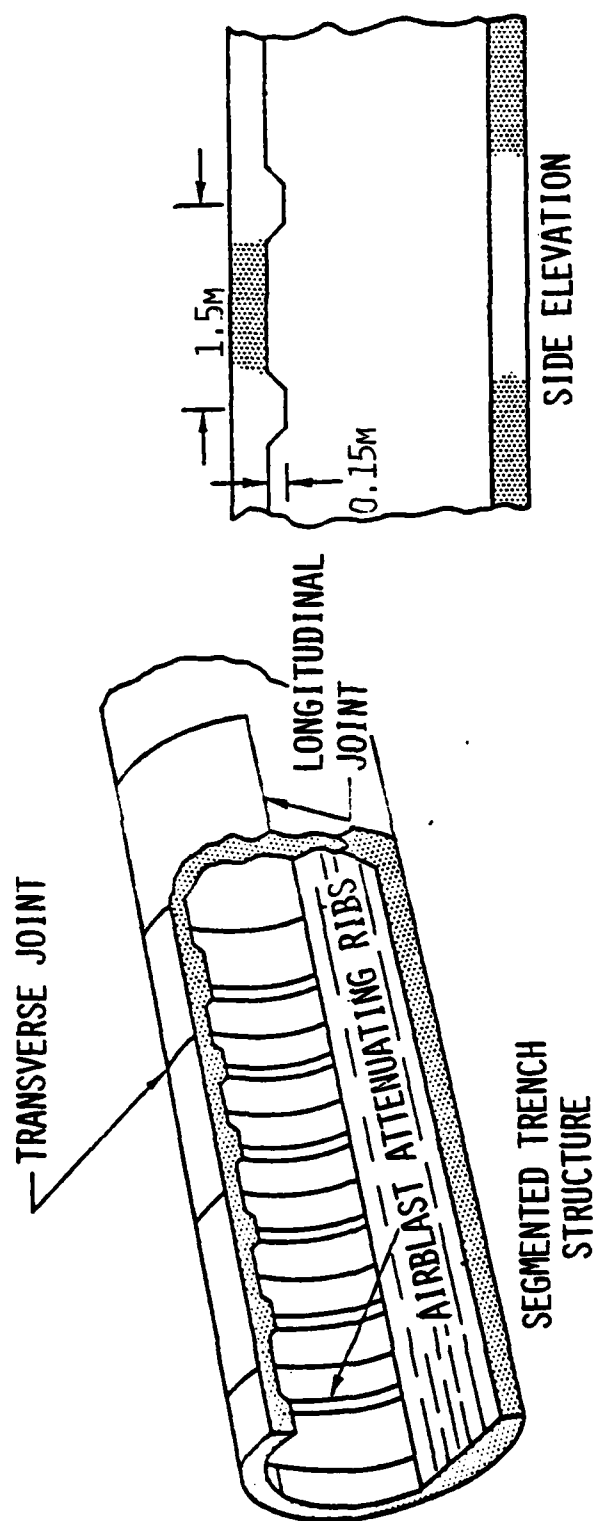


FIGURE 1. MX TRENCH DESIGN.

strong shock region near a nuclear burst on or in the trench massive wall ablation produces significant shock attenuation. Wall expansion and venting are important contributors to shock attenuation at high and intermediate shock strengths. At lower shock strengths (say, $\Delta p \leq 6.8 \times 10^6$ Pascals), shock interactions with the ribs further reduce the shock strength. High shock strength attenuation is being addressed in other DNA analytical and experimental programs. The present discussion is concerned with the latter case, (i.e., shock propagation in a rigid tube with internal ribs).

2.2.1 Empirical Prediction Methods

A number of shock tube experiments had been conducted at low shock strengths in sand-roughened tubes primarily to investigate attenuation mechanisms for air entrainment systems. Simplified models were developed and used to correlate the test data, perhaps the most well known being due to Porzel (Reference 4). Skjeltop offered a more elaborate empirical formulation (Reference 5), and Schiffman (Reference 3) correlated the TRW data with a modified version of these approaches.

The problem with these empirical models (as with most such approaches) is that the models were fine tuned to match a specific set of data, and are unsuccessful when addressing problems outside the range of parameters for which they were formulated. Rough wall attenuation of shocks in a tube is far from a trivial problem. Earlier modeling efforts were too simplified and led Kriebel (Reference 6) to conclude, for example, "--- from the foregoing comparison of theories --- the predicted attenuation of a shock front due to tube wall friction differs widely for both smooth-walled tubes and rough-walled tubes."

2.2.2 One-Dimensional Computational Models

Shock propagation models have been assembled by Kuhl at TRW (Reference 1) and as part of this program which assume that the flow is one-dimensional and quasi-steady (fully developed pipe flow). The shock attenuation mechanisms invoked are wall friction and heat transfer. Solutions are obtained by numerically solving the mass, momentum and energy conservation equations.

The SAI one-dimensional model is embodied in the RIST code (Reference 7) which was used to make pretest predictions. The code solves the appropriate conservation equations using the FLIC method, and friction and convective heat transfer laws are obtained from steady flow models. Schlichting (Reference 8) presents the friction coefficients ($\lambda = 4C_f$) of Nikuradse (Figure 2) which indicate that for high pipe Reynolds number Re_D and large sandgrain roughness k_s , the friction coefficient C_f is independent of Reynolds number. Under MX prototype conditions ($Re_D \sim 10^9$ and $R/k \sim 13$) the wall resistance formula for the completely rough regime

$$C_f = \frac{1}{4 \left(2 \log \frac{R}{k_s} + 1.74 \right)^2} \quad (1)$$

would be expected to apply. For the transverse ribs in the MX trench, an equivalent sandgrain roughness

$$\frac{k_s}{k} = \exp \left(\frac{8.5 - R}{2.5} \right) \quad (2)$$

and R is determined from empirical curves of Dalle-Donne and Meyer (Reference 9).

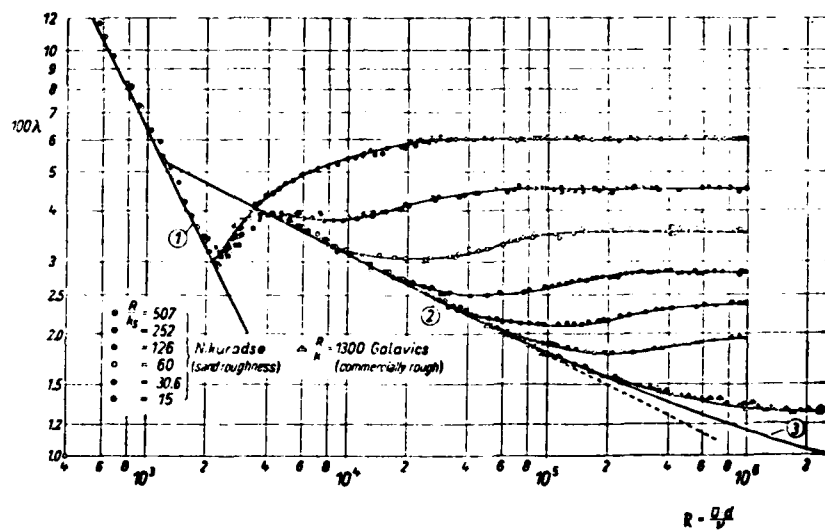


FIGURE 2. RESISTANCE FORMULA FOR ROUGH PIPES.

Heat transfer to the wall is defined in terms of a Stanton number for which Dirling's compressible flow model was chosen (Reference 10). Expressed in terms of a modified Reynolds analogy

$$\frac{St}{(C_f/2)} = \left\{ 1 + \left(\frac{T_w}{T_\infty} \frac{C_f}{2} \right)^{\frac{1}{2}} \left[5.19 (h_{ws}^+)^{0.2} Pr^{0.44} - 8.5 \right] \right\}^{-1} \quad (3)$$

where

$$h_{ws}^+ = \frac{k_s \sqrt{\tau_w / \rho_w}}{v_w} \quad (4)$$

is a roughness Reynolds number evaluated at the wall.

Whether a one-dimensional model is adequate depends to a great extent on whether the wall boundary closes the tube (fully developed pipe flow). According to Mirels (Reference 11), the shock boundary layer for a smooth wall MX trench requires a distance of 140 diameters whereas a smooth wall shock tube of 0.1 meter diameter requires 50 diameters. Roughness will increase the boundary layer growth rate, but the effect of large protuberances such as the MX ribs on the boundary layer is unknown.

2.2.3 Two-Dimensional Computational Models

The two dimensional finite difference HULL code (Reference 12) has been used by Needham at the Air Force Weapons Laboratory to calculate the airblast environment in an MX trench. HULL solves the finite difference analogs of a system of partial differential equations describing an inviscid, nonconducting fluid. A two-dimensional cylindrical geometry was used to represent the MX trench, and a 6.8×10^7 Pascal overpressure shock waveform from a 1 MT surface burst was input at the trench entrance (Reference 2).

The HULL code calculation revealed a complicated two dimensional flow structure due to shock interaction with the

ribs, and the shock decayed more rapidly than an equivalent free air burst. Shock attenuation was caused by the nonisentropic conversion of kinetic energy to thermal energy and the redistribution of axial momentum into radial components. The influence of viscosity on these calculations has not been determined.

2.3 Experimental Requirements

Since the one-dimensional and two-dimensional models treat different physical mechanisms, it was necessary to provide a means of evaluating the approaches. The philosophy adopted was to obtain a set of experimental data for a well described flowfield and scaled geometry as a test for the computer codes. Thus, if a code could adequately predict the experimental results, confidence would be gained in the prototype predictions.

Small scale experiments can be directly useful to prototype assessments if it can be shown that the scale either does not influence the test results or can be accounted for. For a geometrically scaled test model, the model size enters through the nondimensional Reynolds number. Skin friction, for example, is usually Reynolds number dependent; however, for rough tubes at sufficiently high Reynolds number, the skin friction is Reynolds number independent. Thus, determining the influence (or lack thereof) of Reynolds number was a test requirement.

Shock attenuation rates were found to be a function of shock strength by TRW and Martin for tubes with internal ribs and by Porzel for sandgrain roughened tubes. Therefore, a requirement of the experiments was to perform the tests from as high an initial shock strength as possible down to an initial shock strength of 40 (equivalent of a 600 psi shock). To maintain high Reynolds numbers and absolute shock pressures, tests were to be conducted as near ambient initial pressure as practical. Since the ribs were expected to perturb the flow, end

wall reflected pressure measurements were required to estimate the load history on the M-X blast plug.

The primary rib geometry for the experiments was to be the nominal MX design (Figure 1). However, it was also of interest to determine if the rib configuration could be optimized to provide increased attenuation. The empirical skin friction correlation of Dalle Donne and Meyer indicated that the M-X rib separation distance was well chosen but that increased drag could be achieved (in steady flow) by increasing the height to width ratio. A second rib geometry was built to test this hypothesis.

Details of the shock wave flowfield were deemed necessary to understand the physics of the shock wave attenuation process. For the one-dimensional models, the question of appropriate wall drag models and the state of the boundary layer were controversial and required experimental investigation. In addition, a qualitative picture of the rib/flowfield interaction was necessary to guide the development of one and two-dimensional models.

3.0 SHOCK TUBE TEST PROGRAM

A series of shock tube experiments were conducted at the NASA Ames Research Center Electric Arc Shock Tube (EAST) to aid in the understanding of airblast propagation in the MX trench. The facility was selected because of its ability to produce strong, repeatable shock waves at ambient or near ambient initial pressures.

Test sections containing removable liners with internal ribs were attached to the EAST facility and tested at three initial shock strengths after facility calibration tests. Blast plug load histories were obtained from pressure measurements on a rigid end wall located at the end of a ribbed test section. The nominal instrumentation consisted of time of arrival (TOA) probes and high frequency pressure transducers. In addition, custom built diagnostics were developed to determine the loads on a floating wall element and to provide optical measurements of the rib/flowfield interactions.

3.1 Facility Description

The NASA Ames Research Center EAST facility (Figure 3) is an electric arc shock tube used for high energy shock physics experiments. EAST consists of a 1.2 MJ capacitor bank, an 0.1 meter I.D. shock tube and a dump tank (Figure 4). For the present tests a 1.36 meter long cylindrical driver was employed.

Strong shocks are created by discharging energies approaching 1 MJ into a driver section through an exploding wire technique. Joule heating of the driver gas takes place when an arc is struck along the wire path between the ground electrode at the diaphragm station and the high voltage electrode at the base of the driver (Figure 5). Alternate gases such as helium are used in the driver section to create stronger shocks than would occur with air in the driver. Details of the driver operation can be found in References 13 and 14.

ELECTRIC ARC SHOCK TUBE FACILITY



AMES RESEARCH CENTER

FIGURE 3. EAST FACILITY.

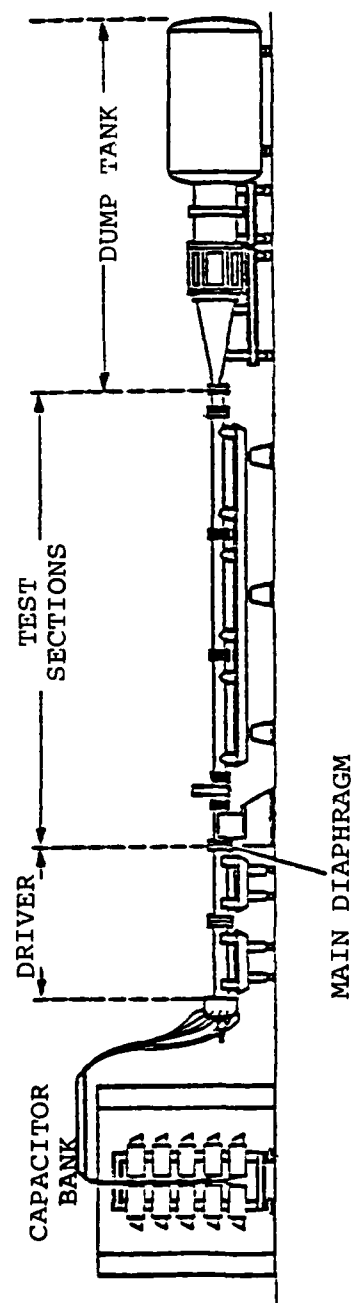
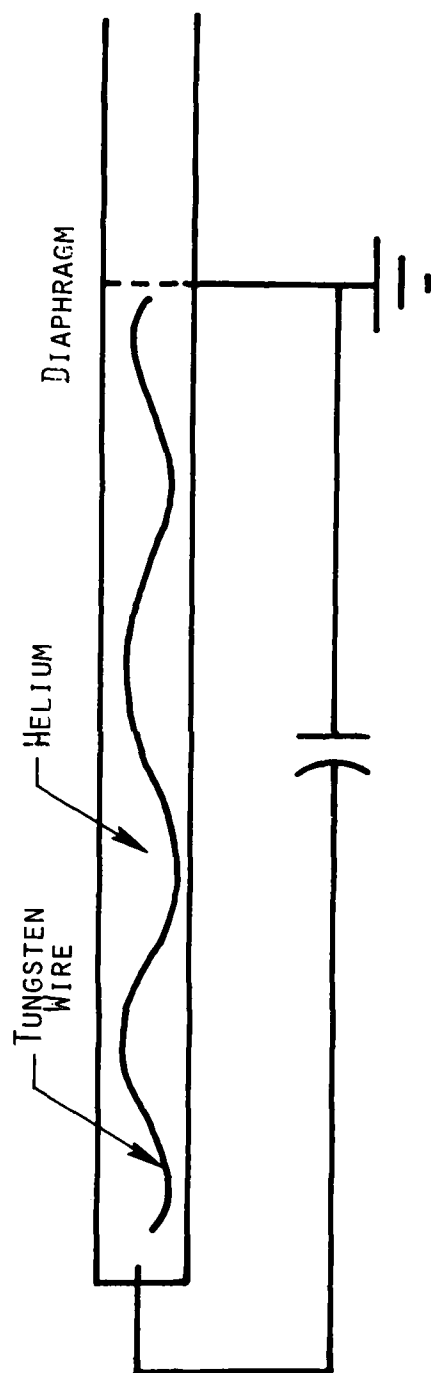


FIGURE 4. NASA AMES ELECTRIC ARC SHOCK TUBE SCHEMATIC.



CAPACITOR BANK

$C = 1520 \mu\text{FARADS}$
 VOLTAGE = 0 - 40. K VOLT
 ENERGY = 0 - 1.2 M JOULE

FIGURE 5. ARC HEATED DRIVER.

Operation of the shock tube is easily illustrated by considering a constant diameter tube divided into two regions: a high pressure driver section and a lower pressure driven section separated by a diaphragm (Figure 6a). When the diaphragm is burst, a shock wave propagates down the driven section, and an expansion fan propagates back into the driver section (Figure 6b). The expansion fan converts the stagnation energy of the driver gas into flow energy of the expanded driver gas and the work done in compressing and accelerating the driven gas. Expansion waves travel at the speed of sound relative to the local driver gas conditions; thus the driver gas sound speed is an important parameter in creating strong shocks. References 15 and 16 present the details of shock tube performance.

Using the notation of Figure 6, the ideal shock Mach number is determined from

$$P_{41} = \frac{1 + \frac{2\gamma_1}{\gamma_1 + 1} (M_s^2 - 1)}{\left(1 - \frac{(\gamma_4 - 1)(M_s^2 - 1)}{(\gamma_1 + 1) A_{41}^2 M_s^2} \right)^{\frac{2\gamma_4}{\gamma_4 - 1}}} \quad (5)$$

where A is sound speed and the double subscript implies a ratio. The shock pressure ratio or strength is

$$P_{21} = \frac{2\gamma_1}{\gamma_1 + 1} (M_s^2 - 1) + 1 \quad (6)$$

Driver gas (Region 4) state after arc discharge is estimated from constant volume heating for ideal gases

$$P_{41} = T_{41} = 1 + (\gamma_4 - 1) \left(\frac{E}{VP_{4i}} \right) \quad (7)$$

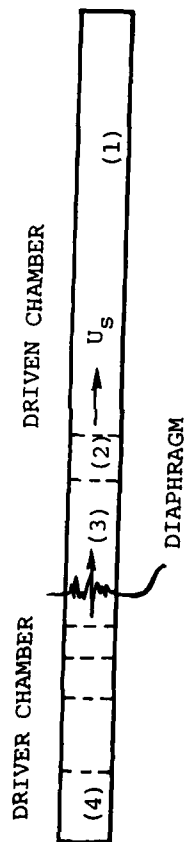


FIGURE 6A. SHOCK TUBE SCHEMATIC,

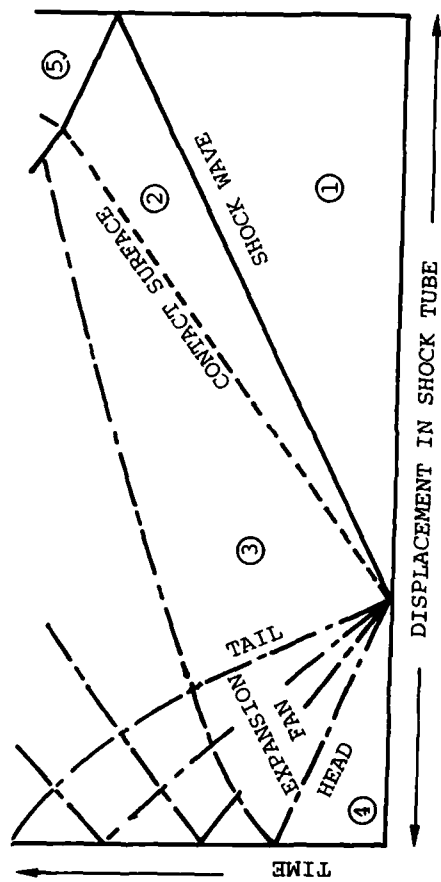


FIGURE 6B. SHOCK TUBE X-T DIAGRAM.

$$A_{41} = \left(\frac{\gamma_{41}}{m_{41}} T_{41} \right)^{\frac{1}{2}} \quad (8)$$

where m is the molecular weight. Equations 5 through 8 were used to estimate the shock tube performance; final test conditions (Figure 7) were determined from calibration runs.

Velocity and state variables behind the shock wave (Region two) are found from the initial state of the driven tube gas and the shock Mach number

$$\frac{U_2}{A_1} = \frac{2}{\gamma_1 + 1} \left(\frac{M_s^2 - 1}{M_s} \right) \quad (9)$$

$$\rho_{21} = \frac{(\gamma_1 + 1) M_s^2}{(\gamma_1 - 1) M_s^2 + 2} \quad (10)$$

$$T_{21} = \frac{\left[2\gamma_1 M_s^2 - (\gamma_1 - 1) \right] \left[(\gamma_1 - 1) M_s^2 + 2 \right]}{(\gamma_1 + 1)^2 M_s^2} \quad (11)$$

Reynolds number based on diameter in region two is

$$Re_{2D} = \frac{\rho_{21} \left(\frac{U_2}{A_1} \right)^2}{T_{21} \left(M_s - \frac{U_2}{A_1} \right)} \left(\frac{\rho_1}{\rho_{STP}} \right) \left(\frac{\rho_1 A_1 D}{\mu_1} \right)_{STP} \quad (12)$$

where STP refers to standard conditions, and the viscosity is taken as proportional to temperature.

Since velocity and pressure are constant across the contact surface, conditions in Region three are found from the initial state of the driver gas and the velocity in Region 3.

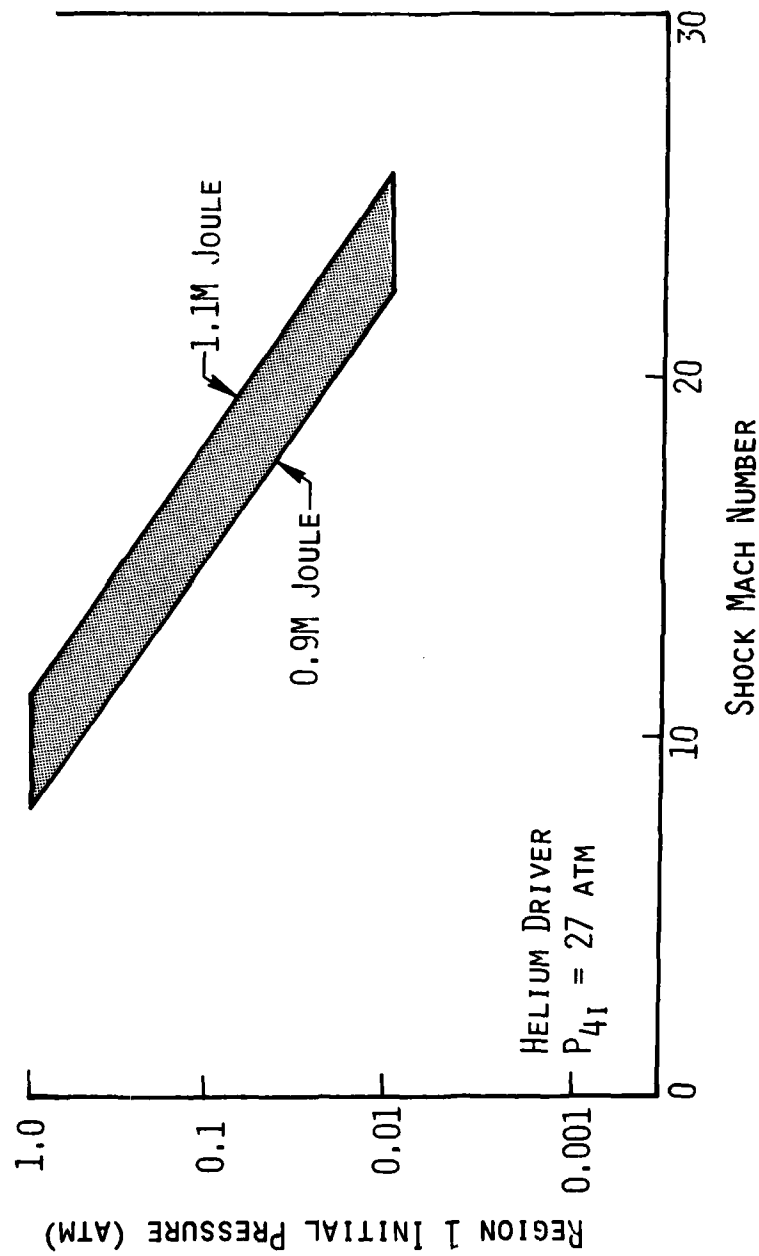


FIGURE 7. SHOCK TUBE PERFORMANCE FOR 1.36 METER CYLINDRICAL DRIVER.

$$A_{34} = 1 - \frac{(\gamma_4 - 1)}{2} \frac{U_2}{A_1} \frac{A_1}{A_4} \quad (13)$$

$$T_{34} = (A_{34})^2 \quad (14)$$

$$\rho_{34} = (A_{34})^{\frac{2}{\gamma_4 - 1}} \quad (15)$$

The Region 3 Reynolds number is

$$Re_{3D} = \frac{\left(\frac{\rho_4}{\rho_{STP}}\right) \rho_{34} \left(\frac{U_3}{A_4}\right)}{\left(\frac{T_4}{T_{STP}} \cdot T_{34}\right)^{\frac{1}{2}} \left(\frac{\rho_4 A_4 D}{\mu_4}\right)_{STP}} \quad (16)$$

Equations 12 and 16 were used to estimate the flow Reynolds number for scaling considerations.

Since the contact surface follows closely behind the shock wave for high shock strength flows, Region 3 gases occupy the test section for a large portion of the test. Communication of the effects of the ribs on Region 3 gases to the shock is controlled by the acoustic impedance ratio across the contact surface

$$\Gamma_{32} = \rho_{32} A_{32} \quad (17)$$

If Γ is near one acoustic signals are transmitted intact, if Γ is largely different from one the signals can be weakened ($\Gamma > 1$) or amplified ($\Gamma < 1$).

3.2 Models and Instrumentation

Two test sections were constructed for airblast attenuation experiments. Cylindrical 4142 steel seamless tubes 0.18 meter

(7 inch) O.D. by 0.13 meter (5 inch) I.D. were bolted to the EAST facility via existing flanges threaded onto the steel tubing. Figure 8 shows a single 3.1 meter (10 feet) long test section in place for the initial attenuation experiments; the final experiments were run with a 5.5 meter (18 feet) test section.

Interchangable liners with internal ribs were inserted into the shock tube test sections. The internal diameter of the liners (rib tops) matched the NASA shock tube smooth wall diameter (10 cm) to avoid an abrupt area change. Two sets of liners were tested (Figure 9): one set was a 1/39 scale (based on diameter) replica of the proposed MX rib geometry (referred to as MX), and one set was an attempt to optimize shock attenuation via the Dalle Donne and Meyer skin friction correlations within the MX rib height constraints (referred to as DD&M).

Pressure measurements were made along the test section primarily at the rib tops; a few rib valley measurements indicated no significant differences. Pressure transducers were mounted in steel inserts in the sidewall to protect them from liner/wall relative motion. Because the mountings were wider than the individual ribs, the space between two ribs was filled in at the transducer locations (Figure 10).

Several initial tests were conducted to provide information for an MX interchange meeting; the test arrangement consisted of 2.4 meters (8 feet) of MX ribs followed by 0.6 meters (2 feet) of smooth wall. The MX ribs began at the shock tube interface (Figure 11a), and the first pressure station was 0.3 meters (1 foot) from the first rib. The initial tests indicated a dramatic drop in shock strength by the time the shock had traversed the 8 ribs to the first pressure transducer. To investigate this entrance region effect the second test section was modified, and the remainder of the tests were conducted with a pressure transducer downstream of the first rib (Figure 11b).

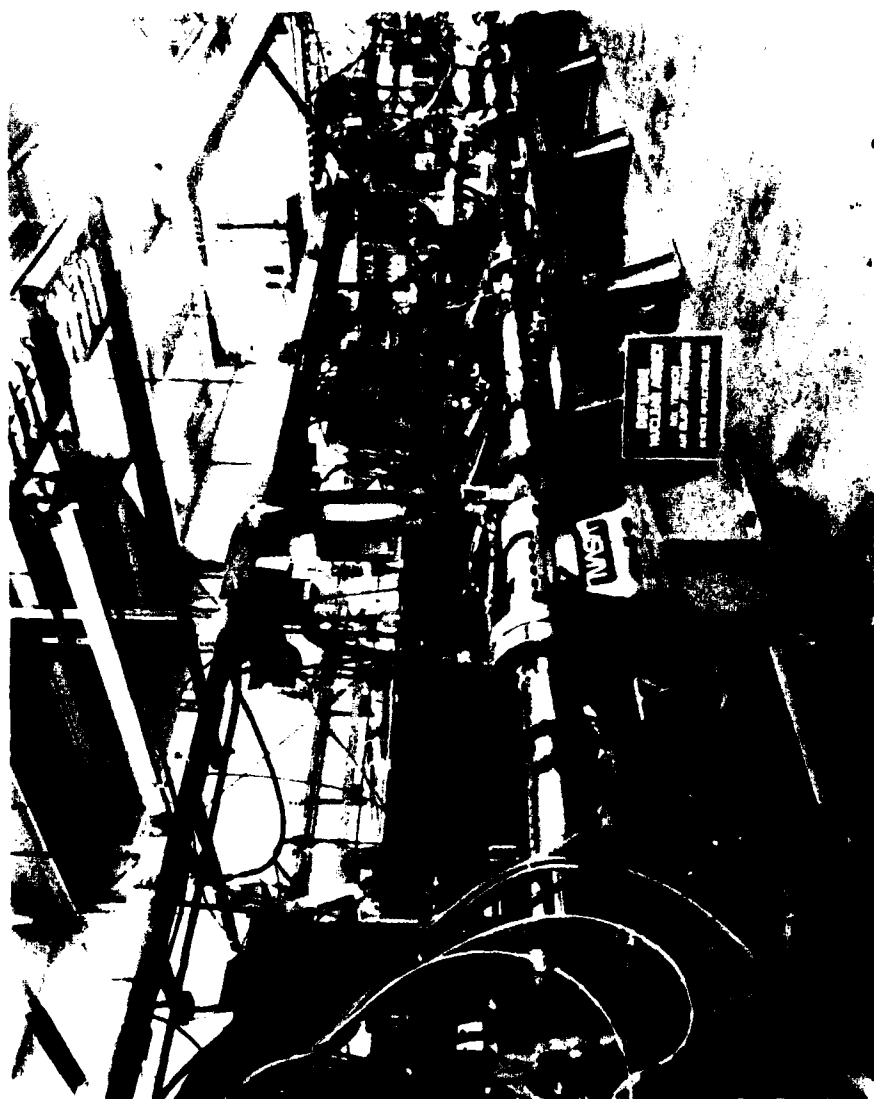
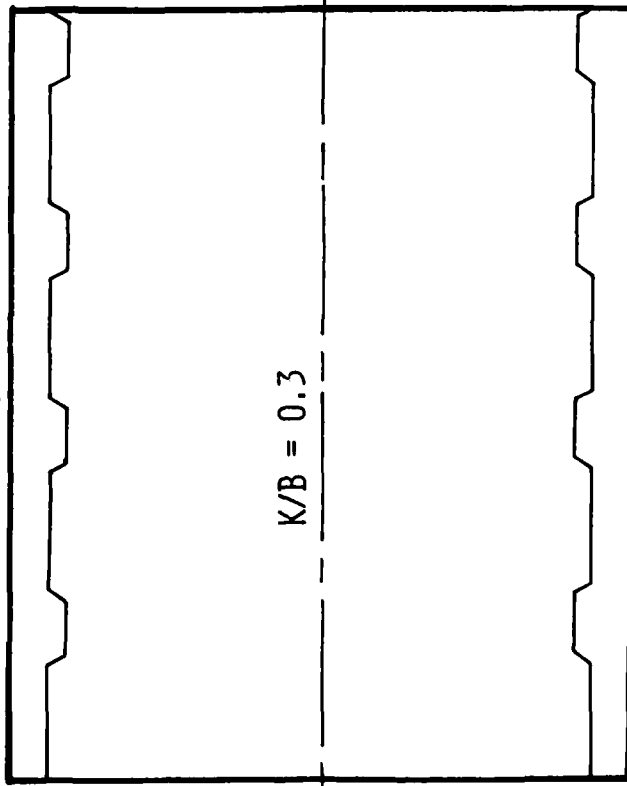


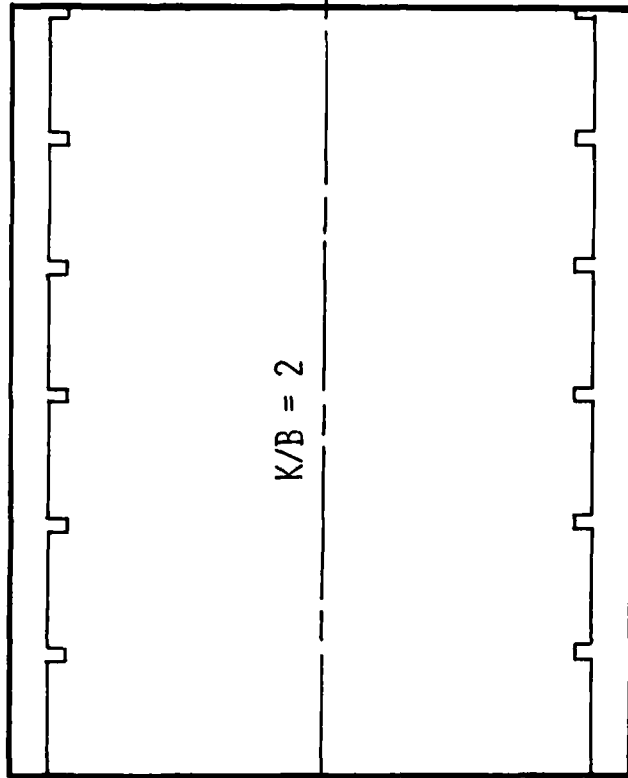
FIGURE 8. SHOCK ATTENUATION TEST ARRANGEMENT

MX
 $K/D = 0.038, S/D = 0.375$



$K/B = 0.3$

DD&H
 $K/D = 0.038, S/D = 0.257$



$K/B = 2$

FIGURE 9. RIB GEOMETRIES.

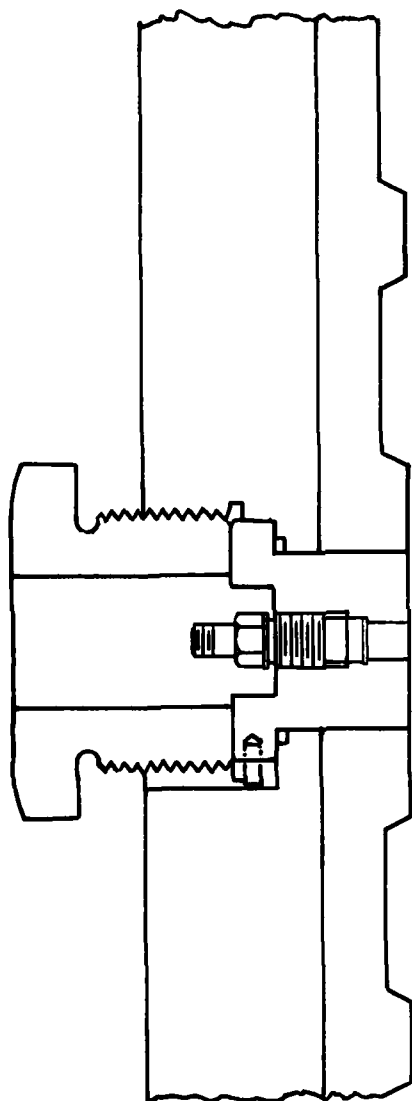


FIGURE 10. PRESSURE TRANSDUCER MOUNTING.

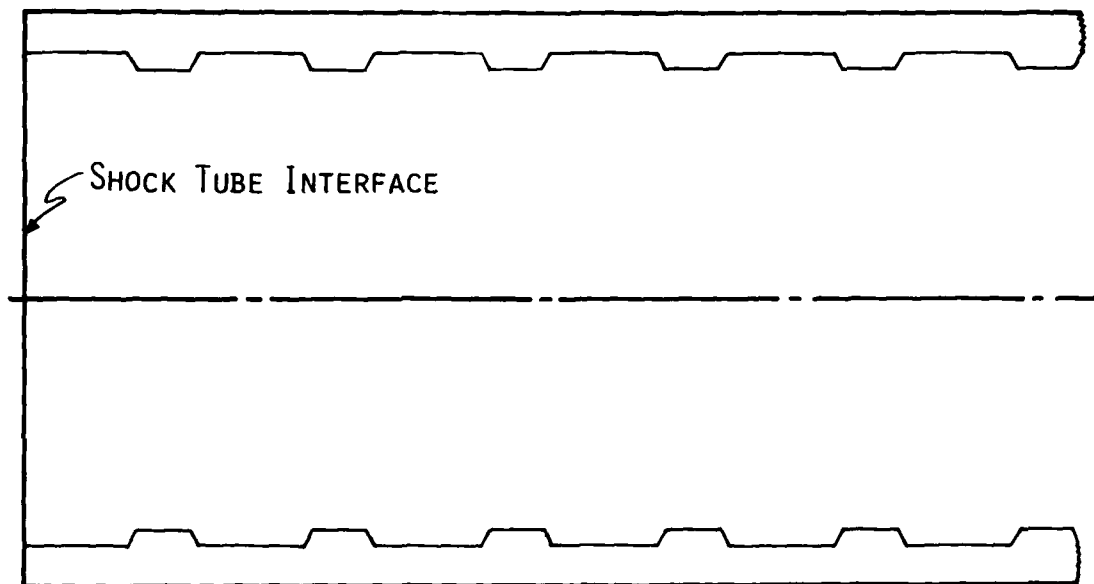


FIGURE 11A. INITIAL ENTRANCE REGION DESIGN.

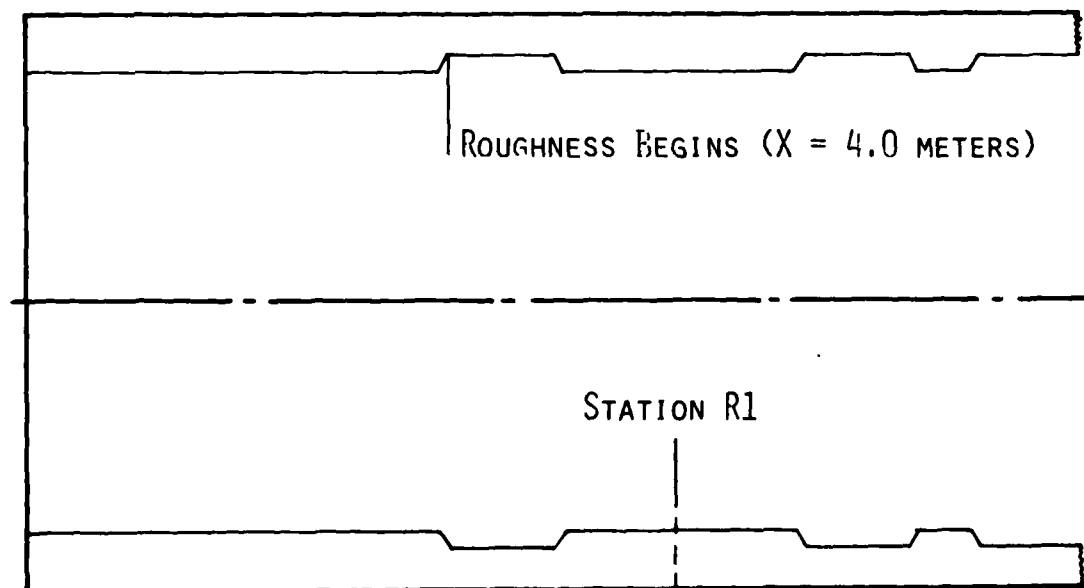


FIGURE 11B. FINAL ENTRANCE REGION DESIGN.

Shock time of arrival (TOA) measurements were made along the shock tube as a basis for code comparison and as a check on the pressure measurements. TOA measurements were accomplished with NASA twin probe ionization gauges coupled to a counter system via existing electronics. The probes operate on the principle that the heated gas behind the shock front provides a conductive path between the probes which produces a trigger signal. TOA locations are given in Appendix A.

Pressure history measurements were made at various stations along the smooth and ribbed test sections (Figure 12). Smooth wall stations were designated C through I; ribbed wall stations were designated R1 through R6 for transducers mounted flush with the rib tops and V2 through V3 for transducers mounted in the rib valleys. Transducer locations for the final runs are given in Appendix B. For the blast plug tests, the pressure transducers were mounted at three radial stations ($r = 0$, $R/2$ and $3R/4$ in a rigid end wall located downstream of a 24 diameter long ribbed section. PCB Piezotronics quartz pressure transducers models 113A22 and 113A24 provided high frequency (1 μ sec rise time) measurements. The transducers were protected from the thermal environment by covering the transducer face with a thin layer of RTV.

A custom built load cell (PCB Model 217M03) was employed to measure the longitudinal loads on a 0.15 meter (0.5 feet) long floating M-X rib liner section containing four ribs. Liner sections fore and aft of the floating liner were pinned in place, and a nylon ring was loaded in compression in front of the liner to take up any relative motion (Figure 13). The load cell had to be specially designed and fabricated since none could be found with an 0.1 meter (4 inch) I.D. to allow the shock to propagate through the test section. Fast response was required to measure the shock induced loads. Based on a measured stiffness of 3×10^{10} newton/meter and a liner mass of 4.9 kilograms, the load cell/liner response time was estimated to be of the order of 80 μ sec for a simple spring-mass system.

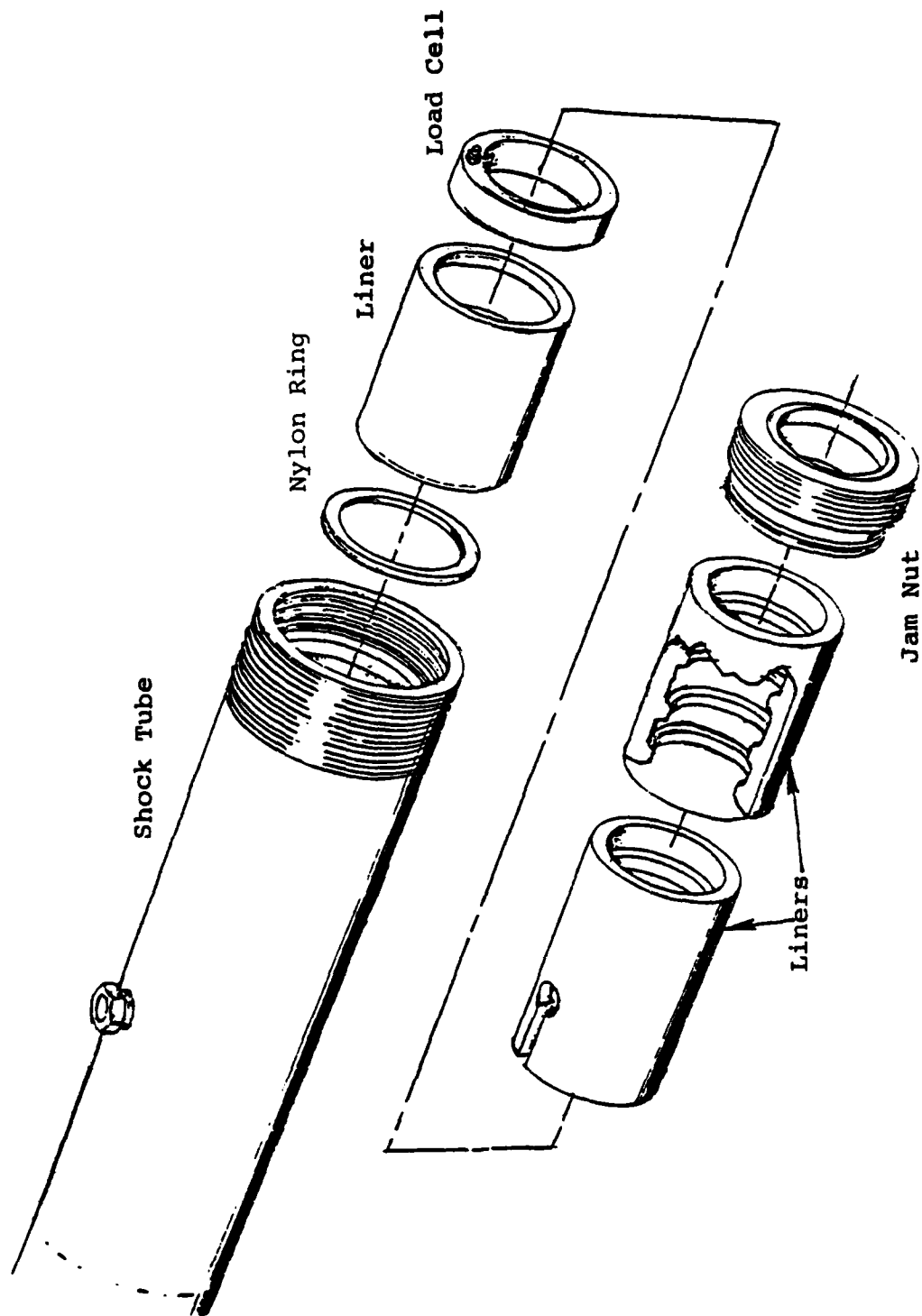


FIGURE 13. LOAD CELL ARRANGEMENT.

A square test section was constructed to accomodate optical measurements of two-dimensional rib/flowfield interactions (Figure 14). To avoid complicated geometrical transitions from the cylindrical NASA shock tube, a cookie cutter approach was used, and this limited the optical test section internal dimension to 5 cm (2 inches). Scaled MX ribs (scale factor 78) were located on the top and bottom of the test section extending 67 cm (26 inches) upstream and 30 cm (12 inches) downstream of the center of a 5 cm x 15 cm optical port utilizing plexiglass windows flush mounted with the sidewalls (Figure 15). The overall test section length was 151 cm (5.0 feet) extending 30 cm (12 inches) into the forward NASA shock tube and ending abruptly at the aft NASA shock tube. Pressure transducers were located at both ends of the test section (labeled TS1 and TS3) and in the optical port region (TS2).

An SAI custom built holographic interferometer was employed to record shadowgrams and interferograms of the flowfield. A Nd/YAG frequency doubled laser emitting 30 mJoules of 5320 Å light in 20 nsec pulses provided a source of coherent illumination. Agfa-Gavaet film (number 10E-56) which spatially resolves 1500 lines/mm was used to record the images. Figure 16 shows the optical arrangement in place at the NASA shock tube; details of the holography system are contained in Appendix C.

An ionization gauge at Station I detected the shock arrival, and the gauge output triggered a delay pulse generator which fired the laser after a selected time. The actual laser firing time was verified by a detector placed within the laser beam. Shock wave arrival along the test section was measured at three pressure transducer stations relative to shock wave TOA at Station I. Therefore, the time at which the laser fired could be determined relative to the shock wave arrival in the optical port for comparison with code calculations and to estimate the position of the shock relative to the optical port.

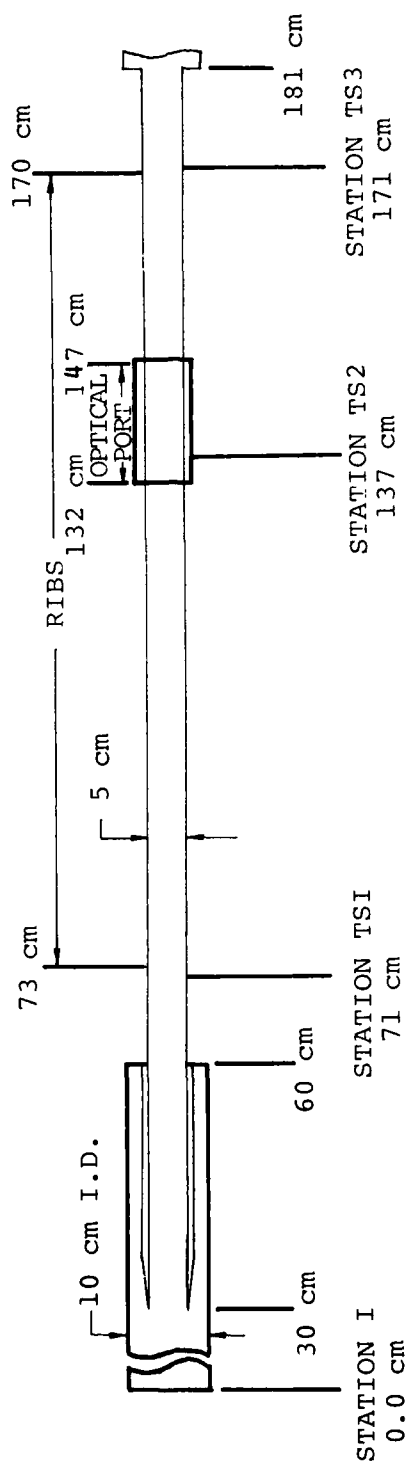


FIGURE 14. OPTICAL TEST SECTION.

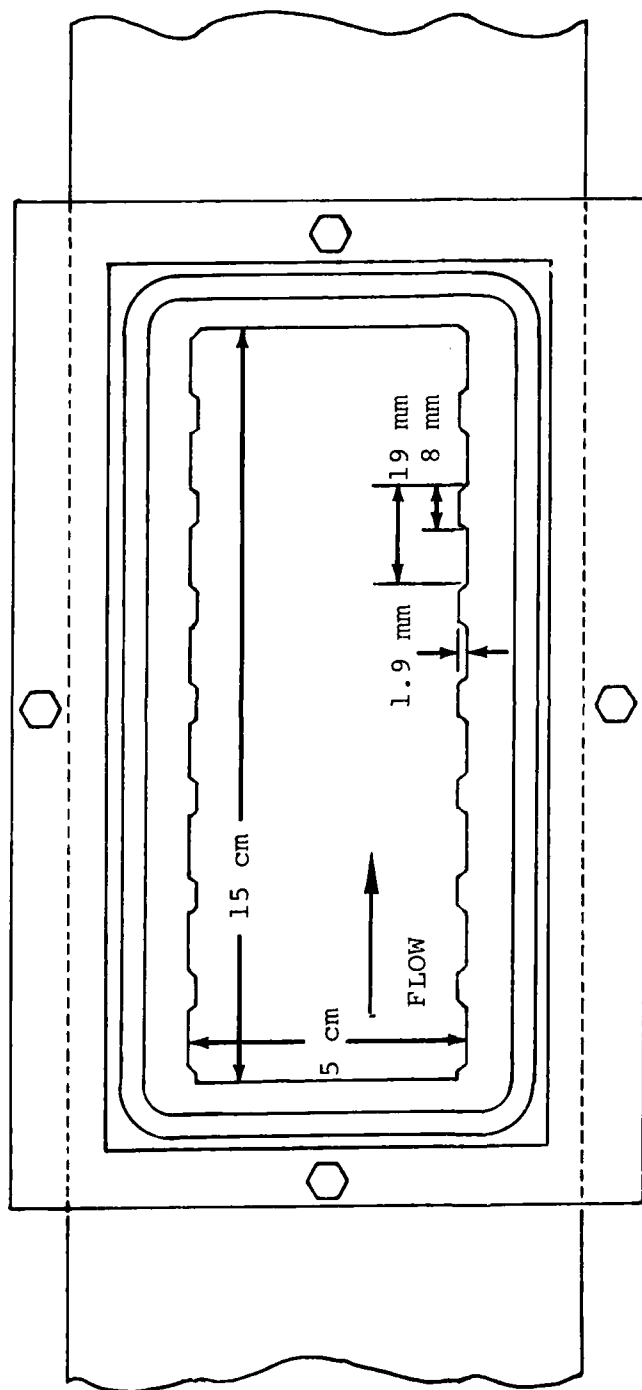


FIGURE 15. OPTICAL PORT IN TEST SECTION.



FIGURE 16. OPTICAL TEST ARRANGEMENT.

3.3 Data Recording and Processing

Shock wave TOA measurements were made in the smooth sections using the NASA MSTIMS (Multi-Station Time Interval Measuring System) which is a ten channel counter system with 0.1 microsecond time resolution (Reference 17). Counting begins after the arc discharge is extinguished (without this precaution the counters could be started prematurely by RF noise from the discharge). The counters are stopped by trigger signals from the NASA twin probe ionization gauges located along the shock tube. The outputs of the ionization gauges are monitored by Schmidt triggers which are enabled at an adjustable time after arc discharge (usually slightly longer than the time delay to begin counting). When the Schmidt trigger is fired, a 50 V pulse is generated which stops the counters. In the ribbed wall test sections TOAS were obtained from the pressure transducers.

Pressure histories at various stations were obtained from Polaroid records of the pressure transducer signals displayed on Tektronix Model 555 Oscilloscopes. Vendor supplied calibrations (Appendix B) were used to convert voltage to pressure levels. It was estimated that the shock wave pressure ratios could be determined from the photographs to within ± 10 percent; shock wave TOA was measured to ± 5 μ sec. Load cell data were recorded and processed in a similar manner. Details of interferogram data analysis are presented in Appendix C.

3.4 Test Matrix

Shock tube driver conditions were selected to produce shock strengths P_{21} of 80,300 and 700 at the entrance to the ribbed test section for the shock attenuation tests. Since the test flowfield is largely composed of Region 3 gas, the tests were designed to keep the acoustic impedance ratio Γ_{23} across the contact surface as close to one as practical to insure that wall effects would be communicated to the shock wave.

Table 1 gives the conditions for the shock attenuation tests. Shock tube repeatability as measured by run to run variation of shock C_s between stations at 2.0 and 3.2 meters from the diaphragm was generally better than 5 percent. Four series of tests are indicated. The first two series compared Reynolds number effects at a constant shock strength ($P_{21} = 80$). Series three and four addressed the effect of increased shock strength ($P_{21} = 300$ and 700) at nearly constant Reynolds number. Runs 5, 10, 7 and 50 were smooth tube calibration tests. Runs 56, 54 and 52 employed DD&M ribs while the remainder tested MX ribs. Runs 58 and 59 demonstrated test repeatability. End wall reflected pressures were measured on Run 63.

Test conditions for the optical runs were the same as for Series 2, except that the driver pressure was raised to 5.4 atmospheres. The shock wave pressure ratio in the optical port (Station TS2) was $P_{21} = 70$ (Appendix B), and the mean shock speed between stations TS1 and TS2 was 2.60 Km/sec ($M_s = 7.47$) with a variation of two percent for Runs 37 through 49. The optical system configuration for each run and firing time relative to the station TS2 TOA are listed in Table 2.

TABLE 1. SHOCK ATTENUATION TEST CONDITIONS.

Run	Driver Helium @ 300°K		Driven Air @ 300°K		P ₂₁	Acoustic Impedance Ratio Γ ₂₃	RE _{2D}	RE _{2D}
	P _{4i} (atm)	E ₄ (kJ)	P ₁ (atm)	C _s [*] (km/sec)				
5	27.3	937	1.0	2.9	80	0.8	3 x 10 ⁷	8 x 10 ⁶
56				3.0				
57				3.0				
58				2.9				
59				2.9				
10	2.7	195	0.1	3.1	80	0.8	3 x 10 ⁶	8 x 10 ⁵
63				3.0				
64				3.2				
7	27.0	1100	0.1	5.8	300	1.4	2 x 10 ⁶	1 x 10 ⁷
54				5.7				
60				5.5				
50	27.0	937	0.01	8.2	700	2.6	1 x 10 ⁵	4 x 10 ⁶
52				7.9				
61				8.2				

*Shock velocity between stations D and E

TABLE 2. OPTICAL TEST SERIES.

Run	Time* (μsec)	Optical Configuration
37	48.0	Laser Shadowgraphy
38	12.0	Laser Shadowgraphy
40	176.0	Laser Shadowgraphy
43	5.0	Laser Holography (Double Pulse-Offset Fringe)
44	73.0	Laser Holography (Double Pulse-Offset Fringe)
45	188.0	Laser Holography (Double Pulse-Offset Fringe)
46	341.0	Laser Holography (Double Pulse-Offset Fringe)
47	11.0	Laser Holography (Single Pulse)
48	81.0	Laser Holography (Single Pulse)
49	24.0	Laser Holography (Double Pulse-Zero Offset)

*Relative to shock wave TOA at Station TS2.

4.0 EXPERIMENT RESULTS

Sixty five runs were made in the NASA East facility to investigate the propagation of strong shock waves in tubes with internal ribs. Calibration runs established the shock wave characteristics in the existing smooth wall NASA shock tube and determined the arc driver performance. A few attenuation tests were conducted using one ribbed test section with an L/D of 24 to provide initial data in time for an MX interchange meeting. Final attenuation data and wall drag measurements were obtained in two test sections with a combined L/D of 48. Only these latter tests are reported here. End wall reflected pressures were obtained downstream of the first test section and optical data were obtained in the two dimensional test section.

Test results are presented in their reduced form in the following section. The raw TOA data and pressure traces are catalogued in Appendixes A and B along with appropriate transducer sensitivities and oscilloscope settings.

4.1 Pressure Waveforms

A conventional shock tube produces a shock wave which is followed by a region of constant pressure. The constant pressure region is terminated by the front of the rarefaction wave reflecting from the aft end of the driver. The rate at which the rarefaction front approaches the shock and at which the shock decays after the front reaches the shock are dependent on the sound speed of the driver gas and the length of the driver. Thus, pressure waveforms can be tailored to a certain extent by controlling these two variables.

For the present tests, it was desired that the shock wave traverse the entire length of the test section (4.8 meters) before rarefaction waves reached the entrance in order to investigate rib effects in the simplest possible flowfield. The longest available

7 driver (1.36 meters) was used to maximize the constant pressure regime. Pressure waveforms (e.g. Figure 17) in the smooth shock tube calibration runs exhibited a constant pressure duration which depended on shock strength and distance along the shock tube. In order of increasing shock strength the constant pressure durations were 100, 600, and 900 μ sec at the entrance to the ribbed test section ($L/D = 40$).

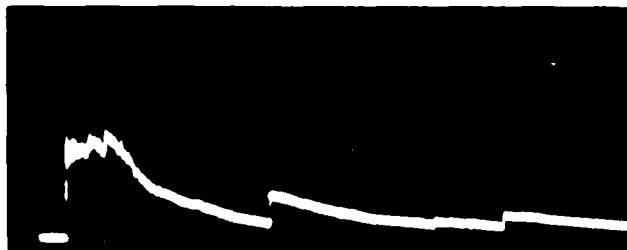


FIGURE 17. SAMPLE PRESSURE WAVEFORM (26.2 ATM/DIV AND 500 μ SEC/DIV).

The effect of MX ribs on the pressure waveform for $P_{21} = 80$ was to stretch out the constant pressure region and reduce the pressure ratio as the shock traveled through the ribbed test section (Figure 18). However, when the $P_{21} = 300$ shock encountered the ribbed test section the pressure waveforms exhibited a gradual rise behind the shock wave to two or three times the local shock value (Figure 18). Pressure waveforms for the strongest incident shocks tested ($P_{21} = 700$) showed a similar behavior. The increasing pressure may not be of particular significance to MX trench design, as trench expansion and venting effects (not simulated in these tests) will tend to reduce the pressure rise. However, calculations of the experiments can only be considered successful if these features of the pressure waveforms are predicted.

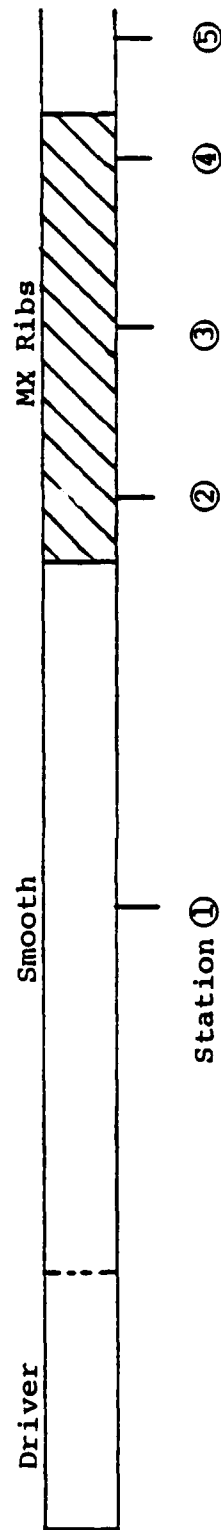
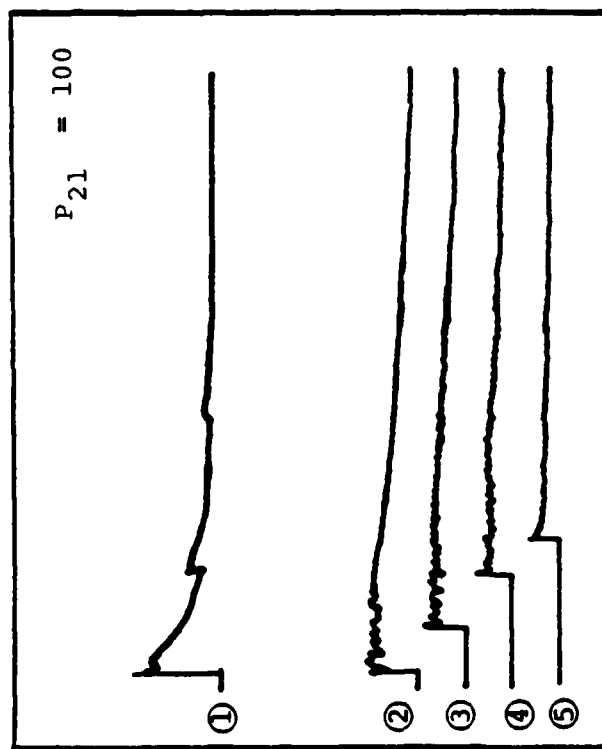
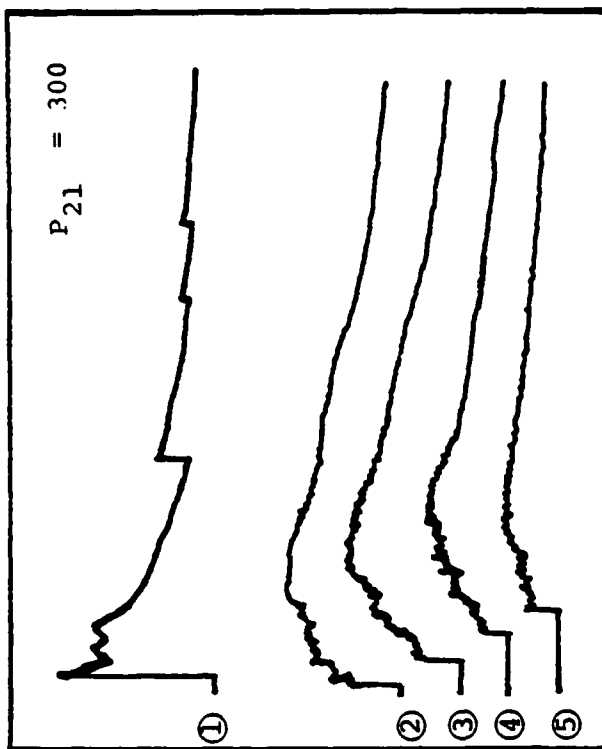


FIGURE 18. TYPICAL PRESSURE HISTORIES.

Pressure waveforms in the smooth tube forward of the ribbed test section showed several discontinuities well after the rarefaction waves had entered the test section indicating shocks were moving upstream into the smooth shock tube section. In the TRW (Reference 3) tests these perturbations were thought to be due to reflections off the ribs projecting into the flow; however, in the present tests the rib tops were aligned with the smooth tube. One-dimensional calculations indicated that the compression region forming in the ribbed tube builds into a relatively weak shock wave which propagates back upstream as the upstream pressure decays. Two dimensional calculations are required to resolve the detailed flow processes.

The waveforms presented here were all measured with transducers located in the rib tops. No significant differences were noted in the few valley measurements (e.g., Figures B-7 and B-8 of Appendix B).

4.2 Shock Attenuation

From the x-t plots prepared from the TOA data (Figure 19 to 21), it is apparent that the shock attenuates in the ribbed test sections. The $P_{21} = 80$ shock traveled 48 diameters (4.8 meters) in the smooth tube in 1.89 msec. In the MX ribbed test section the traversal time was 2.30 msec, and in the DD&M test section the traversal time was 2.67 msec. For the $P_{21} = 700$ shock the comparable times are 0.65 msec in the smooth section and 0.87 msec in the MX ribbed section. Thus, the rarefactions from the driver entered the test section before the shock wave left for the $P_{21} = 80$ runs. For the $P_{21} = 700$ runs the shock wave left the test section before the rarefactions arrived at the entrance.

Also apparent in the x-t diagrams are the trajectories of the shocks propagating upstream. Assuming that there is little or no flow down the shock tube (the incoming pressure waves

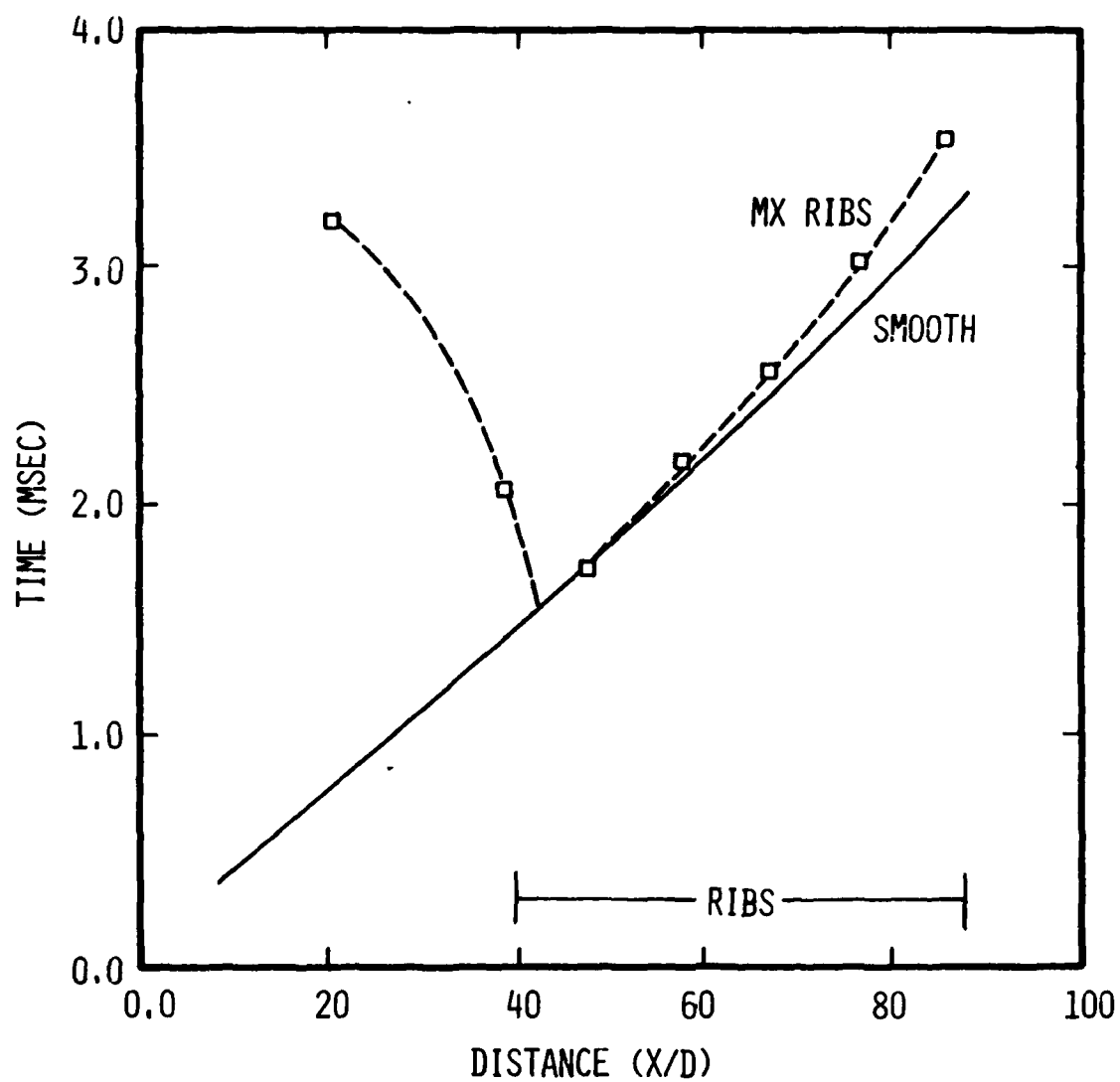


FIGURE 19. SHOCK TOA FOR MX RIBS ($P_{21} = 80$).

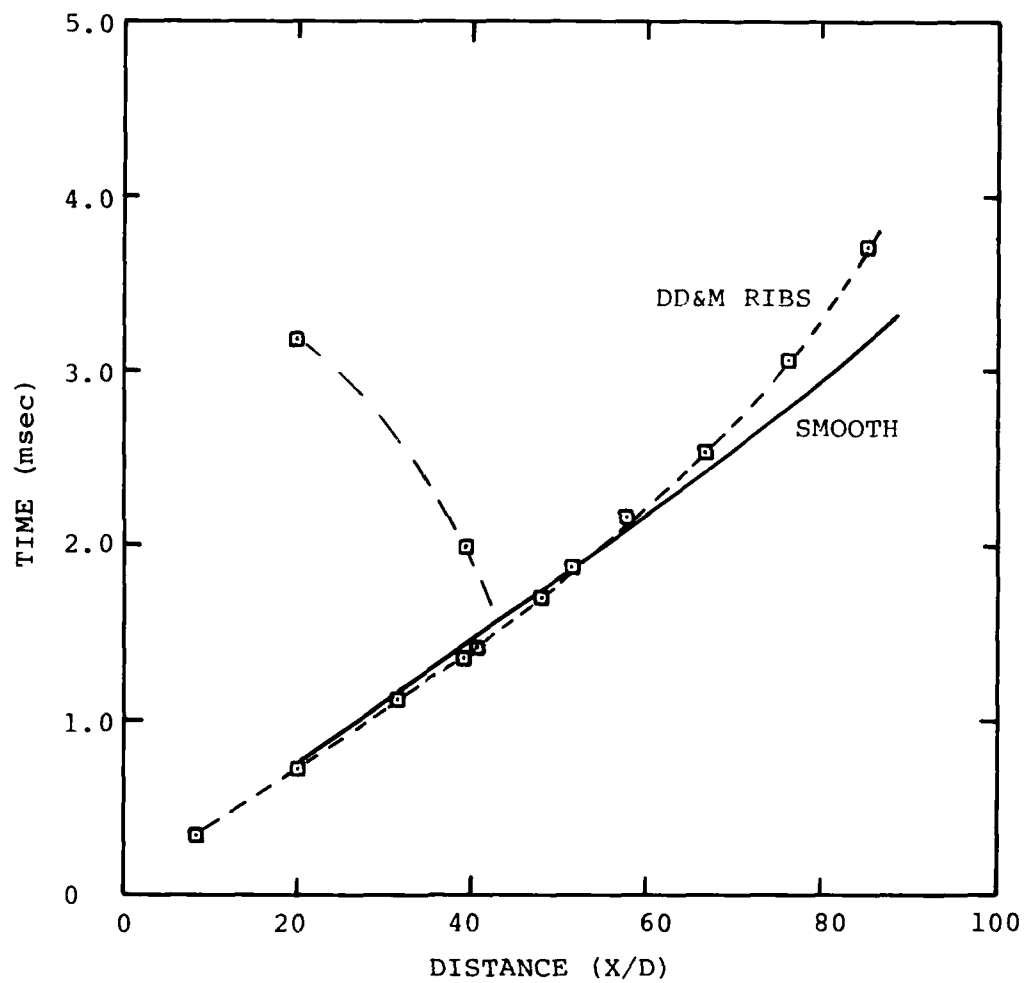


FIGURE 20. SHOCK TOA FOR DD&M RIBS ($P_{21} = 80$).

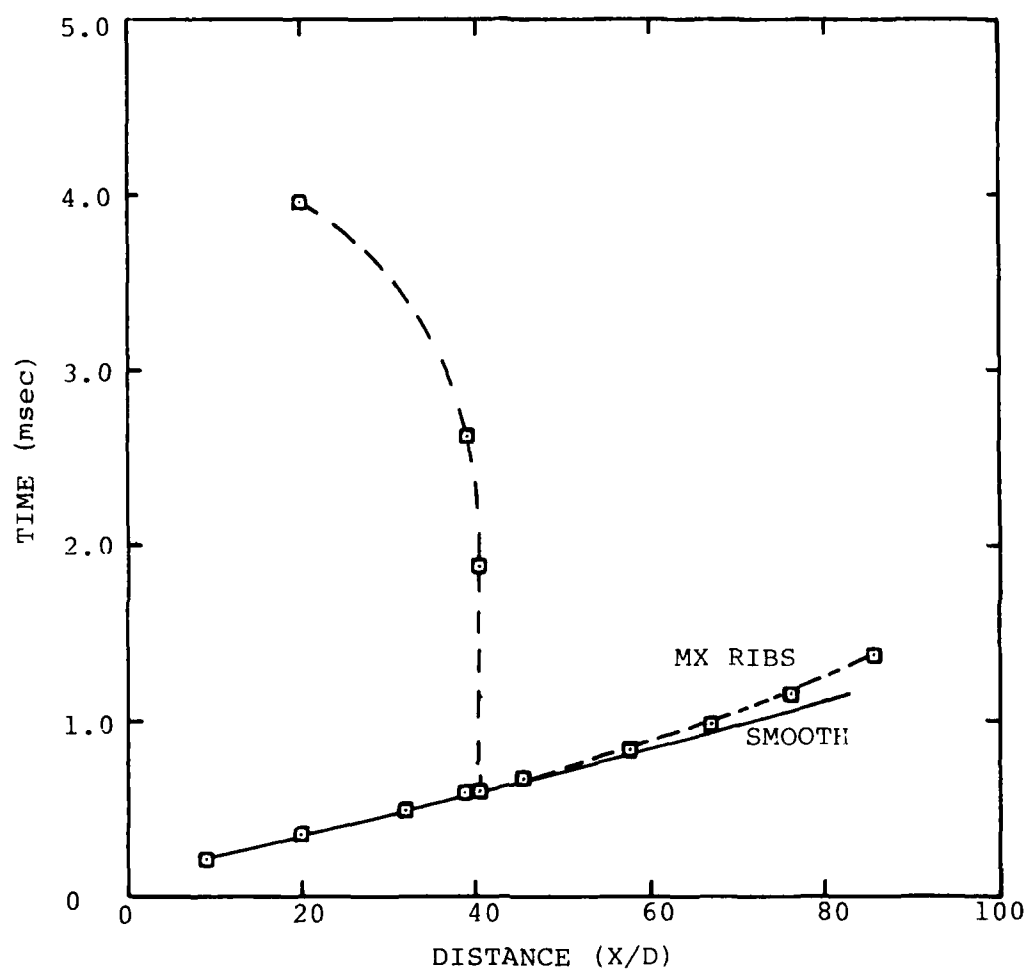


FIGURE 21. SHOCK TOA FOR MX RIBS ($P_{21} = 700$).

have decayed due to rarefactions from the driver), the shallow trajectories provide further evidence that the returning shocks are relatively weak.

Pressure measurements on the rib tops also demonstrate the shock attenuation. For $P_{21} = 80$ with an atmospheric test section, the shock attenuates to about 76 percent of its smooth wall value by 24 diameters of travel and to 45 percent of its smooth wall value by 48 diameters (Figure 22). Three runs (57, 58, 59) indicate the repeatability of the pressure measurements; the data generally agree within ± 10 percent (Figure 22). Shock pressure ratios from the TOA measurements via the Rankine-Hugoniot relationships were generally within 15 percent of those determined from pressure gauges located midway between the TOA probes. For example, the measured shock pressure ratio at the $X/D = 20$ station in Figure 22 was 95.3 while the value determined from TOA measurements was 83.5. Consequently, for the remainder of the test series only one successful (defined as acquiring the necessary data) test run was conducted for each objective, and only the reduced pressure data are discussed.

4.2.1 Reynolds Number Effect on Shock Attenuation

Shock attenuation data taken from the pressure measurements for $P_{21} = 80$ showed no discernable effects of flow Reynolds number. Tests run with initial pressures of 1.0 and 0.1 atmospheres produced nearly identical decay rates although the flow Reynolds numbers differed by an order of magnitude (Figure 23). The absolute values of the shock strengths were slightly different for the two tests due to sensitivity of the arc discharge to initial driver pressure; however, a consistent trend is seen in the smooth and ribbed wall data. In fact, if the data is shifted to match in the smooth tube, the results overlap.

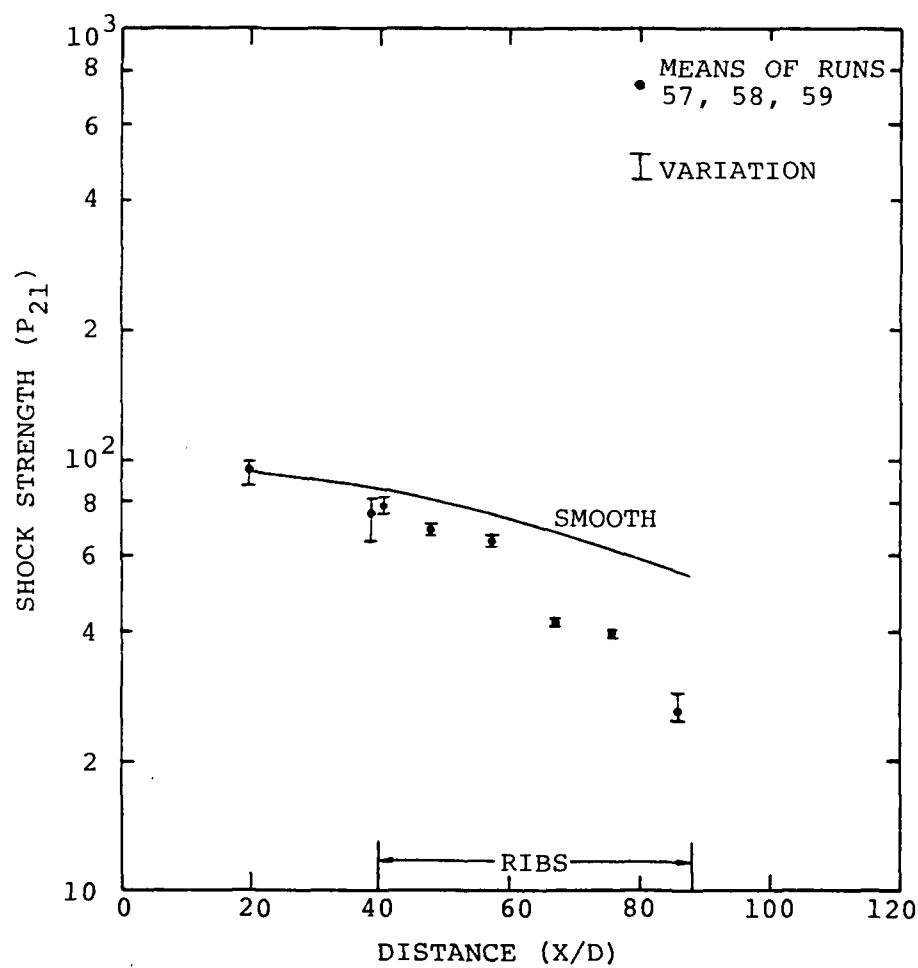


FIGURE 22. SHOCK ATTENUATION BY MX RIBS.

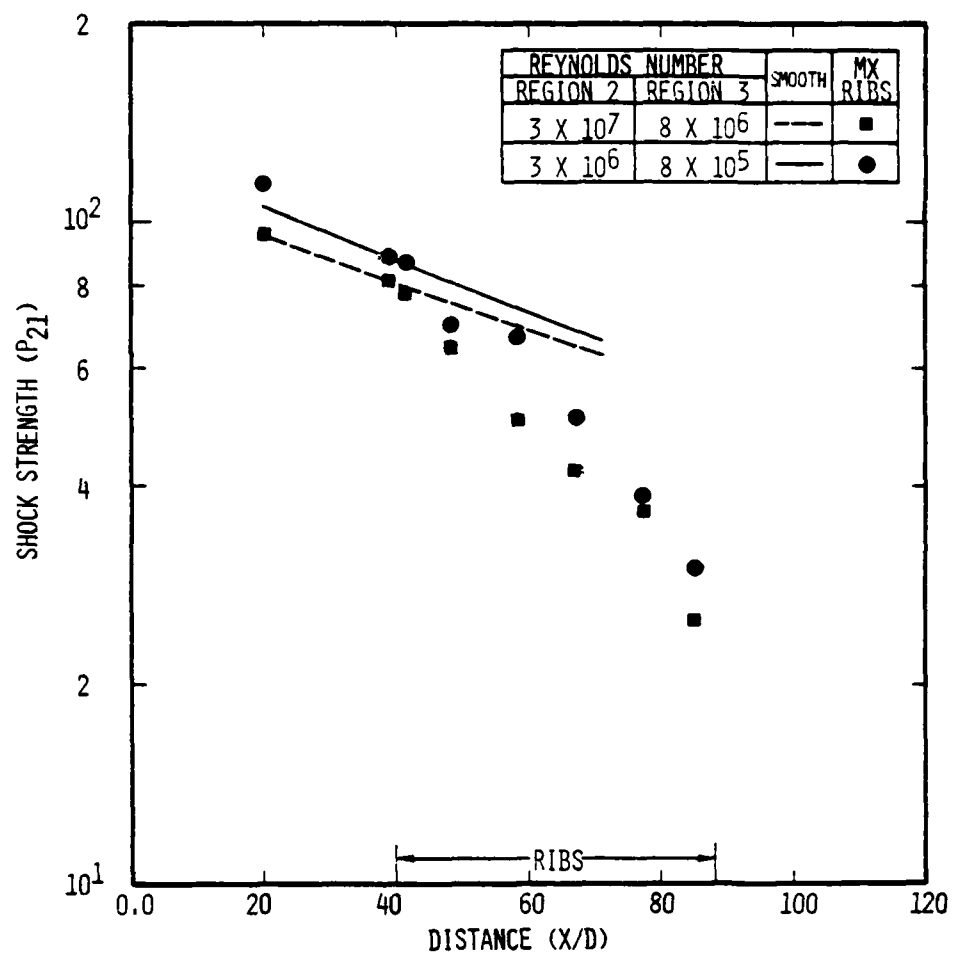


FIGURE 23. REYNOLDS NUMBER EFFECT ON SHOCK ATTENUATION.

The implication here is that scale effects introduced through the Reynolds numbers are not important to the attenuation process. This could come about in two ways: the pipe flow type skin friction is truly in the Reynolds number independent region or the attenuation mechanism is a purely inviscid shock-rib interaction phenomena.

4.2.2 Shock Strength and Rib Geometry Effects on Shock Attenuation

Shock attenuation data taken from the pressure measurements are summarized in Figures 24 through 26 for three initial shock strengths and two rib geometries. The present data indicated essentially, a relatively uniform, exponential decay rate with the shock waves reaching half their associated smooth wall strength in about 30 diameters for $P_{21} = 80$ and in about 20 diameters for $P_{21} = 300$ and 700.

It must be noted that measurements made in the preliminary portion of this program indicated a dramatic drop in shock strength at a station three diameters from the rib test section entrance (Figure 27). The present tests conducted with the first transducer located behind the first rib and the second transducer nine diameters from the start of the ribs are not conclusive as to how quickly the shock decays initially. Caution should be used in assuming simple exponential data fits until the entrance effect is resolved.

The DD&M rib geometry appeared to provide slightly better shock attenuation than the MX ribs. The increased attenuation was not evident until the shock had traveled through 20 to 30 diameters of the ribbed section after which the effect seemed to be increasing. The additional attenuation at the end of the test section ($L/D = 48$) was 25, 27 and 19 percent over the MX attenuation in order of increasing shock strength.

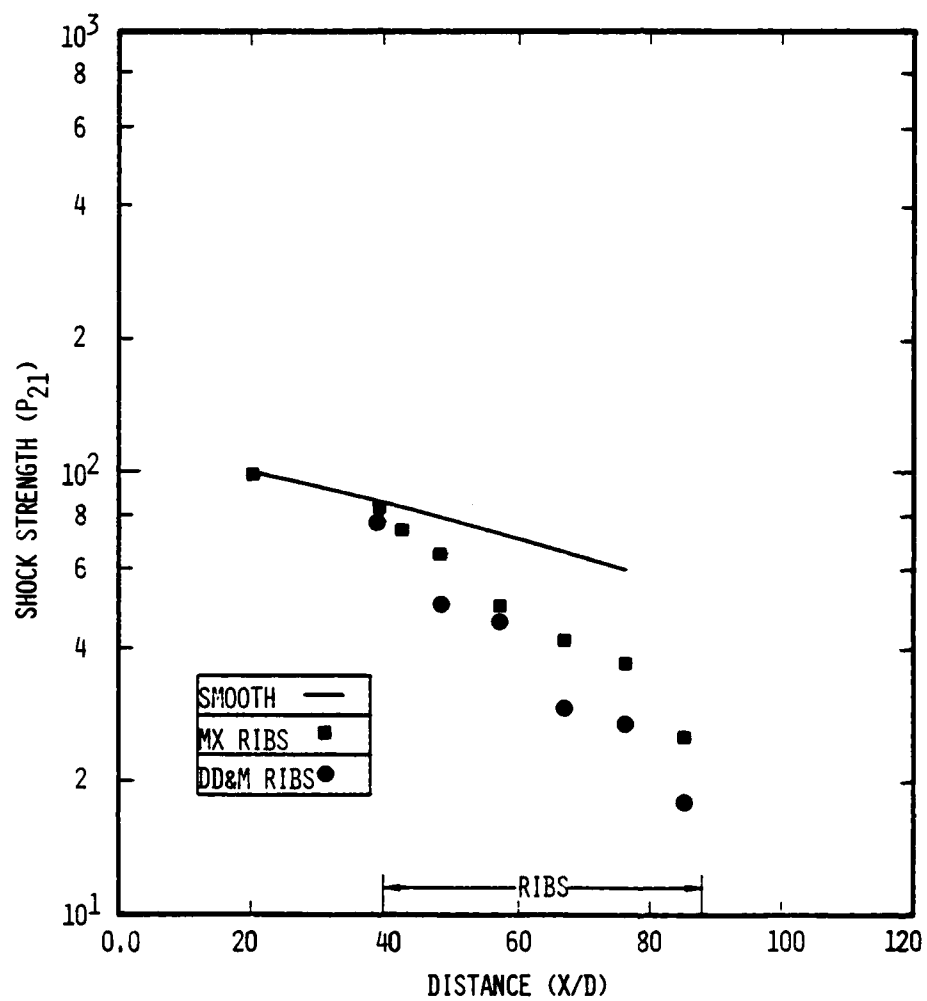


FIGURE 24. SHOCK ATTENUATION AT $P_{21_i} = 80$.

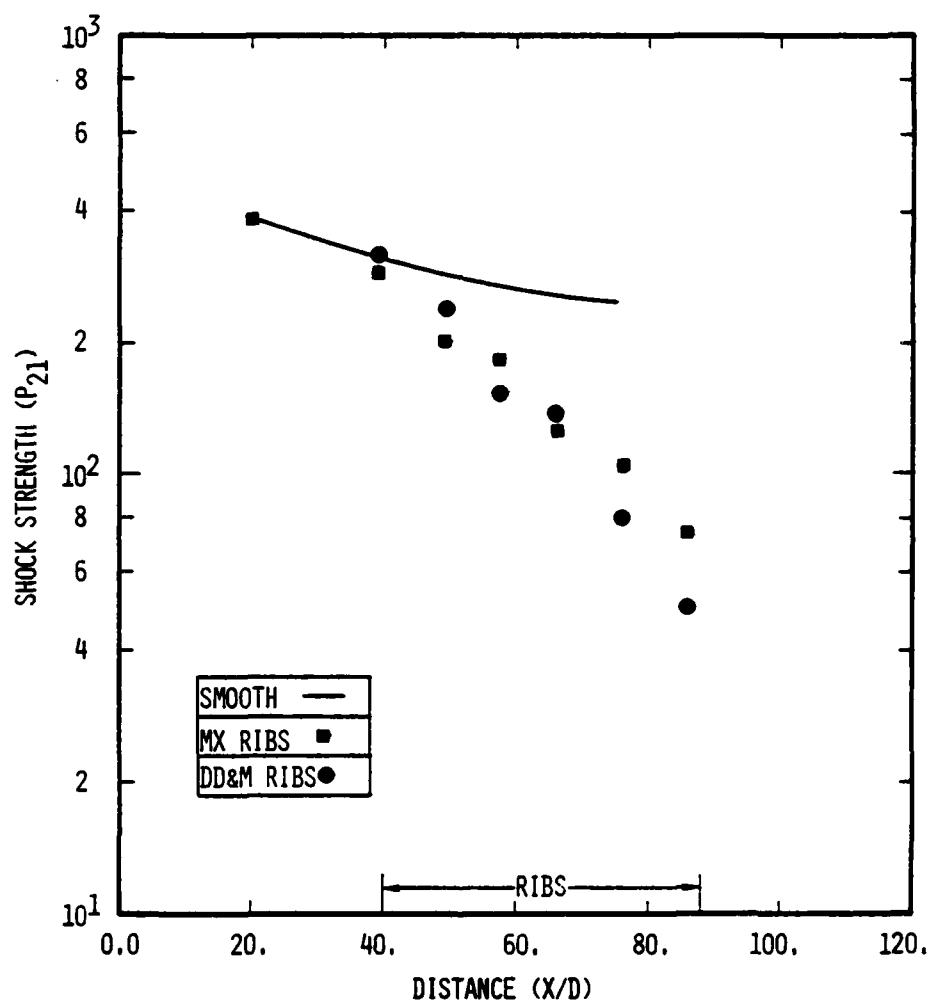


FIGURE 25. SHOCK ATTENUATION AT $P_{21_i} = 300$.

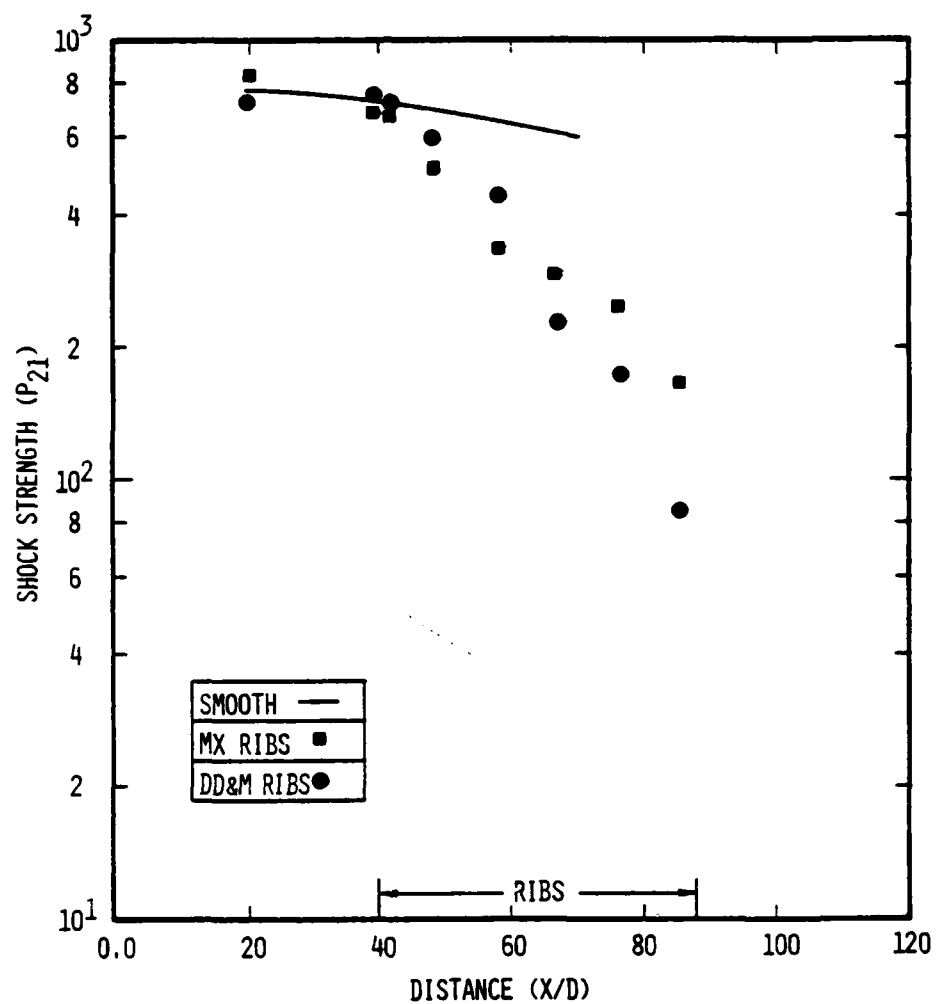


FIGURE 26. SHOCK ATTENUATION AT $P_{21_i} = 700$.

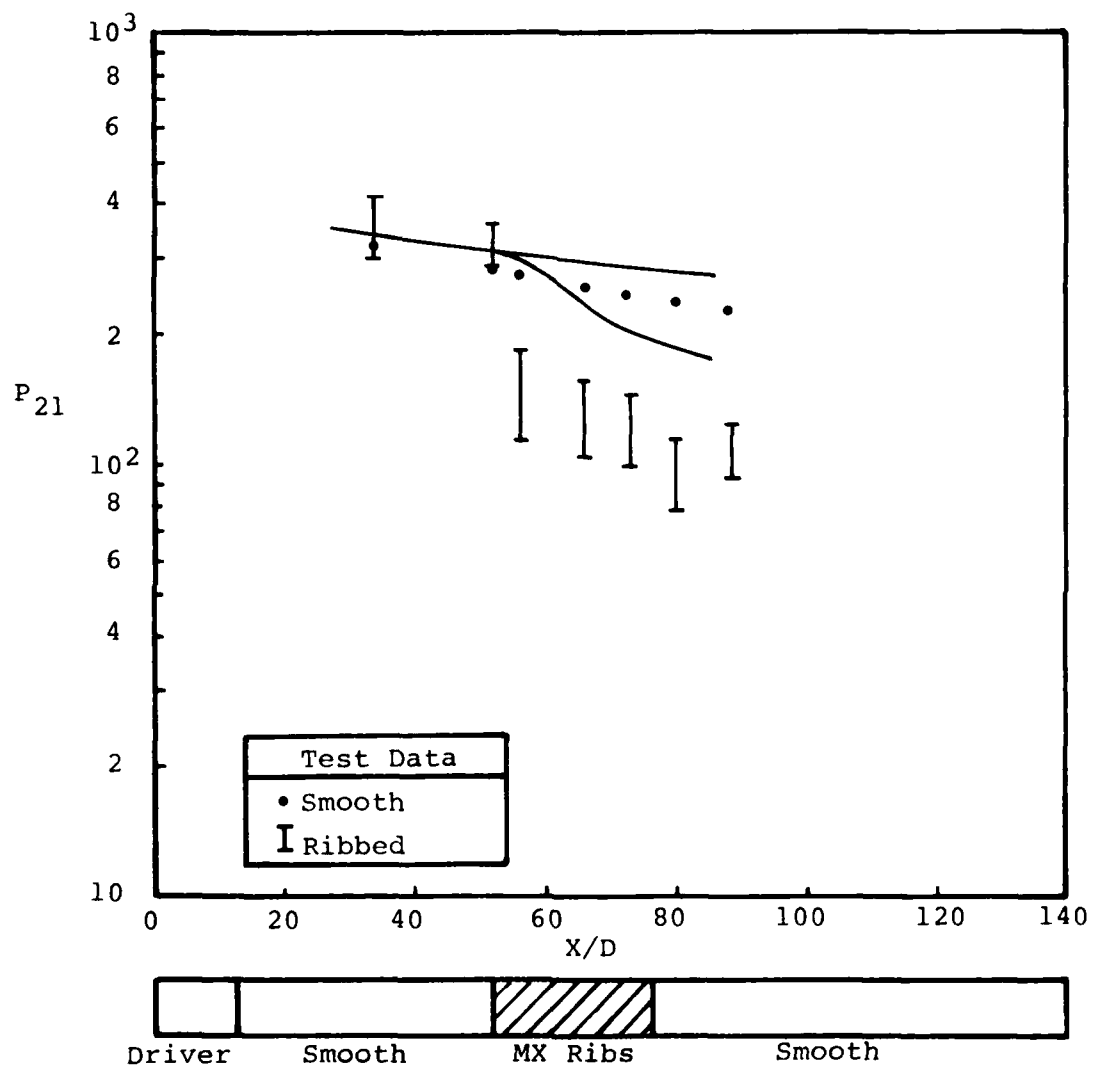


FIGURE 27. SHOCK ATTENUATION FROM PRELIMINARY TESTS.

4.3 Optical Flowfield Measurements

Holographic techniques provided a qualitative description of the rib/flowfield interaction as well as limited quantitative measurements of the density fields. Photographs of the holographic images are catalogued in Appendix C; shadowgrams and interferograms of the region near the main shock and at 7.5 diameters behind the main shock are described here. Additional quantitative data could be reduced from the holographic interferogram plates.

Laser shadowgrams of the main shock region (Figure 28) confirm the existence of a multiple shock structure predicted by AFWL two-dimensional calculations (Reference 2). The source of the multiple shock structure is the reflection of the main shock from the ribs. Each shock-rib interaction sends out a blast wave-like shock which interacts with the main shock and with the other secondary shocks. This propagation controls the strength of the main shock and therefore drives the attenuation process. It is useful to discuss schematically the shock rib interaction for one rib, and then to note the additional features of multiple ribs from the flow visualization.

As the main shock passes each trapezoidal rib compression and expansion disturbances are created at both the forward and rearward faces. Mach reflection occurs on the forward face (Reference 23) causing a reflected shock to propagate along the backside of the main shock. Shock strength is discontinuous across this three shock intersection, and the trajectory of this point is called a triple point path (Reference 19). Mach reflection continues until the Mach stem reaches the corner where an expansion fan is formed. The expansion fan overtakes and weakens the Mach stem causing the curvature required to keep the shock normal to the top of the rib. As the expansion fan overtakes the triple shock



FIGURE 28. LASER SHADOWGRAM OF SHOCK/RIB INTERACTIONS.

the reflected wave is weakened reducing the shock strength discontinuity at the triple shock. This weakening also decelerates the radial velocity of the triple shock which in the limit of weak reflected shocks is the sonic velocity behind the shock.

Another expansion fan is created when the shock reaches the downstream edge of the rib. Again, the expansion fan overtakes and weakens the portion of the main shock near the wall keeping the shock normal to the rear face of the rib. Mach reflection occurs when the shock on the rear fan reaches the bottom of the rib creating a second triple shock intersection. This event is the last portion of one cycle of the motion of the main shock.

The rib/shock interactions combine in a complicated but symmetric pattern. The main features observed in the shadowgram are identified in Figure 29, and they include:

- Reflected secondary shocks on the main shock forming triple shock intersections.
- Slip streams in the wake of the triple shock intersections.
- Vortex like separated regions on the top and backside of the ribs.
- Reflected shock interactions with turbulent cavity flows.

To quantify the two dimensional aspects of the flow, holographic interferometry was used to measure density variations across the shock tube (Appendix C). A holographic interferogram of the main shock (Figure 30) displays a complicated image of the flow. The density profile at section A-A one rib spacing behind the shock (Figure 31) reveals a strong compression process with the density at the wall exceeding twice the centerline density. This increased density is presumably a result of the reflection of the main shock from the ribs.

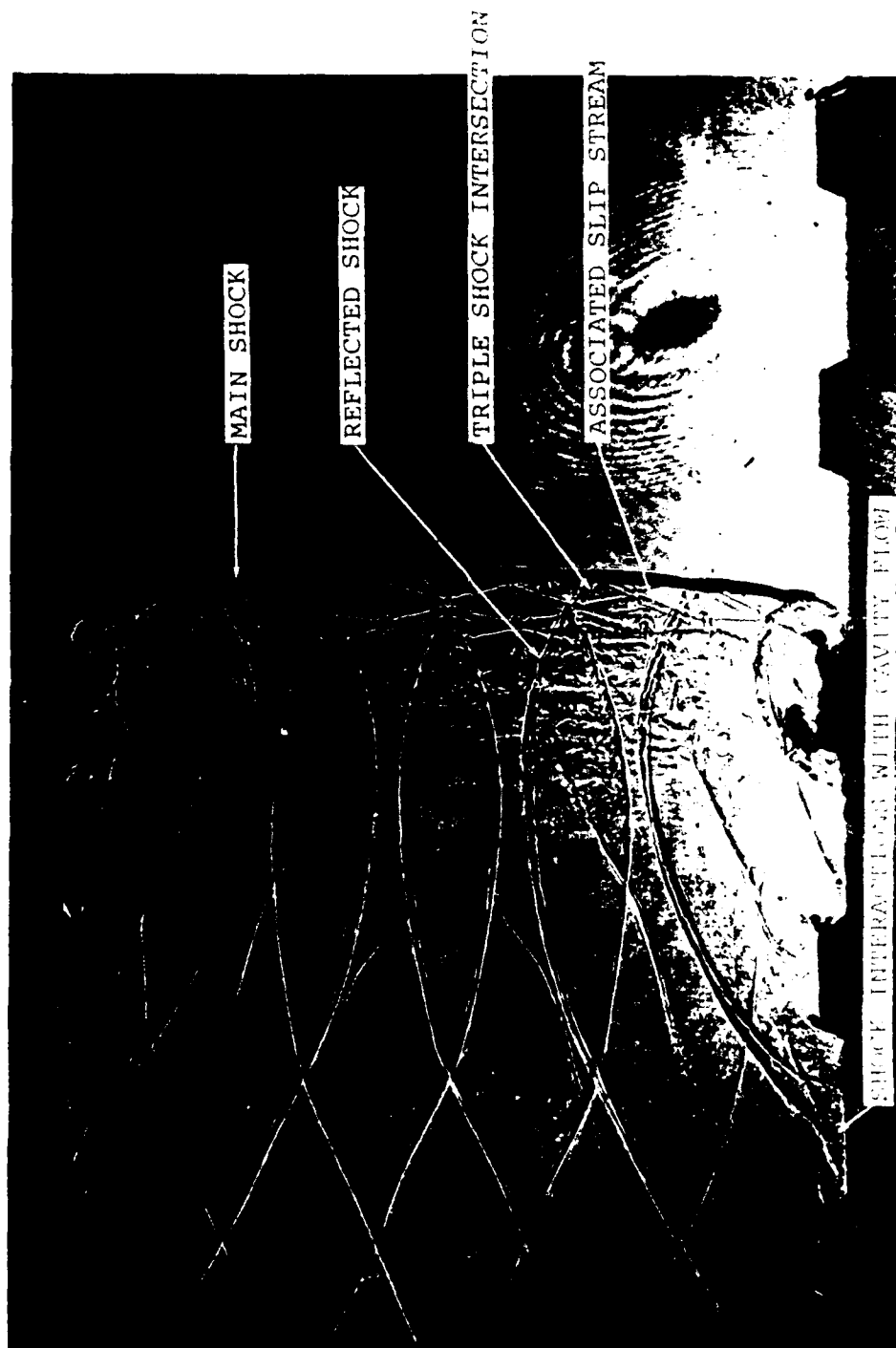


FIGURE 29. THE MAIN FEATURES OF THE SHOCK.

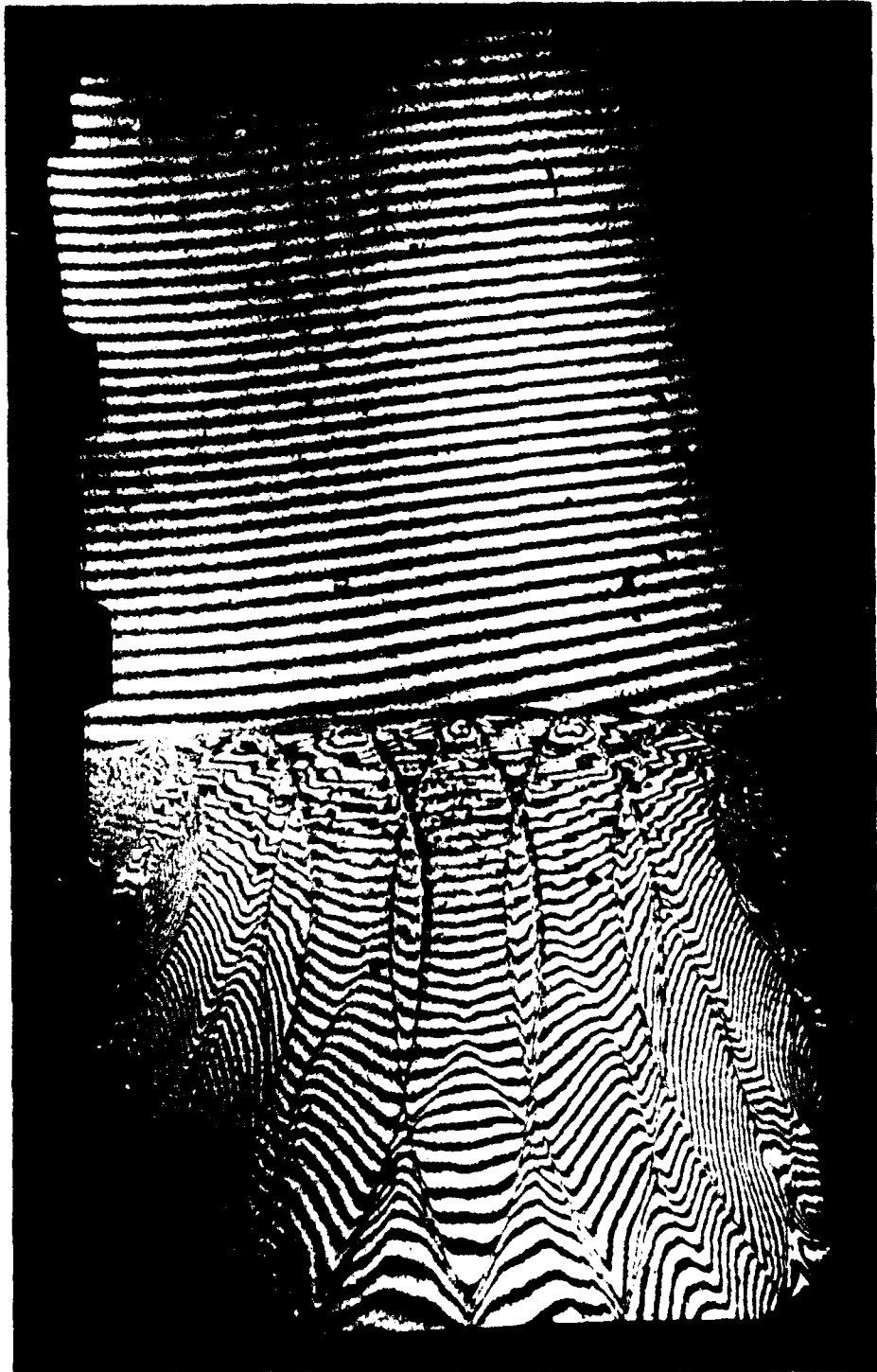


FIGURE 30. HOLOGRAPHIC INTERFEROGRAM OF SHOCK/RIB INTERACTIONS.

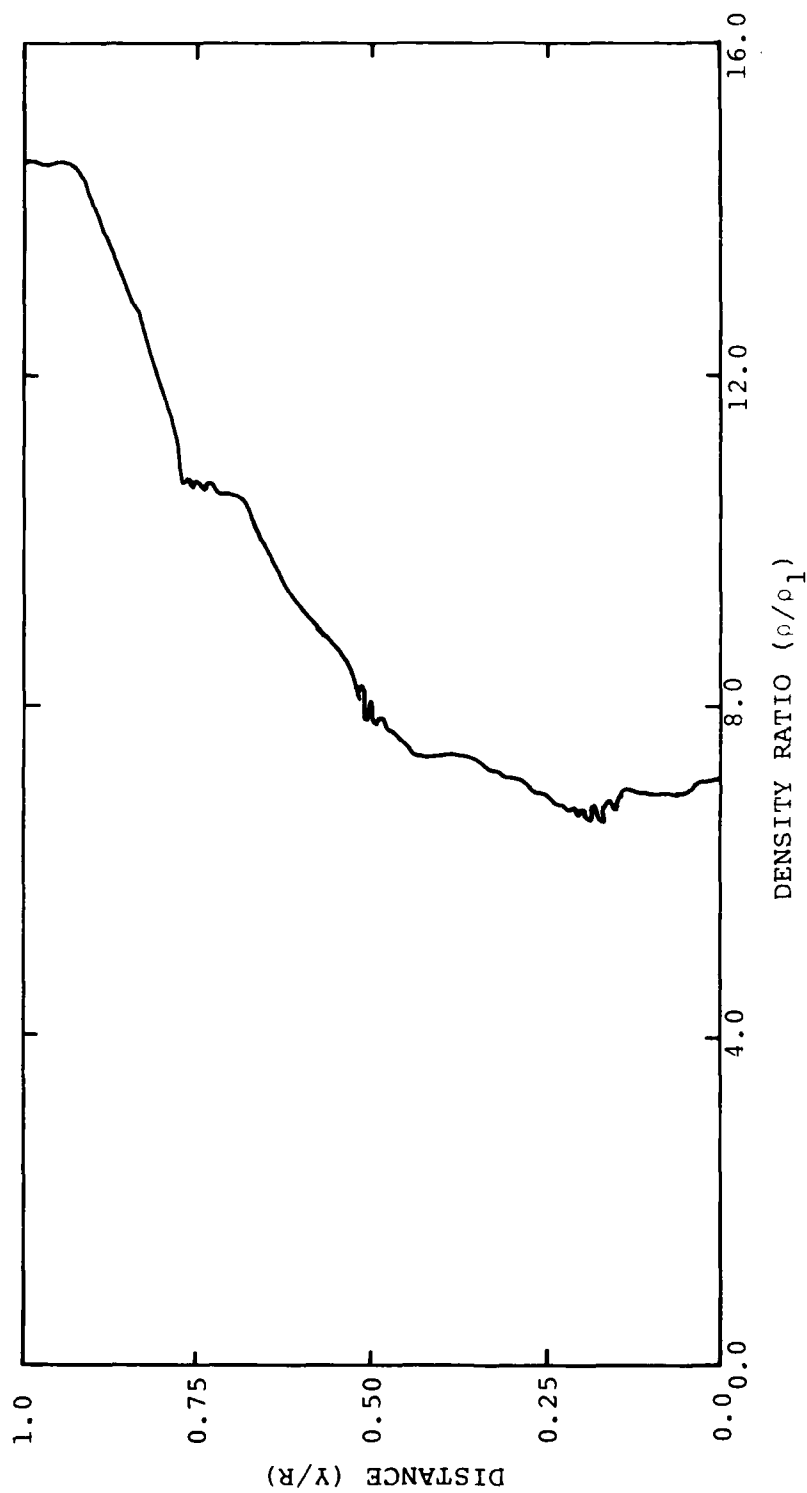


FIGURE 31. DENSITY PROFILE ONE RIB SPACING BEHIND SHOCK ($\rho_1 = 9.03 \times 10^{-4} \text{ gm/cm}^3$).

Farther behind the shock ($X/D = 2.5$) the flowfield appears to become stationary with bow shocks extending diagonally across the shock tube (Figure 32). The angle between the straight portion of the bow waves and the shock tube axis is approximately the Mach angle ($\alpha = 30^\circ$) where the flow Mach number is calculated from the shock speed via the Rankine-Hugoniot equations. This would imply relatively weak waves.

A holographic interferogram (Figure 33) of the flow at a later time than the laser shadowgram ($X/D = 7.5$) displays the sensitivity of the technique to detect small density changes. The dominant features of the flow are displayed in the regular distortion of the vertical fringes coincident with the diagonal shocks in the laser shadowgram. Density profiles across the tube at station 7.5 diameters behind the shock confirm that the shocks are weak (Figure 34).

Viscous effects appear to be confined to a region near the wall in contradiction to the main assumption in one-dimensional computer models. The shadowgrams reveal a turbulent region only between the ribs. The interferogram at $X/D = 7.5$ does not indicate a large cold wall influence ($T_\infty/T_w = 11.8$ for $M_s = 7.5$) on the flow above the ribs. Even if the small density increase near the wall in Figure 34 is interpreted as a viscous effect, the boundary layer height is on the order of the smooth wall boundary layer thickness (2.9 rib heights) predicted by the method of Reference 25.

The inference from the flow visualization results is that the shock flowfield is two-dimensional in the vicinity of the main shock, and that two-dimensional calculations are required to understand the shock attenuation process. The influence of viscosity may contribute increased attenuation over that predicted by inviscid codes.

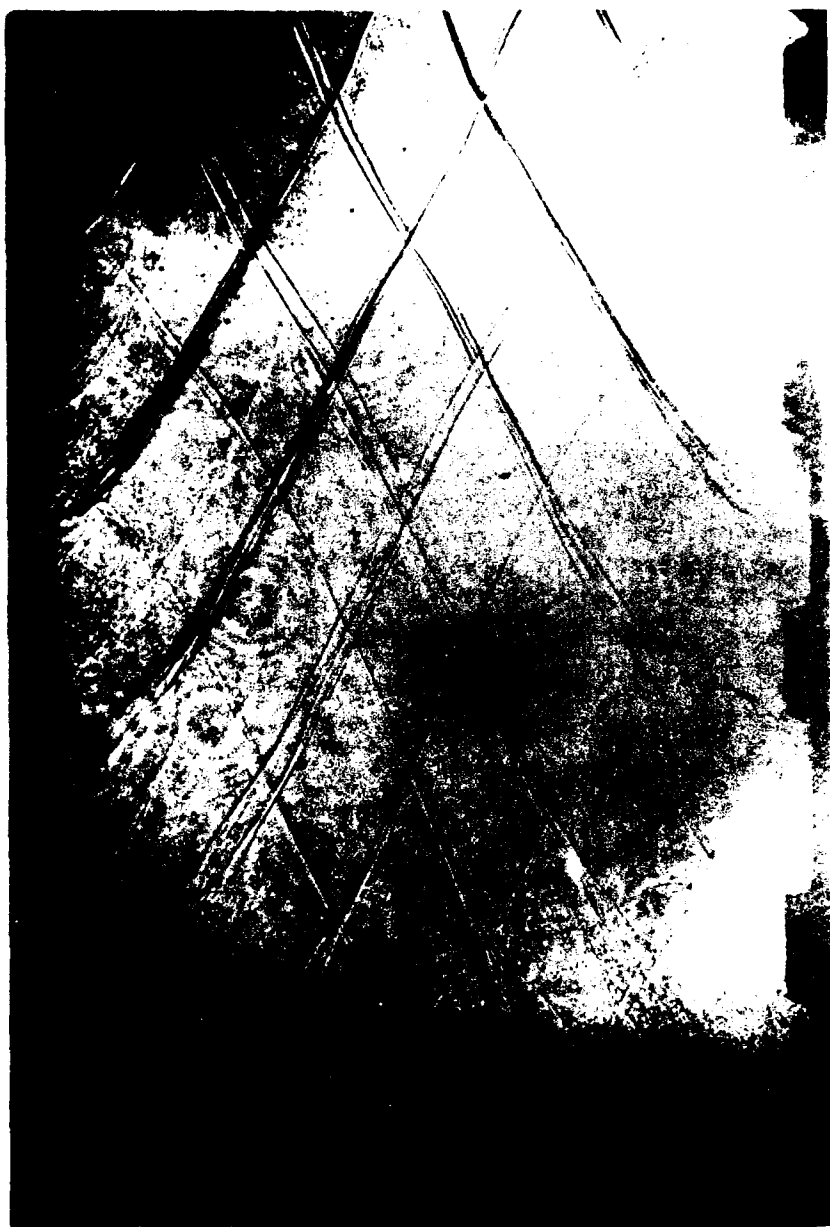
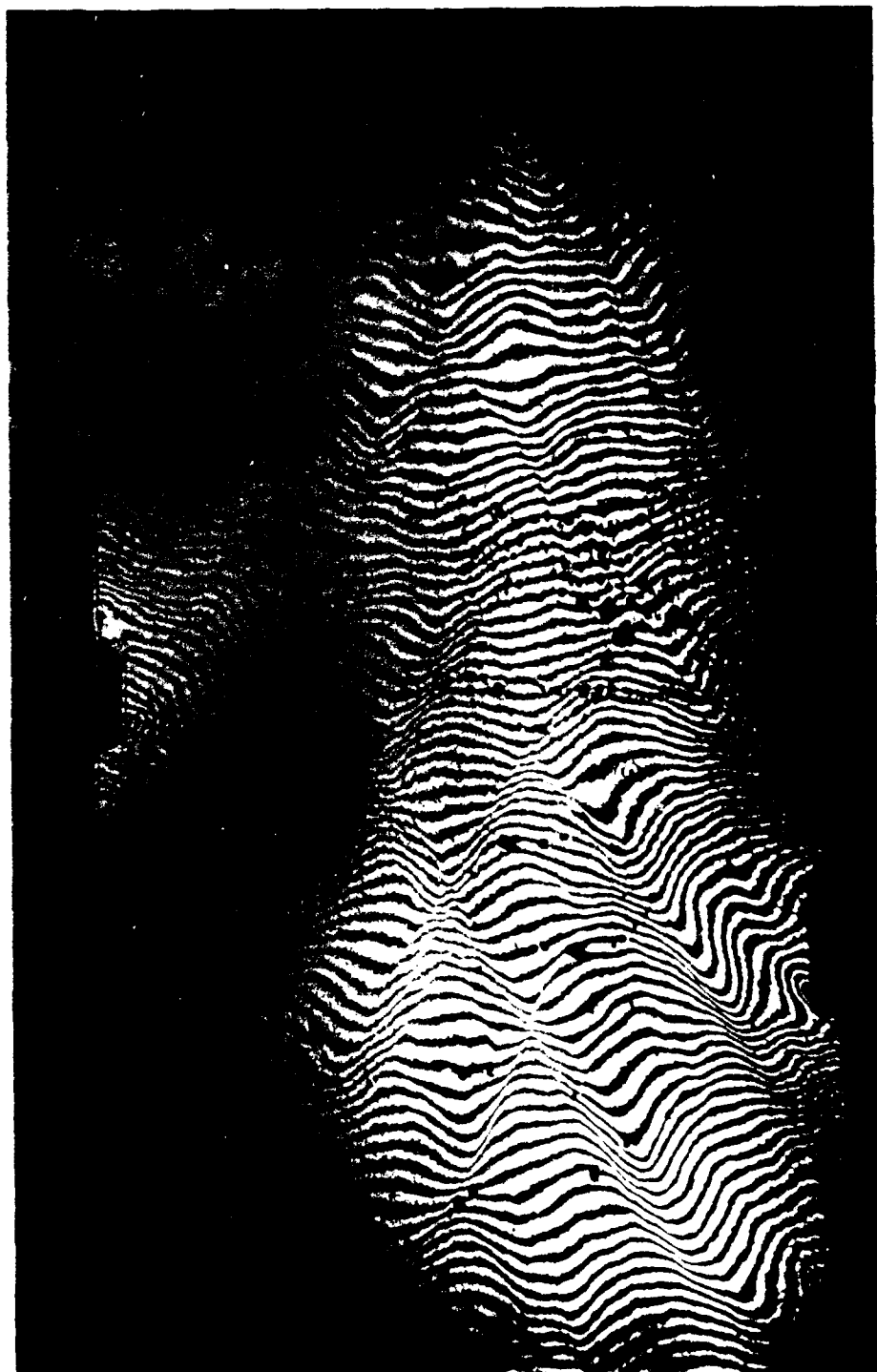


FIGURE 32. LASER SHADOWGRAM OF QUASI-STEADY FLOW.



↑ ↑ ↑
 0.001 in
 0.001 in
 0.001 in

FIGURE 33. HOLOGRAPHIC INTERFEROGRAM OF QUASI-STEADY FLOW.

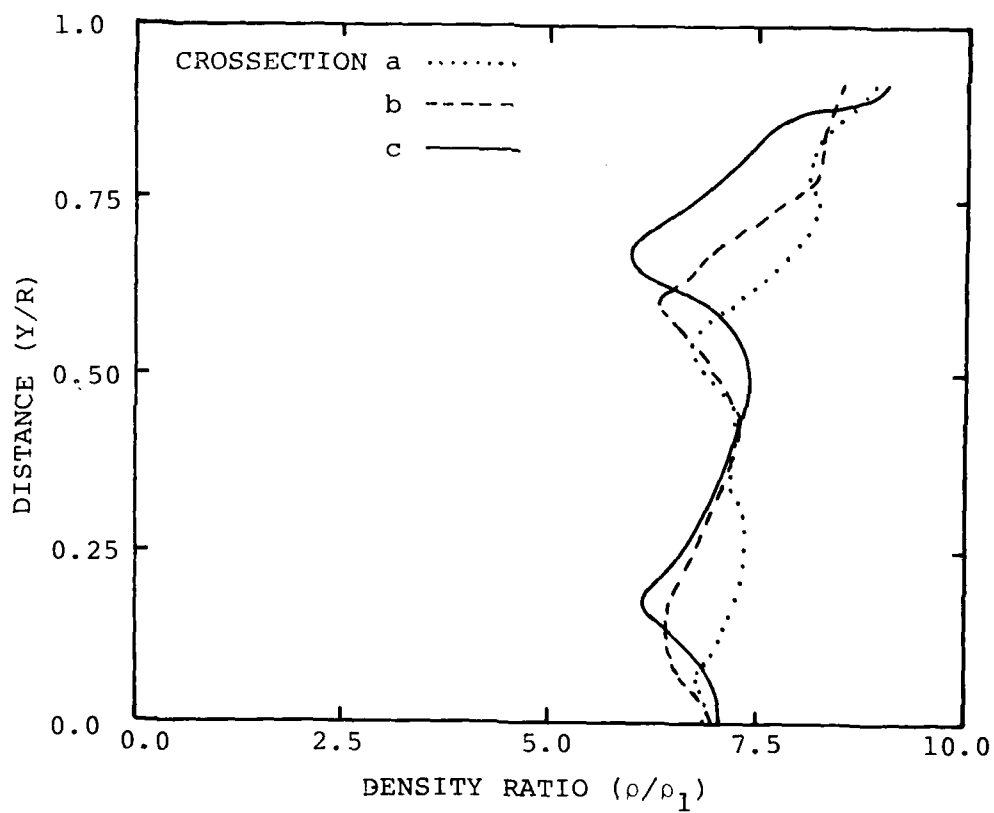


FIGURE 34. DENSITY PROFILES IN THE QUASI-STEADY FLOW ($\rho_1 = 9.03 \times 10^{-4}$ GM/CM³).

4.4 Wall Drag

Wall drag measurements were performed for runs 60 and 61 with the custom built load cell located twenty diameters downstream of the entrance to the MX rib test section. The local shock strengths were $P_{21} = 190$ and 350 respectively. Load cell signals (Figure 35) are characterized by a sharp initial deflection followed by a gradual rise to peak load at 2 msec after shock arrival. The similarity of the load cell and pressure signals led to the suspicion that the load cell was sensitive to internal pressure, and this was confirmed by post test calibrations. Vendor estimates of the internal pressure sensitivity indicated that at the shock arrival the internal pressure may account for as much as thirty percent of the signal; at later times the internal pressure could account for even larger fractions of the signal. Therefore, only the initial signal deflection was analyzed.

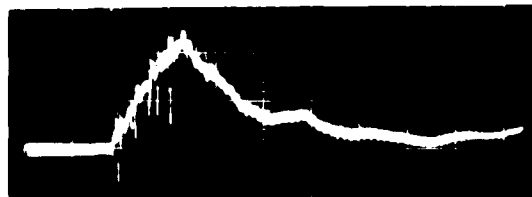
Measured drag forces were divided by the liner wall area and a dynamic pressure calculated from

$$q = \frac{\gamma}{2} P_2 M_2^2 \quad (18)$$

to produce an effective drag coefficient near the shock wave (Table 3). The steady flow drag coefficient according to equations 1 and 2 is 0.032 which is a factor of three to five lower than the measured values. In light of the flow visualization observations, a simple wave drag model was formulated which at least produces higher estimates. Loads on the MX rib liner section were calculated from pressure distribution estimates for forward and rearward facing steps neglecting the tangential shearing forces on the axial portion of the liner. The average pressure on a forward facing step (Reference 21) was taken as

$$\bar{P}_f = 0.8 (M_2 + 2) P_2 \quad (19)$$

RUN 60



RUN 61

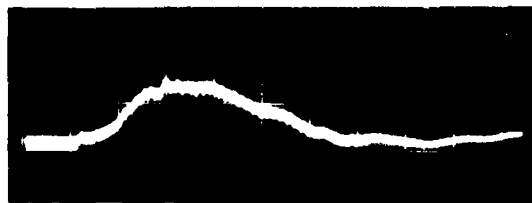


FIGURE 35. MX LINER LOAD HISTORIES
(10 KLBS/DIV X 1.0 MSEC/DIV).

TABLE 3. LOAD CELL MEASUREMENTS.

Run Number	Local Shock Strength	Drag Coefficient		
		Experiment	Pipe Flow Estimates	Wave Drag Estimates
60	190	0.08	0.032	0.08
61	350	0.17	0.032	0.05

and the average pressure on a rearward facing step (Reference 22) was taken as

$$\bar{P}_R = \left(\frac{5.4 - M_2}{10} \right) P_2 \quad (20)$$

Both correlations are for data for stream Mach numbers between two and four. The net axial force on the rib is the product of the pressure difference and the rib frontal area. The rib force is averaged over the wall area per rib which is normalized by the dynamic pressure to form a drag coefficient

$$C_D = \frac{k}{S} \frac{2}{\gamma} \left(\frac{1.09 + 0.9 M_2}{M_2^2} \right) \quad (21)$$

where k/S is the rib height to spacing ratio.

The few experiments conducted here are not conclusive. More detailed experiments and comparisons with the models are required to establish an effective wall drag.

4.5 End Wall Reflected Pressures

The end wall test (Run 63) was run at an initial test section pressure of 0.1 atmosphere and an initial shock strength at the rib section entrance of $P_{21} = 80$ to minimize the loads on the shock tube. A measurement station was not available just upstream of the end wall, so the shock strength incident on the wall was inferred from Run 64. Initial test conditions for Run 63 were the same as for Run 64, and pressure measurements at four stations upstream of the end wall matched well for the two runs (Figure 36). The interpolated value of the incident shock strength is $P_{21} = 52$, and the theoretical reflection factor for a plane shock wave of this strength is about 7.5 (References 15 and 17).

End wall reflected shock waveforms exhibited an irregular pattern as seen in the plots of Figure 37 (oscilloscope traces in

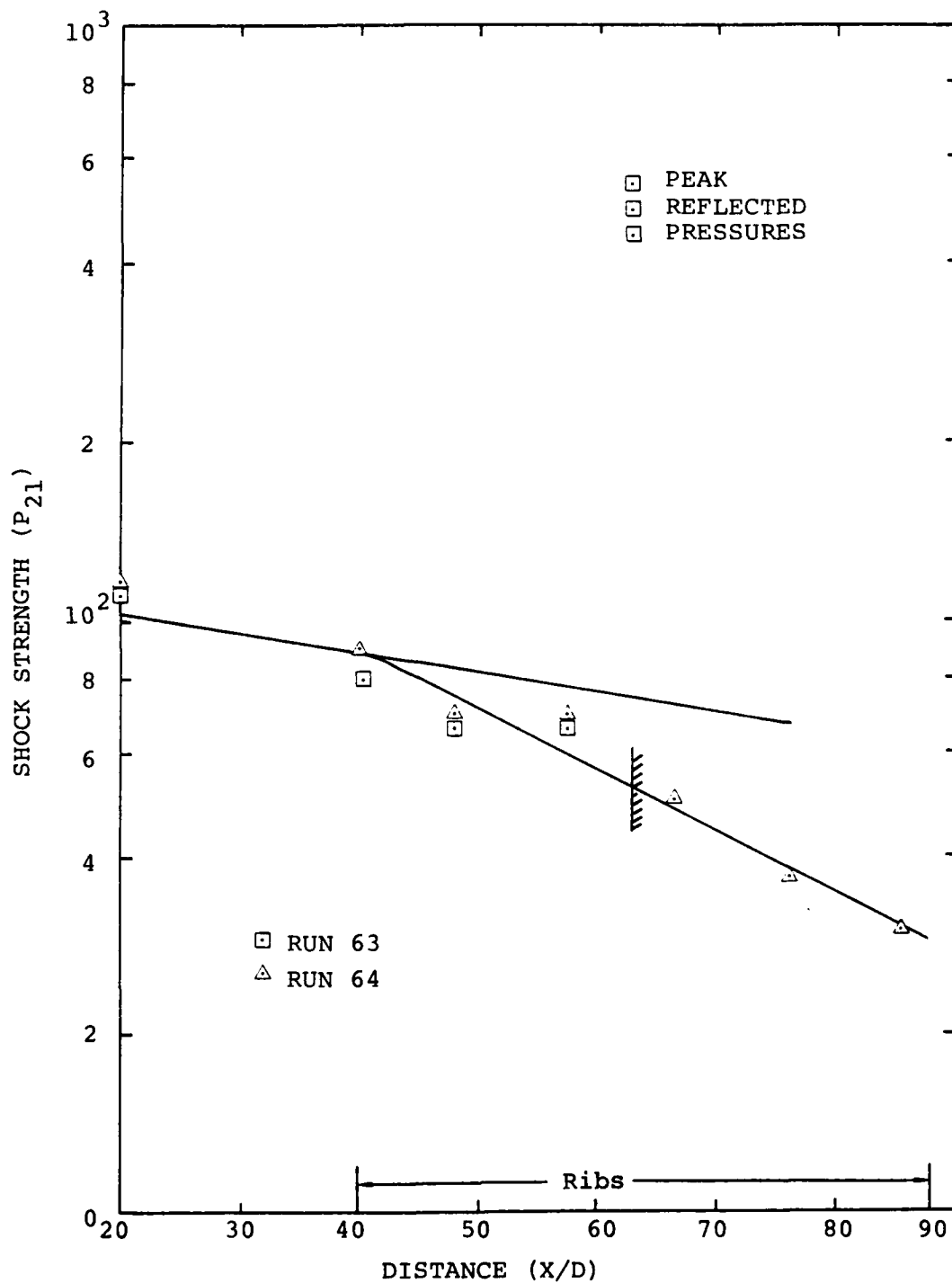


FIGURE 36. END WALL PRESSURE MEASUREMENTS.

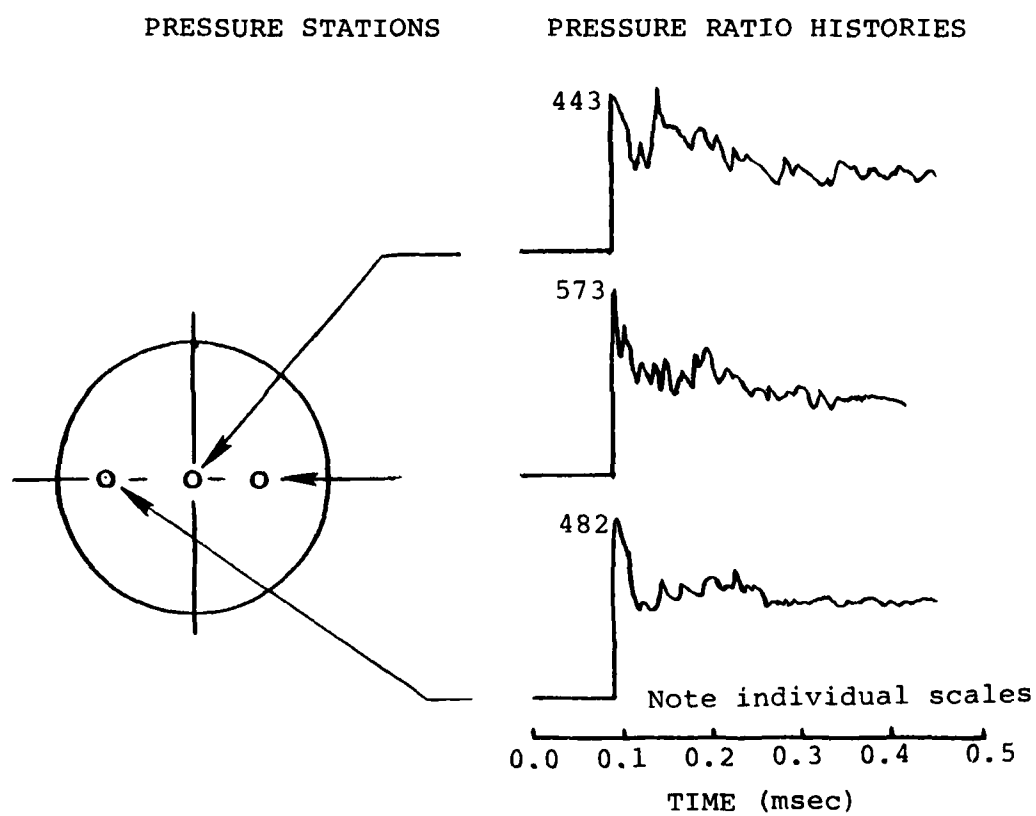


FIGURE 37. END WALL PRESSURE MEASUREMENTS.

Appendix B). The three pressure transducers measured an initial reflected pressure ratio from 8.5 to 11. The duration of this unexpectedly high reflected pressure varied from 20 μ sec at the outer transducer ($r = 3R/4$) to 50 μ sec at the centerline after which the pressures decayed to near the expected level.

Pressure fluctuations apparently not associated with transducer ringing (the transducers have a natural frequency of 500 kHz) persist throughout the records. Interaction of the reflected shock and the nonuniform region behind the incident shock may contribute to the pressure fluctuations for about 200 μ sec after shock arrival. A more satisfactory explanation for the irregularities and seemingly high reflection factors is apparent from the optical measurements which revealed the strongly two-dimensional nature of the flow-field. Secondary shock waves created by the ribs cause the shock to be nonplanar (small differences in shock arrival time were noted on the end wall) and create pressure variations in both the radial and longitudinal direction. Thus, pressures measured on the rib tops may not be representative of local pressures across the tube.

4.6 Shock Attenuation Comparison with Predictions

Three approaches have been suggested for predicting shock attenuation in a ribbed tube: empirical such as the method due to Porzel, one-dimensional with fully developed pipe flow assumptions and two-dimensional inviscid calculations. A brief comparison of the first two techniques with the test data is presented here. Two-dimensional calculations are being performed by Air Force Weapons Laboratory personnel.

The semi-empirical prediction method of Porzel has the simple form

$$\frac{P_{21}}{P_{21_i}} = e^{-2\frac{k}{D}\left(\frac{X}{D}\right)} \quad (22)$$

for strong shocks. Using the geometrical rib height ($k/D = 0.038$) Equation (22) does not predict the attenuation observed in the present tests (e.g., Figure 38). Although an expression of the form

$$e^{-A \frac{K}{D} \left(\frac{X}{D} \right)}$$

would reproduce the test results, there is no guarantee that the coefficient is constant for other shock strengths or other rib designs. Furthermore, an empirical approach such as this ignores the detailed physics of the attenuation mechanism and does not treat the entrance region effects observed in the preliminary tests.

RIST code calculations were performed for the tests run at initial shock strengths of $P_{21i} = 80$ and 300 to determine if one-dimensional shock attenuation models based on steady flow assumptions were adequate. The calculations predicted the smooth wall shock attenuation reasonably well (Figure 39), considering that no special pains were taken to model driver conditions. RIST also did an acceptable job of predicting shock attenuation for the lower shock strength ($P_{21i} = 80$). However, RIST code calculations of the attenuation for $P_{21i} = 300$ were inadequate. The rapid decay in shock strength at the entrance region measured in the initial tests was not reproduced, and overall shock strengths decayed about twice as fast as predicted.

No attempt at improving the one-dimensional code was undertaken in light of the entrance effects and the distinctly two-dimensional flowfield observed in the optical results. Two dimensional calculations performed by Allen Kuhl for the TRW experiment (Reference 20) and AFWL personnel for the present experiment need to be studied in detail before further modeling is pursued.

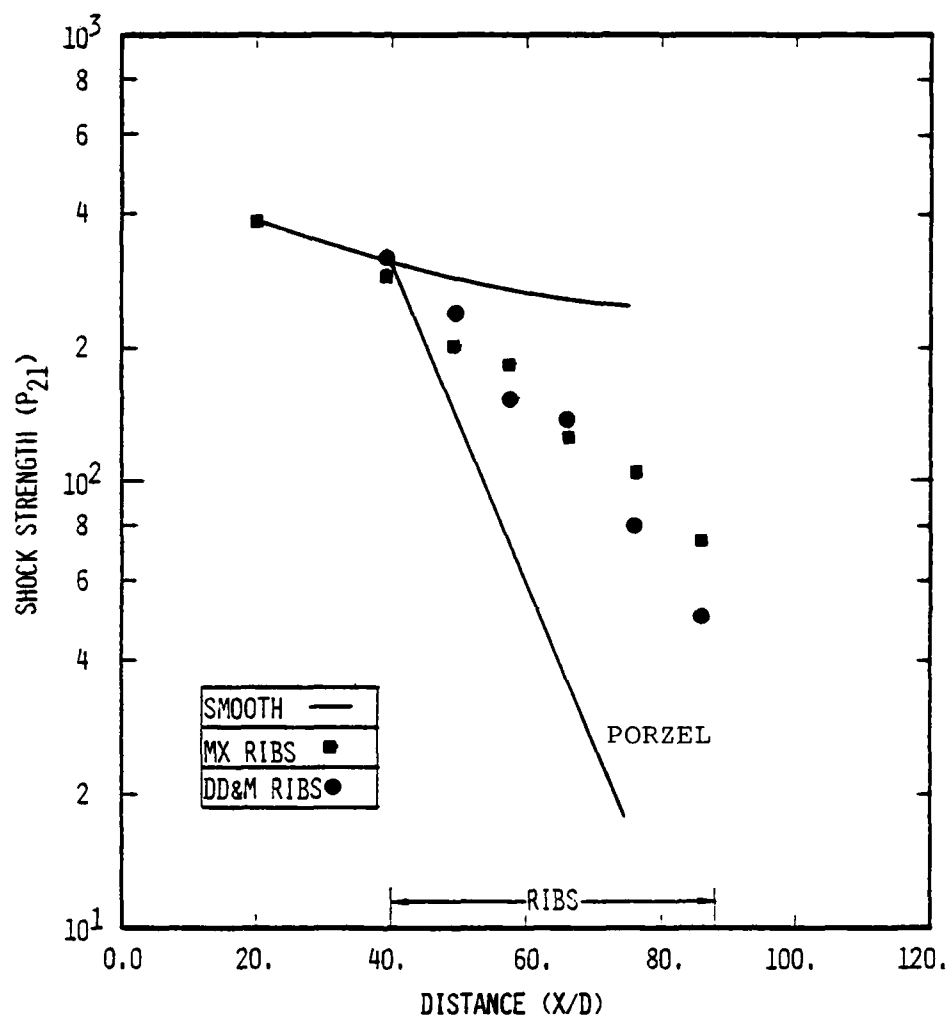


FIGURE 38. COMPARISON OF PORZEL MODEL WITH TYPICAL DATA SET.

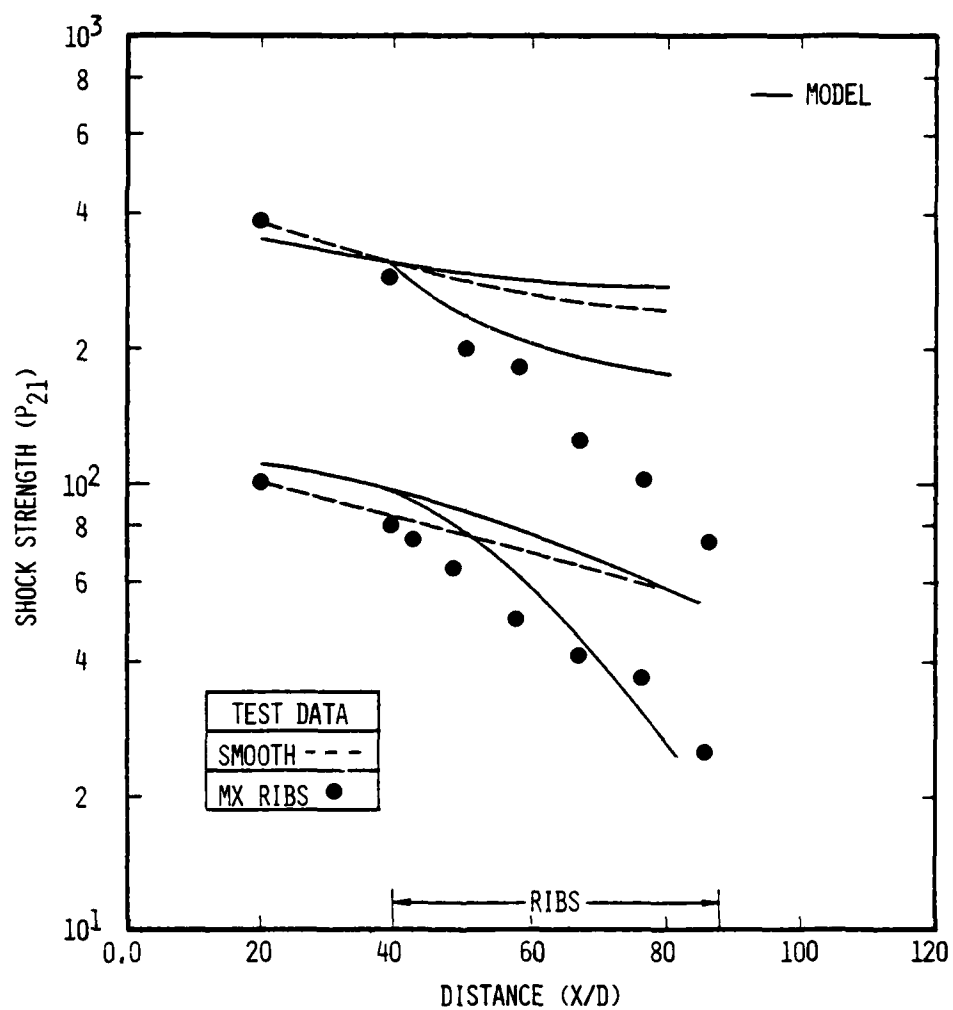


FIGURE 39. ONE DIMENSIONAL RIST CODE PREDICTIONS.

5.0 SUMMARY

A shock tube test program was conducted at the NASA Ames East facility to provide experimental data useful for MX trench prototype assessment. The experiments considered the propagation of strong shock waves in a rigid tube with transverse internal ribs. In addition to standard time of arrival and pressure measurements, custom built diagnostics were assembled to measure wall drag and to provide an optical description of the rib/flowfield interactions. Limited comparisons of test results with prediction techniques were made.

5.1 Conclusions

The conclusions reached during the program are:

- The shock tube test data should scale to the prototype trench. Experiment scales were introduced through geometry and flow Reynolds number. The experiment was performed with a 1:39 geometric scaling of the prototype design. The test Reynolds number was two to four orders of magnitude lower than the prototype. However, no discernable effect of flow Reynolds number on shock attenuation or on pressure waveforms was seen when the Reynolds number was varied by an order of magnitude.
- Shock wave flowfields are two-dimensional in the vicinity of the shock front. Shadowgrams in the shock-front vicinity revealed a complicated but symmetric wave structure composed of a perturbed main shock and reflected shocks originating at each rib. Farther behind the shock ($X/D \sim 7$) the flowfield appeared to take on a quasi-steady character with bow shocks emanating from each rib. Interferograms at $X/D = 7$ produced no evidence of fully developed pipe flow.
- Shock strength attenuation is dependent on initial shock strength and apparently not strongly dependent on rib design. High strength shocks ($P_{21} \geq 300$) decayed to half their smooth wall values in about twenty

diameters; lower shock strengths decayed less rapidly. Entrance effects appeared to play a strong role in the attenuation. An alternate rib geometry optimized (within design constraints) for steady flow wall drag produced a small increase in shock attenuation.

- Two-dimensional flowfield calculations are required to understand the ribbed wall shock attenuation process. The empirical formulation of Porzel and a one-dimensional computer code model do not predict the observed attenuations for high strength shocks. The rapid decrease in shock strengths in the entrance region appears to be two-dimensional and must be replicated before confident prediction of prototype airblast environments can be performed.
- Pressure waveforms in the ribbed tube are characterized by a rise in pressure behind the shock wave. While expansion and venting will probably minimize this effect in the MX trench prototype, the pressure rise should be predicted by computer codes attempting to calculate the experiments.

5.2 Recommendations

As a result of the test program the following recommendations are made to improve the understanding of shock propagation in tubes with transverse ribs:

- Two-dimensional flowfield calculations should be performed for the present experiments and closely examined. Special emphasis should be placed on understanding the entrance region phenomenon to determine how the subsequent attenuation is influenced and whether it is test unique. The calculations should be compared with measured shock time of arrival, shock strength, pressure waveforms, flow structure and density distribution.
- The possibility of constructing simplified models of the shock attenuation process

should be examined. One dimensional computer codes provide a cost effective design tool for computing shock propagation if adequate models can be developed.

- Design tools should be verified with selected experiments. When a shock propagation methodology has been developed, the model can be exercised over a range of shock tube parameters to define experiment conditions which would test the universality of the method.
- A shock attenuation wall treatment for hardened base entrainment systems should be developed and tested based on the knowledge gained. An effective shock attenuation system could relieve the design requirement on blast valves or doors.

6.0 REFERENCES

1. "Estimates of Airblast Environments Inside the MX Buried Trench," A. L. Kuhl, TRW 76.4735.9-72, September 1976.
2. "Airblast Calculations for Advanced Missile System (MX) Support," C. E. Needham and C. Westmorland, AFWL-TR-75-297, February 1976.
3. Personal Communication with A. L. Kuhl and T. Schiffman, October 1977.
4. "Study of Shock Impedance Effects in a Rough Walled Tunnel," F. B. Porzel, Institute for Defense Analysis, Research Paper P-330.
5. "Airblast Propagation Through Tunnels and the Effects of Wall Roughness," A. T. Skjelthorp, et al., Fortifikatorisk Nofat NR 103/75.
6. "Nuclear Weapons Blast Phenomena, Volume II - Blast Wave Interaction, Supplement 1 - Air Blast in Tunnels and Chambers," A. R. Kriebel, DASA 1200-II Supplement 1, October 1972.
7. "RIST Code Operation," R. Issa, SAI IOC LAC-780-077, October 1977.
8. *Boundary Layer Theory*, A. Schlichting, 6th Edition, McGraw Hill Book Company, 1968.
9. "Turbulent Convective Heat Transfer From Rough Surfaces with Two-Dimensional Rectangular Ribs," M. Dalle-Donne and L. Meyer, *International Journal of Heat and Mass Transfer*, Vol. 20, 1977, pp 583-620.
10. "A Method for Computing Rough Wall Heat Transfer Rates on Reentry Nosetips," R. B. Dirling, AIAA 8th Thermophysics Conference, Palm Springs, 1973.
11. "Shock Tube Test Time Limitation Due to Turbulent-Wall Boundary Layer," H. Mirels, *AIAA Journal*, January 1964, pp. 84-93,
12. "The HULL Hydrodynamics Computer Code," B. Chambers, et al., AFWL-TRO76-183, September 1976.

13. "Arc Driver Operation for Either Efficient Energy Transfer or High-Current Generation," R. E. Dannenberg and A. F. Silva, *AIAA Journal*, Vol. 10, No. 12, December 1972, pp. 1563-1564.
14. "Development of Dynamic Discharge Arc Driver with Computer Aided Circuit Simulation," R. E. Dannenberg and P. I. Slapnicar, *AIAA Journal*, Vol. 14, No. 9, September 1976, pp. 1183-1188.
15. "Handbook of Supersonic Aerodynamics, Section 18, Shock Tubes," I. I. Glass and J. G. Hall, NAVORD Report 1488 (Vol. 6), December 1959.
16. "Principles and Applications of Shock Tubes and Shock Tunnels," NASA TM-X-69941, October 1963.
17. "Microsecond Response System for Measuring Shock Arrival by Changes in Stream Electrical Impedance in a Shock Tube," R. E. Dannenberg, and D. E. Humphrey, *Review of Scientific Instruments*, Vol. 39, Nov. 1968, pp. 1191-1196.
18. Personal Communication with Prof. B. Sturtevant, July 1978.
19. "Linear and Nonlinear Waves," Whitham, G. B., Wiley Publications, 1976.
20. "An Experimental Study of the Turbulent Boundary Layer Behind the Initial Shock Wave in a Shock Tube," W. A. Martin, *Journal of the Aero/Space Sciences*, October 1958, pp. 644-652.
21. "Separation of a Supersonic Turbulent Boundary Layer by a Forward Facing Step," Behrens, W., AIAA Paper 72-237.
22. "Observations of Turbulent Reattachment Behind a Axisymmetric Downstream - Facing Step in Supersonic Flow," Roshko, A., and Thomke, G. J., *AIAA Journal*, Vol. 4, Number 5, June 1977, pp. 975-980.
23. "Numerical Calculations of Shock Decay in Rib Walled Ducts," A. L. Kuhl and S. F. Fink, IV, TRW 78.4735.9-14.

APPENDIX A

Time of Arrival Data

Shock wave time of arrival (TOA) data from the MSTIMS system (smooth tube) and from oscilloscope traces of pressure signals (ribbed tubes) are catalogued in Tables A-1 to A-4. Time is measured from 180 μ sec after peak current of the arc discharge and is accurate to 5 μ sec. Station location is measured from the diaphragm. The order of the presentation is consistent with Table 1 in the text.

TABLE A-1. TIME OF ARRIVAL DATA FOR SERIES 1.

Station	Location (Meters)	TOA (μ sec)				
		Run 5	Run 56	Run 57	Run 58	Run 59
C	0.87		362.	362.	378.	358.
D	2.01	758.	727.	734.	745.	732.
E	3.20	1172.	1129.	1162.	1164.	1144.
F	3.88		1359.	1387.	1401.	1369.
Roughness Starts	4.00					
R1	4.06		1424.	1447.	1469.	1434.
O	4.24	1549.				
V2	4.77					
R2	4.81		1717.	1734.	1775.	1722.
F	5.18	1890.				
V3	5.71					
R3	5.75		2184.	2132.	2184.	2139.
Load Cell	5.93					
G	6.38	2340.				
R4	6.69		2554.	2522.	2591.	2524.
R5	7.63		3079.	3047.	3076.	3009.
H	7.66	2835.				
R6	8.56		3719.	3562.	3636.	3559.
Roughness Ends	8.80					
I	8.88	3333.				

TABLE A-2. TIME OF ARRIVAL DATA FOR SERIES 2.

Station	Location (Meters)	TOA (μsec)		
		Run 10	Run 64	Run 63
C	0.87	392.	267.	378.
D	2.01	755.	602.	741.
E	3.20	1139.	983.	1137.
F	3.88		1200.	1362.
Roughness Starts				
R1	4.00			
O	4.06		1258.	1417.
V2	4.24			
R2	4.77			
F	4.81		1532.	1711.
V3	5.18	1818.		
R3	5.71			
	5.75		1933.	2097.
Load Cell	5.93			End Wall @ X = 6.29 TOA = 2332.
G	6.38	2256.		
R4	6.69		2315.	
R5	7.63		2775.	
H	7.66	2733		
R6	8.56		3310.	
Roughness Ends				
I	8.80			
	8.88	3210.		

TABLE A-3. TIME OF ARRIVAL DATA FOR SERIES 3.

Station	Location (Meters)	TOA (μ sec)		
		Run 7	Run 54	Run 60
C	0.87	235.	238.	239.
D	2.01	420.	427.	432.
E	3.20	627.	638.	650.
F	3.88		757.	773.
Roughness Starts	4.00			
R1	4.06		788.	815.
O	4.24	820.		
V2	4.77			
R2	4.81		947.	977.
F	5.18	1001.		
V3	5.71			
R3	5.75		1203.	1200.
Loca Cell	5.93			
G	6.38	1245.		
R4	6.69		1372.	1443.
R5	7.63		1682.	1718.
H	7.66			
R6	8.56		2097.	2048.
Roughness Ends	8.80			
I	8.88	1774.		

TABLE A-4. TIME OF ARRIVAL DATA FOR SERIES 4.

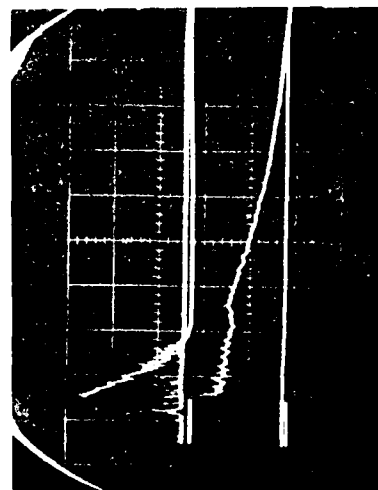
Station	Location (Meters)	TOA (μ sec)		
		Run 50	Run 52	Run 61
C	0.87	211.	198.	213.
D	2.01	362.	344.	362.
E	3.20	509.	495.	508.
F	3.88	586.	576.	589.
Roughness Starts	4.00			
R1	4.06		595.	613.
O	4.24			
F	4.57	668.		
V2	4.77			
R2	4.81		694.	712.
V3	5.71			
R3	5.75		835.	848.
G	5.77	823.		
Load Cell	5.93			
R4	6.69		981.	989.
H	7.05	984.		
R5	7.63		1156.	1159.
I	8.25	1156.		
R6	8.56		1396.	1384.
Roughness Ends	8.80			

Blank

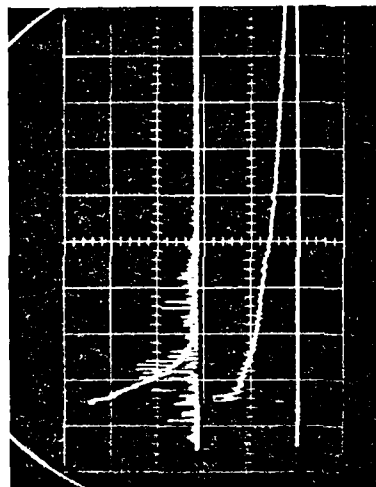
APPENDIX B

Pressure Data

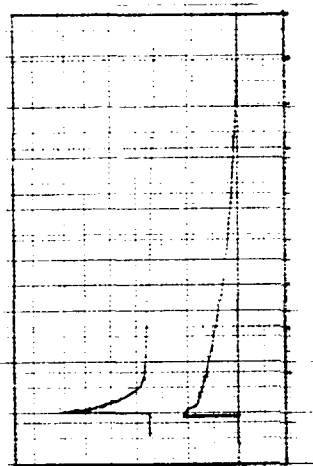
Signals from the pressure transducers were displayed on Tektronix oscilloscopes and recorded on Polaroid film. Polaroid reproductions for the final runs are presented in Figures B-1 through B-15; corresponding identification and sensitivity information is catalogued in Tables B-1 through B-15. Shock wave pressure ratio measurements determined from the initial signal deflection peak (the midpoint of the trace was used) are presented in Tables B-16 through B-19 consistent with Table 1 of the text. The uncertainty in reading the signal from the photographs is taken to be the ratio of half the beam width to the initial beam deflection which is generally less than 10 percent.



5-4



5-5



5-6

FIGURE B-1. PRESSURE SIGNALS FOR RUN 5.

TABLE B-1. OSCILLISCOPE SETTINGS FOR RUN 5.

Polaroid	Source	Beam	Sensitivity (mv/psi)	Vertical (v/cm)	Horizontal (μ s/cm)
5-4	TOA - D	U	-	2.0	200.
	Pressure - D	L	1.04	1.0	200.
5-5	TOA - F	U	-	2.0	200.
	Pressure - F	L	1.06	1.0	200.
5-6	TOA - H	U	-	2.0	200.
	Pressure - H	L	1.07	1.0	200.

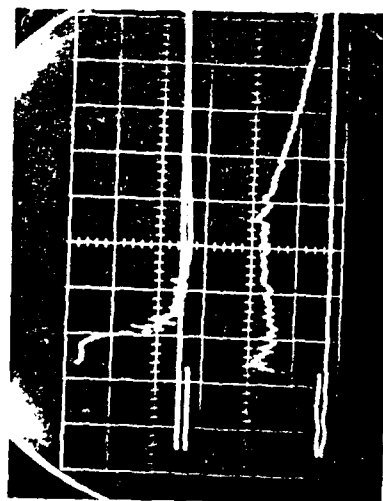
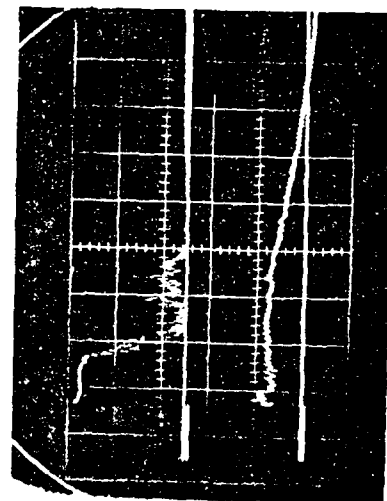
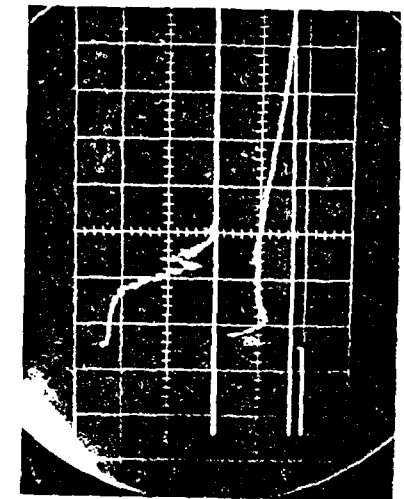


FIGURE B-2. PRESSURE SIGNALS FOR RUN 7.

AD-A085 725

SCIENCE APPLICATIONS INC EL SEGUNDO CALIF
AIRBLAST ATTENUATION EXPERIMENTS FOR THE M-X TRENCH.(U)
DEC 78 D T HOVE, J E CRAIG
SAI-79-546-LA

F/G 18/3

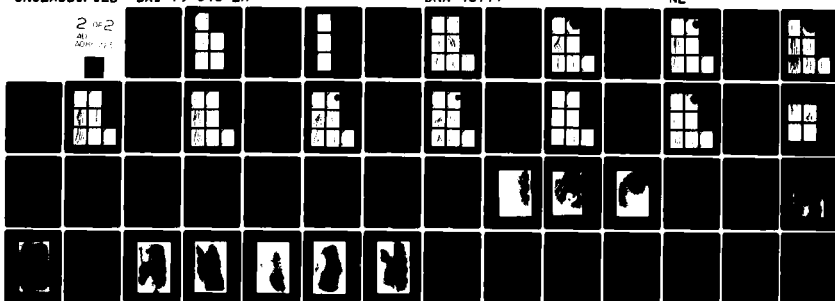
UNCLASSIFIED

DNA001-77-C-0280

DNA-4677T

NL

2 of 2
DU
ADP 17-1



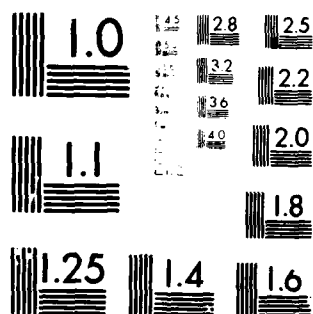
END

DATE

FILMED

7-80

DTIC



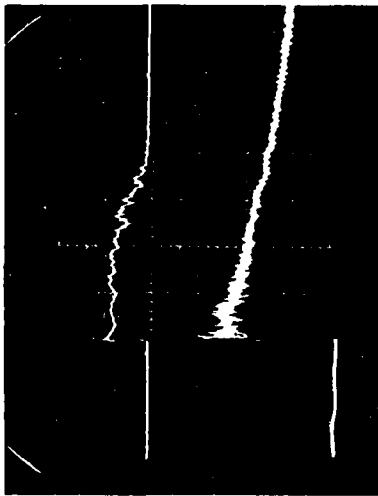
MICROCOPY RESOLUTION TEST CHART
NATIONAL BUREAU OF STANDARDS-1963-A

TABLE B-2. OSCILLOSCOPE SETTINGS FOR RUN 7.

Polaroid	Source	Beam	Sensitivity (mv/psi)	Vertical (v/cm)	Horizontal (μ s/cm)
7-4	TOA - D	U	-	2.0	200.
	Pressure - D	L	1.04	0.5	200.
7-5	TOA - F	U	-	2.0	200.
	Pressure - F	L	1.06	0.5	200.
7-6	TOA - H	U	-	2.0	200.
	Pressure - H	L	1.07	0.5	200.



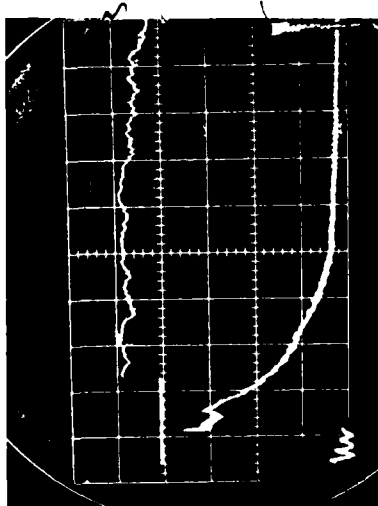
10-4



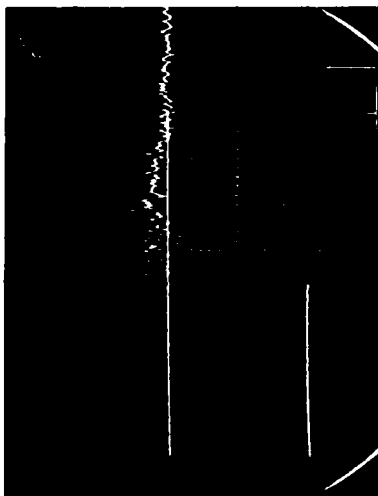
10-5



10-6



10-7

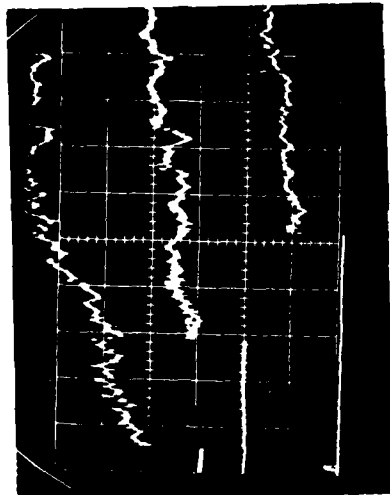


10-8

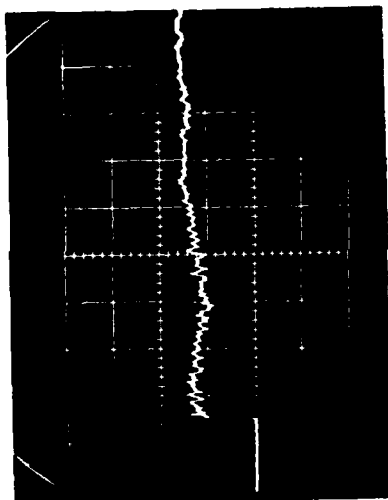
FIGURE B-3. PRESSURE SIGNALS FOR RUN 10.

TABLE B-3. OSCILLOSCOPE SETTINGS FOR RUN 10.

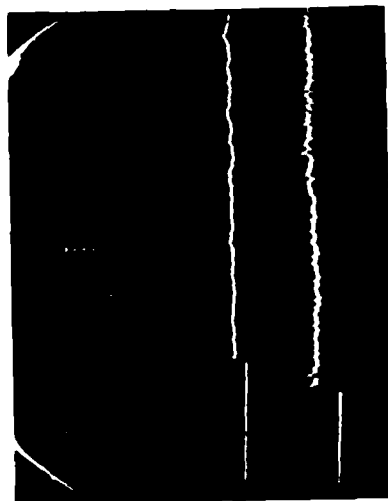
Polaroid	Source	Beam	Sensitivity (mv/psi)	Vertical (v/cm)	Horizontal (μ s/cm)
10-4	TOA - D	U	-	5.0	200.
	Pressure - D	L	1.04	0.05	200.
10-5	TOA - F	U	-	5.0	200.
	Pressure - F	L	1.06	0.05	200.
10-6	TOA-H	U	-	5.0	200.
	Pressure - H	L	1.07	0.05	200.
10-7	TOA - C	U	-	5.0	200.
	Pressure - D	L	1.04	0.05	1000.
10-8	Pressure - D	U	1.04	0.05	10.
	Pressure - D	L	1.04	0.05	20.



50-6



50-5

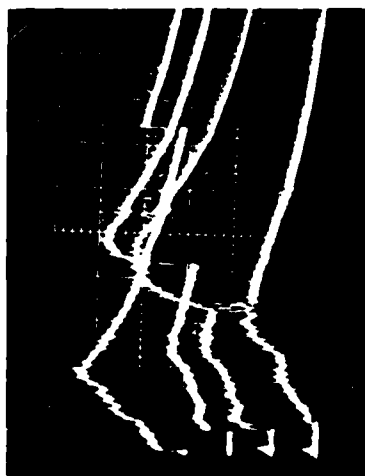


50-4

FIGURE B-4. PRESSURE SIGNALS FOR RUN 50.

TABLE B-4. OSCILLISCOPE SETTINGS FOR RUN 50.

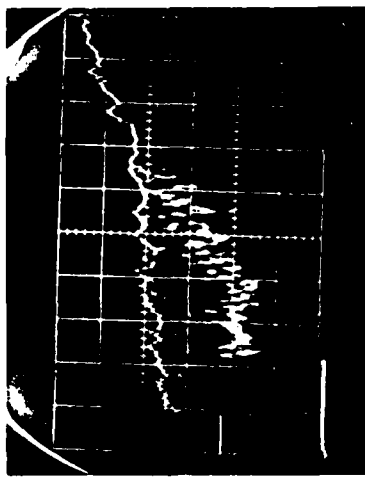
Polaroid	Source	Beam	Sensitivity (mv/psi)	Vertical (v/cm)	Horizontal (μ s/cm)
50-4	Pressure - D	U	1.03	0.5	20.
	Pressure - F	L	1.00	0.2	20.
50-5	Pressure - G	U	5.22	0.5	20.
	Pressure - D	U1	1.03	0.1	100.
50-6	Pressure - F	U2	1.00	0.1	100.
	Pressure - G	L	5.22	0.5	100.



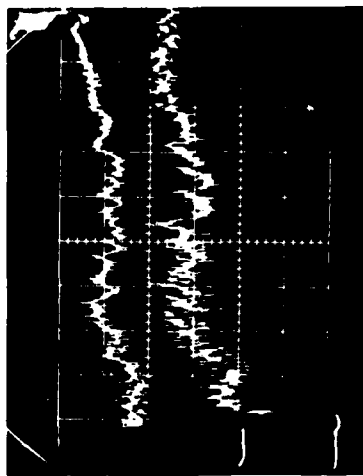
52-1



52-2



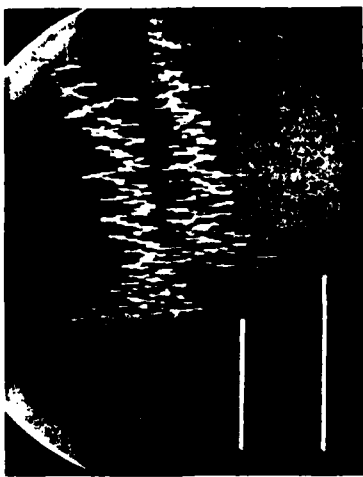
52-3



52-4



52-5



52-6



52-7

FIGURE B-5. PRESSURE SIGNALS FOR RUN 52.

TABLE B-5. OSCILLISCOPE SETTINGS FOR RUN 52.

Polaroid	Source	Beam	Sensitivity (mv/psi)	Vertical (v/cm)	Horizontal (μ s/cm)
52-1	Pressure - D	U1	1.04	0.2	500.
	Pressure - F	U2	1.04	0.2	500.
	Pressure - R1	L1	1.07	0.2	500.
	Pressure - R2	L2	1.06	0.5	500.
52-2	Pressure - R3	U1	1.07	0.2	500.
	Pressure - R4	U2	5.46	1.0	500.
	Pressure - R5	L1	4.97	1.0	500.
	Pressure - R6	L2	5.40	0.5	500.
52-3	Pressure - D	U	1.06	0.1	50.
	Pressure - R2	L	1.06	0.05	50.
52-4	Pressure - F	U	1.04	0.05	50.
	Pressure - R1	L	1.07	0.05	50.
52-5	Pressure - V3	U	1.06	0.05	50.
	Pressure - R3	L	1.07	0.05	50.
52-6	Pressure - R4	U	5.46	0.1	50.
	Pressure - R5	L	4.97	0.05	50.
52-7	Pressure - R6	U	5.40	0.05	50.

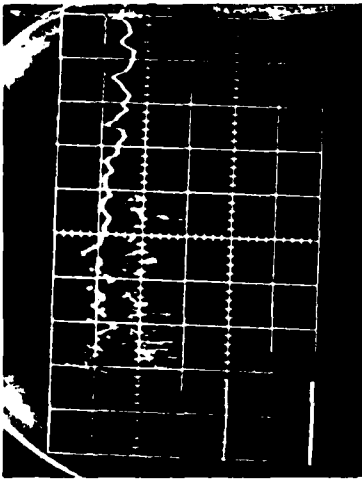
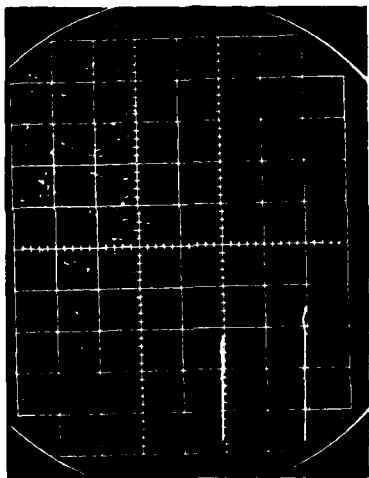
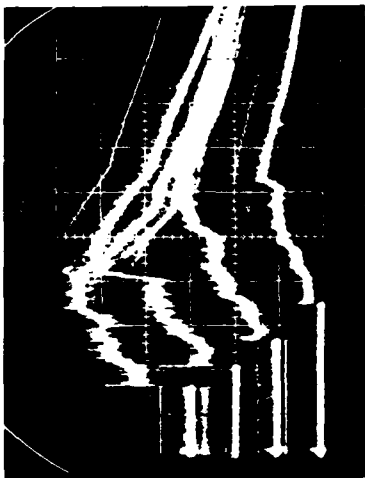
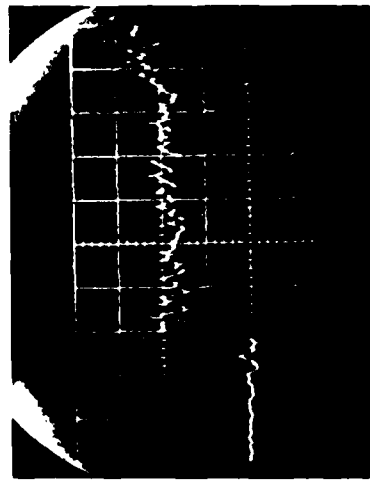
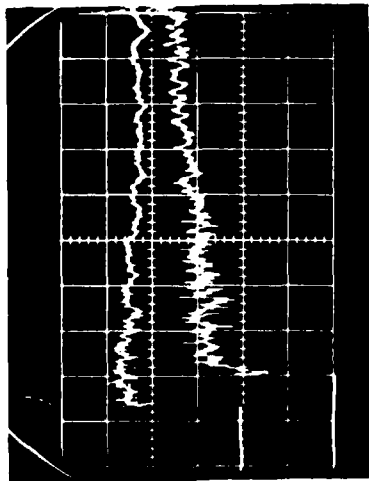
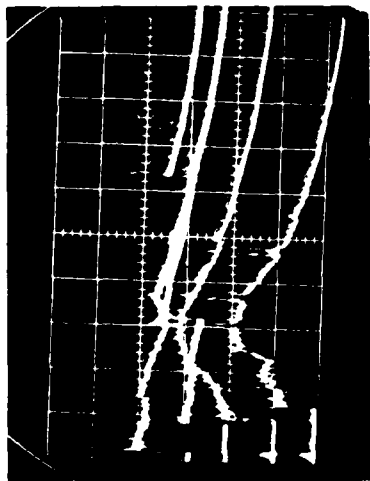
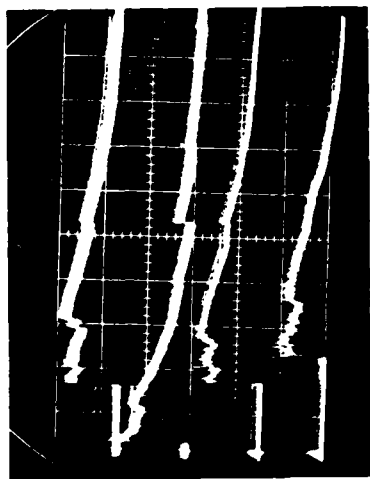


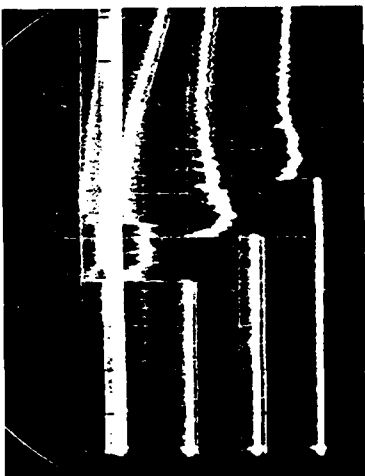
FIGURE B-6. PRESSURE SIGNALS FOR RUN 54.

TABLE B-6. OSCILLOSCOPE SETTINGS FOR RUN 54.

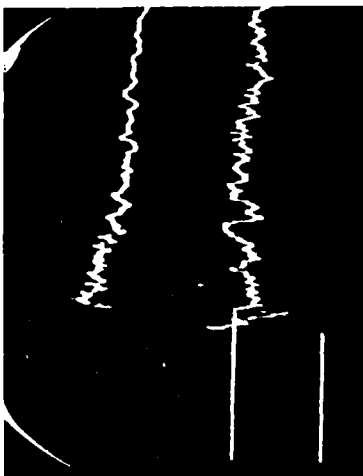
Polaroid	Source	Beam	Sensitivity (mv/psi)	Vertical (v/cm)	Horizontal (μ s/cm)
54-1	Pressure - D	U1	1.06	0.5	500.
	Pressure - F	U2	1.04	0.5	500.
	Pressure - R1	L1	1.07	0.5	500.
	Pressure - R2	L2	1.06	0.5	500.
54-2	Pressure - R3	U1	1.07	0.2	500.
	Pressure - R4	U2	5.46	1.0	500.
	Pressure - R5	L1	4.97	1.0	500.
	Pressure - R6	L2	5.40	1.0	500.
54-3	Pressure - D	U	1.06	0.2	50.
	Pressure - R2	L	1.06	0.1	50.
54-4	Pressure - F	U	1.04	0.2	50.
	Pressure - R1	L	1.07	0.2	50.
54-5	Pressure - V3	U	1.06	0.05	50.
	Pressure - R3	L	1.07	0.05	50.
54-6	Pressure - R4	U	5.46	0.5	50.
	Pressure - R5	L	4.97	0.2	50.
54-7	Pressure - R6	U	5.40	0.2	50



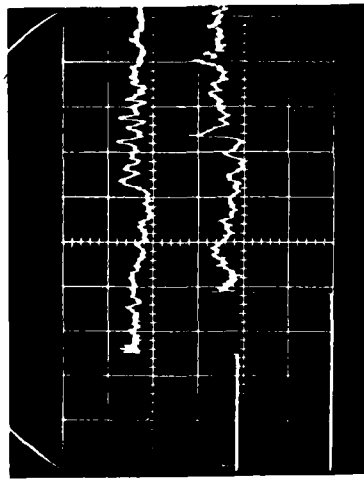
56-1



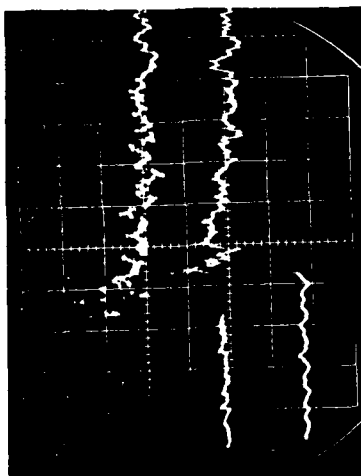
56-2



56-3



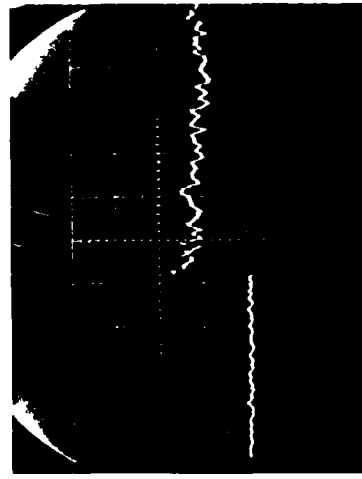
56-4



56-5



56-6



56-7

FIGURE B-7. PRESSURE SIGNALS FOR RUN 56.

TABLE B-7. OSCILLOSCOPE SETTINGS FOR RUN 56.

Polaroid	Source	Beam	Sensitivity (mv/psi)	Vertical (v/cm)	Horizontal (μ s/cm)
56-1	Pressure - F	U1	1.04	1.0	500.
	Pressure - D	U2	1.06	1.0	500.
	Pressure - R1	L1	1.07	1.0	500.
	Pressure - R2	L2	1.06	1.0	500.
56-2	Pressure - R3	U1	1.07	1.0	500.
	Pressure - R4	U2	5.46	2.0	500.
	Pressure - R5	L1	4.97	2.0	500.
	Pressure - R6	L2	5.40	2.0	500.
56-3	Pressure - D	U	1.06	0.5	50.
	Pressure - R2	L	1.06	0.5	50.
56-4	Pressure - F	U	1.04	0.5	50.
	Pressure - R1	L	1.07	0.5	50.
56-5	Pressure - V3	U	1.06	0.5	50.
	Pressure - R3	L	1.07	0.5	50.
56-6	Pressure - R4	U	5.46	1.0	50.
	Pressure - R5	L	4.97	1.0	50.
56-7	Pressure - R6	U	5.40	1.0	50.

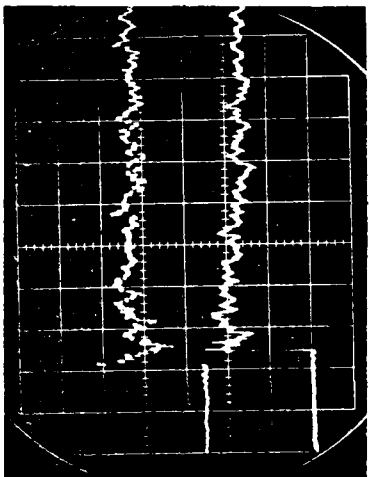
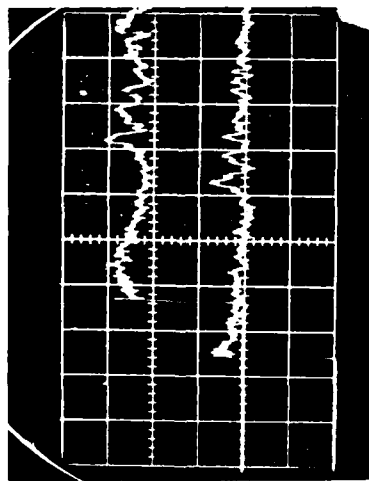
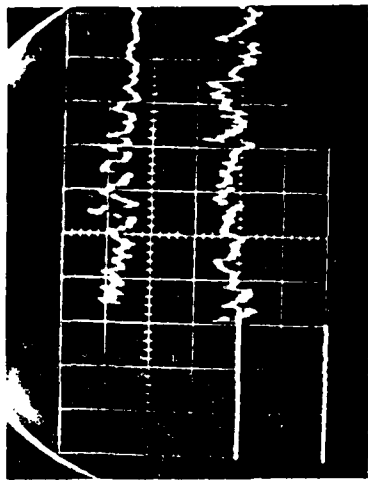
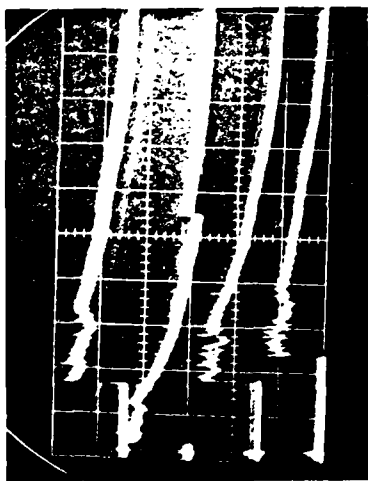
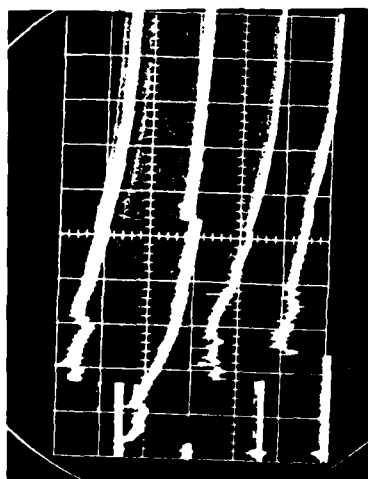


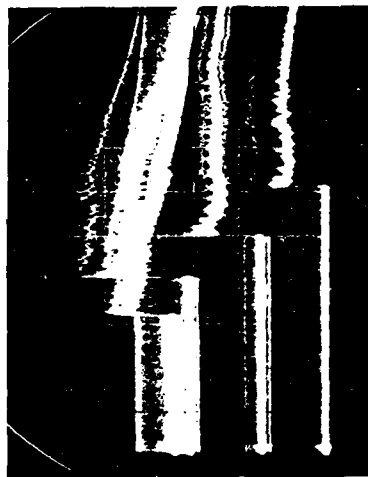
FIGURE B-8. PRESSURE SIGNALS FOR RUN 57.

TABLE B-8. OSCILLISCOPE SETTINGS FOR RUN 57.

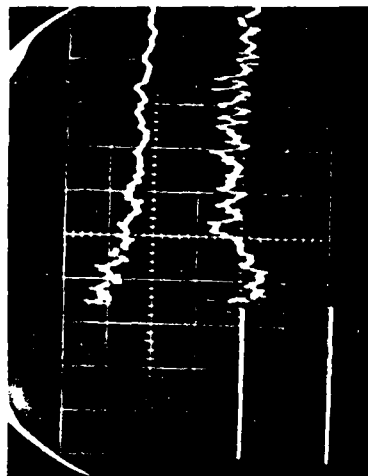
Polaroid	Source	Beam	Sensitivity (mv/psi)	Vertical (v/cm)	Horizontal (μ s/cm)
57-1	Pressure - F	U1	1.04	1.0	500.
	Pressure - D	U2	1.06	1.0	500.
	Pressure - R1	L1	1.07	1.0	500.
	Pressure - R2	L2	1.06	1.0	500.
57-2	Pressure - R3	U1	1.07	1.0	500.
	Pressure - R4	U2	5.46	2.0	500.
	Pressure - R5	L1	4.97	2.0	500.
	Pressure - R6	L2	5.40	2.0	500.
57-3	Pressure - D	U	1.06	0.5	50.
	Pressure - R2	L	1.06	0.5	50.
57-4	Pressure - R1	U	1.04	0.5	50.
	Pressure - F	L	1.07	0.5	50.
57-5	Pressure - V3	U	1.06	0.5	50.
	Pressure - R3	L	1.07	0.5	50.
57-6	Pressure - R4	U	5.46	2.0	50.
	Pressure - R5	L	4.97	1.0	50.
57-7	Pressure - R6	U	5.40	1.0	50.



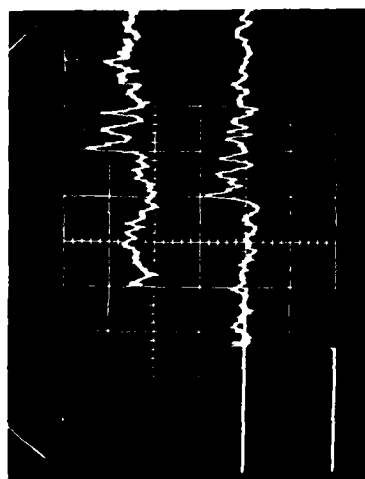
58-1



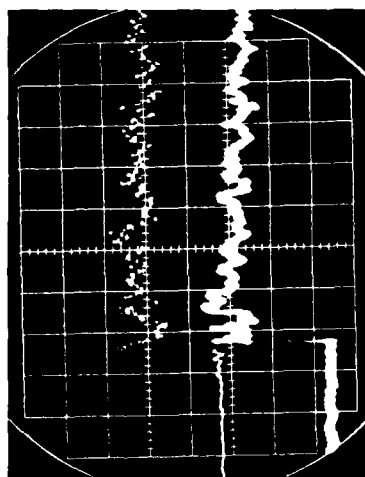
58-2



58-3



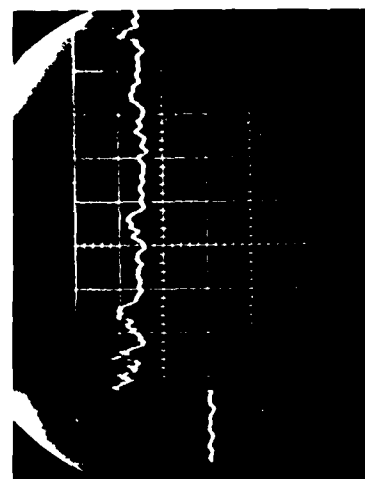
58-4



58-5



58-6



58-7

FIGURE B-9. PRESSURE SIGNALS FOR RUN 50.

TABLE B-9. OSCILLISCOPE SETTINGS FOR RUN 58.

Polaroid	Source	Beam	Sensitivity (mv/psi)	Vertical (v/cm)	Horizontal (μ s/cm)
58-1	Pressure - F	U1	1.04	1.0	500.
	Pressure - D	U2	1.06	1.0	500.
	Pressure - R1	L1	1.07	1.0	500.
	Pressure - R2	L2	1.06	1.0	500.
58-2	Pressure - R3	U1	1.07	1.0	500.
	Pressure - R4	U2	5.46	2.0	500.
	Pressure - R5	L1	4.97	2.0	500.
	Pressure - R6	L2	5.40	2.0	500.
58-3	Pressure - D	U	1.06	0.5	50.
	Pressure - R2	L	1.06	0.5	50.
58-4	Pressure - R1	U	1.04	0.5	50.
	Pressure - F	L	1.07	0.5	50.
58-5	Pressure - V3	U	1.06	0.5	50.
	Pressure - R3	L	1.07	0.5	50.
58-6	Pressure - R4	U	5.46	1.0	50.
	Pressure - R5	L	4.97	1.0	50.
58-7	Pressure - R6	U	5.40	1.0	50.

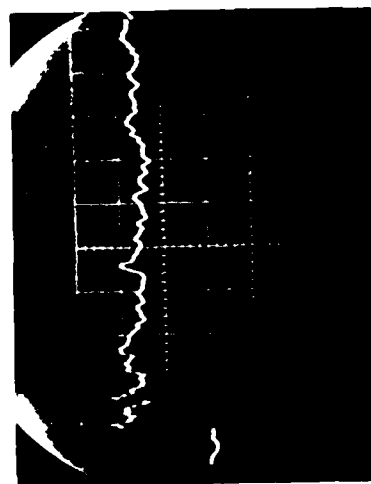
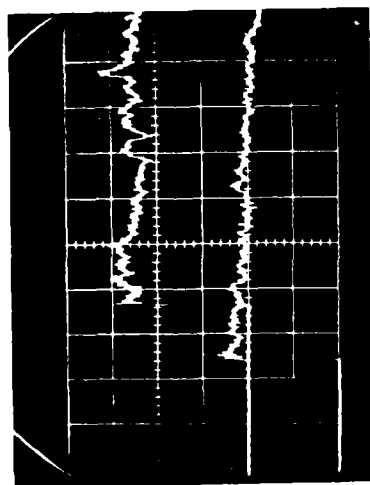
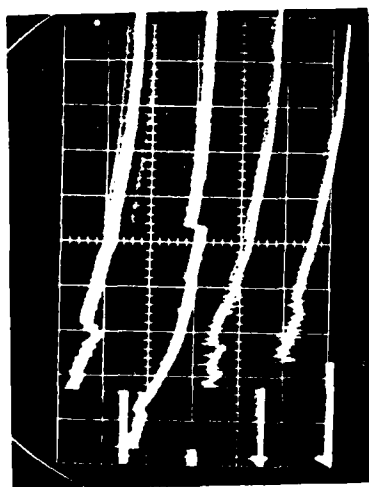
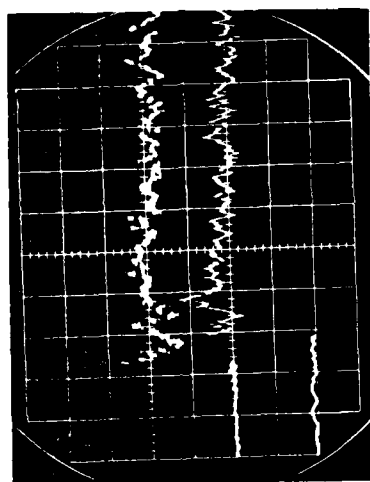
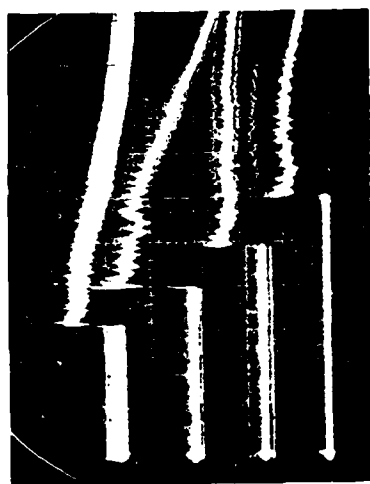
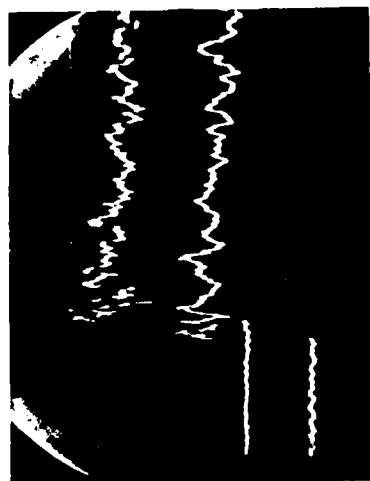
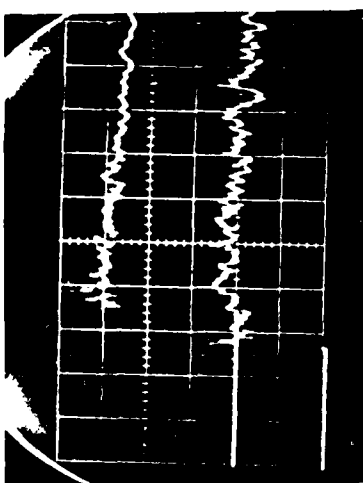


FIGURE B-10. PRESSURE SIGNALS FOR RUN 59.

TABLE B-10. OSCILLOSCOPE SETTINGS FOR RUN 59.

Polaroid	Source	Beam	Sensitivity (mv/psi)	Vertical (v/cm)	Horizontal (μ s/cm)
59-1	Pressure - F	U1	1.04	1.0	500.
	Pressure - D	U2	1.06	1.0	500.
	Pressure - R1	L1	1.07	1.0	500.
	Pressure - R2	L2	1.06	1.0	500.
59-2	Pressure - R3	U1	1.07	1.0	500.
	Pressure - R4	U2	5.46	2.0	500.
	Pressure - R5	L1	4.97	2.0	500.
	Pressure - R6	L2	5.40	2.0	500.
59-3	Pressure - D	U	1.06	0.5	50.
	Pressure - R2	L	1.06	0.5	50.
59-4	Pressure - R1	U	1.04	0.5	50.
	Pressure - F	L	1.07	0.5	50.
59-5	Pressure - V3	U	1.06	0.5	50.
	Pressure - R3	L	1.07	0.5	50.
59-6	Pressure - R4	U	5.46	1.0	50.
	Pressure - R5	L	4.97	1.0	50.
59-7	Pressure - R6	U	5.40	1.0	50.

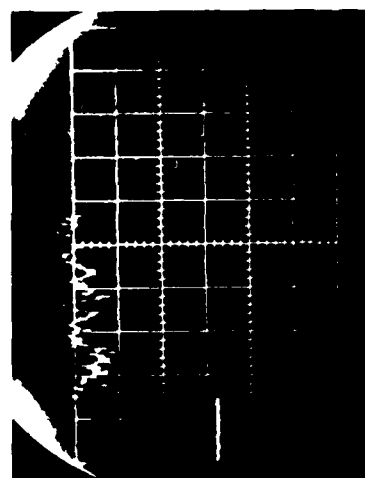
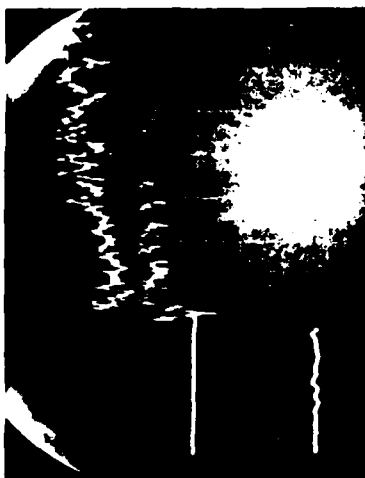
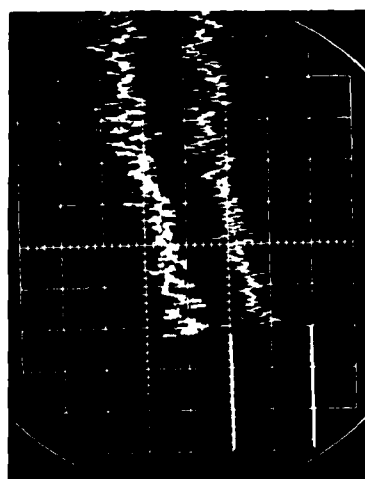
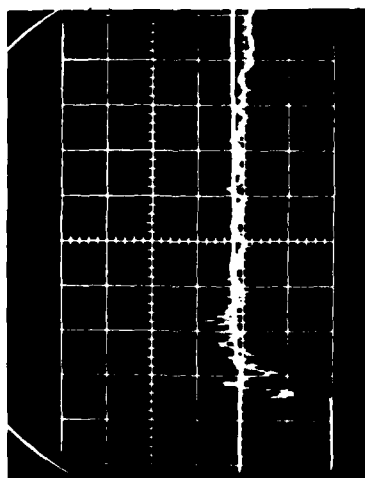
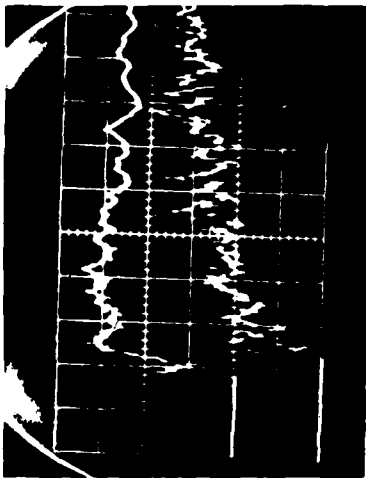
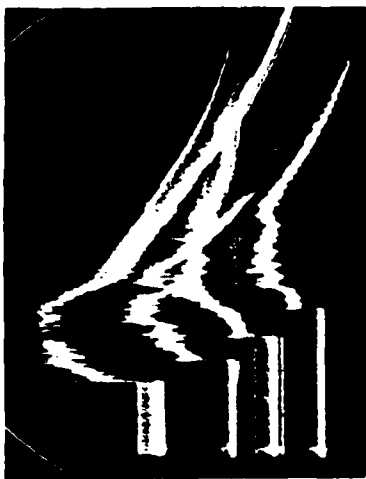
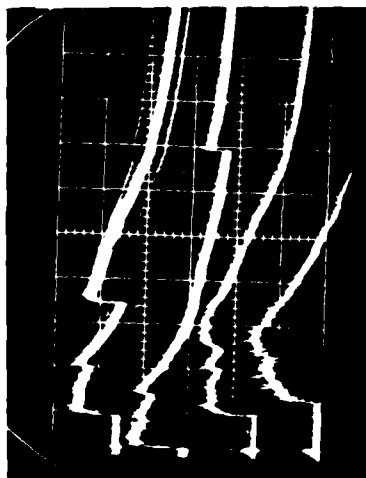


FIGURE B-110. PRESSURE SIGNALS FOR RUN 60.

TABLE B-11. OSCILLOSCOPE SETTINGS FOR RUN 60.

Polaroid	Source	Beam	Sensitivity (mv/psi)	Vertical (v/cm)	Horizontal (μ s/cm)
60-1	Pressure - F	U1	1.04	0.5	500.
	Pressure - D	U2	1.06	0.5	500.
	Pressure - R1	L1	1.07	0.5	500.
	Pressure - R2	L2	1.06	0.5	500.
60-2	Pressure - R3	U1	1.07	0.2	500.
	Pressure - R4	U2	5.46	1.0	500.
	Pressure - R5	L1	4.97	1.0	500.
	Pressure - R6	L2	5.40	1.0	500.
60-3	Pressure - D	U	1.06	0.2	50.
	Pressure - R2	L	1.06	0.2	50.
60-4	Pressure - R1	U	1.04	0.2	50.
	Pressure - F	L	1.07	0.2	50.
60-5	Pressure - V3	U	1.06	0.2	50.
	Pressure - R3	L	1.07	0.2	50.
60-6	Pressure - R4	U	5.46	0.5	50.
	Pressure - R5	L	4.97	0.2	50.
60-7	Pressure - R6	U	5.40	0.2	50.

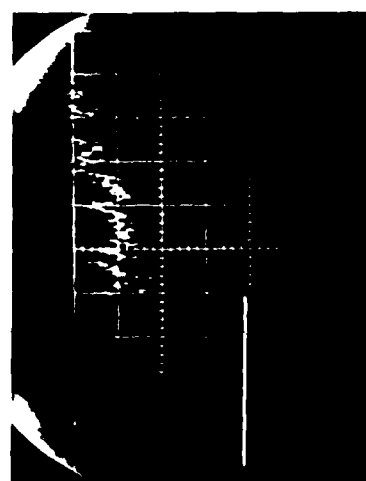
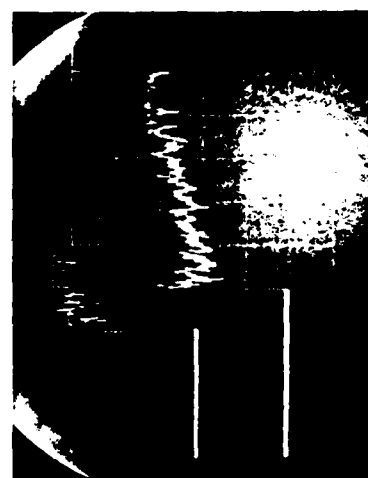
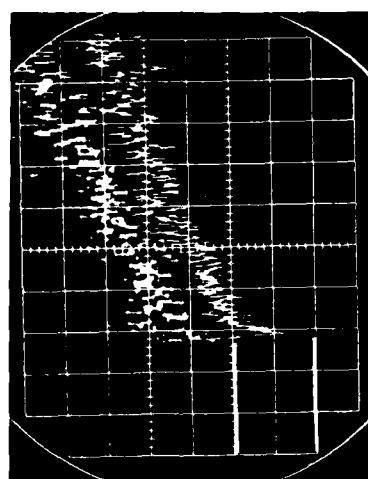
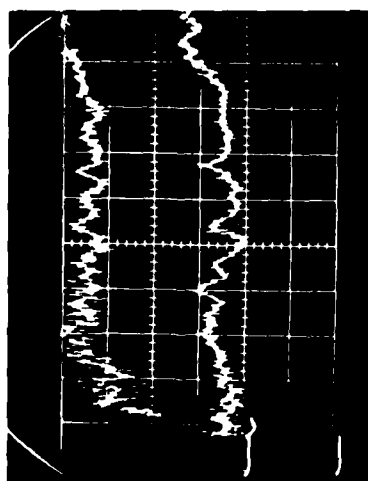
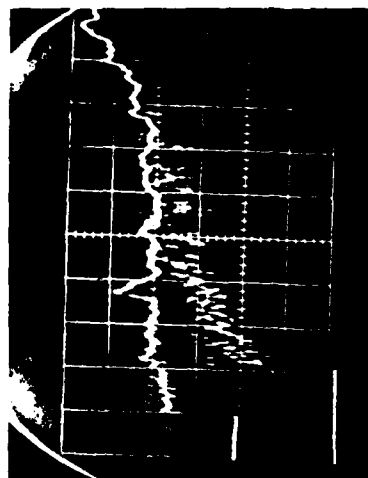
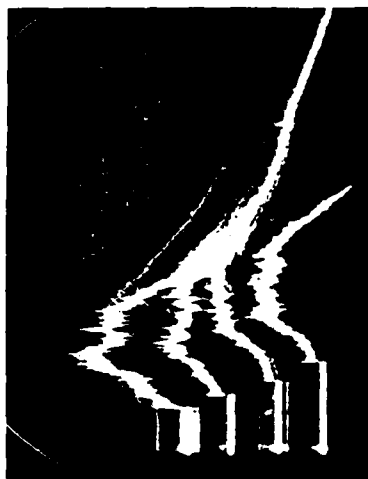
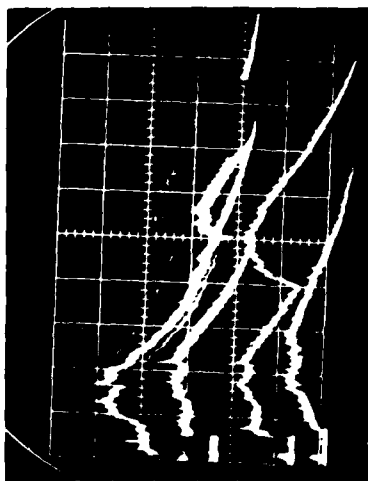


FIGURE B-12. PRESSURE SIGNALS FOR RUN 61.

TABLE B-12. OSCILLOSCOPE SETTINGS FOR RUN 61.

Polaroid	Source	Beam	Sensitivity (mv/psi)	Vertical (v/cm)	Horizontal (μ s/cm)
61-1	Pressure - D	U1	1.03	0.2	500.
	Pressure - F	U2	1.00	0.2	500.
	Pressure - R1	L1	1.03	0.2	500.
	Pressure - R2	L2	1.02	0.5	500.
61-2	Pressure - R3	U1	1.03	0.2	500.
	Pressure - R4	U2	5.37	1.0	500.
	Pressure - R5	L1	4.75	1.0	500.
	Pressure - R6	L2	5.22	0.5	500.
61-3	Pressure - D	U	1.03	0.1	50.
	Pressure - R2	L	1.02	0.05	50.
61-4	Pressure - R1	U	1.00	0.05	50.
	Pressure - F	L	1.03	0.05	50.
61-5	Pressure - V3	U	1.03	0.05	50.
	Pressure - R3	L	1.03	0.05	50.
61-6	Pressure - R4	U	5.37	0.1	50.
	Pressure - R5	L	4.75	0.1	50.
61-7	Pressure - R6	U	5.22	0.05	50.

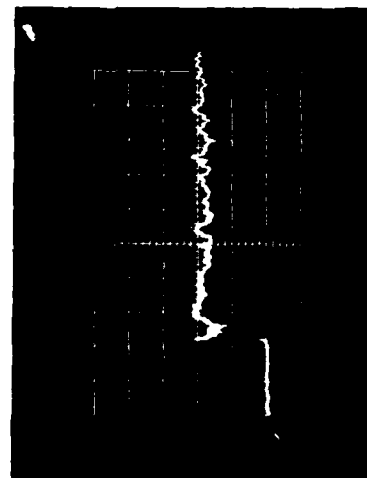
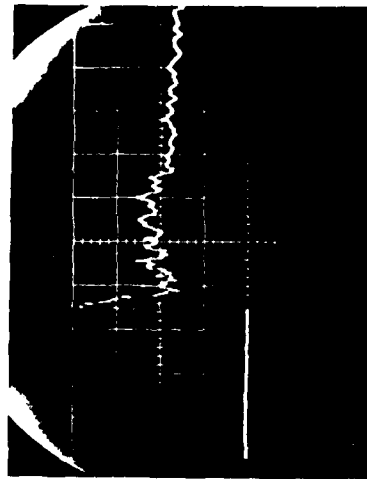
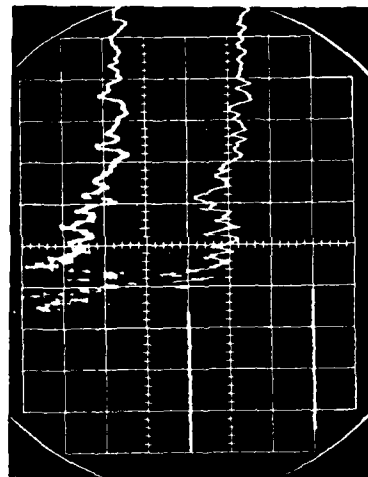
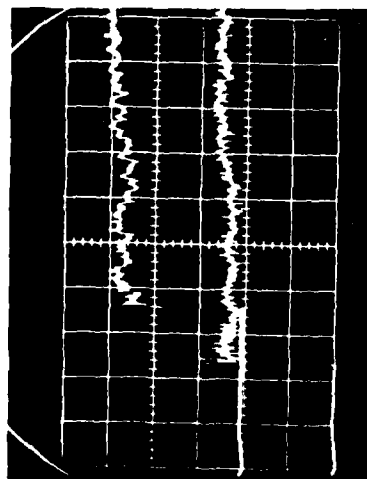
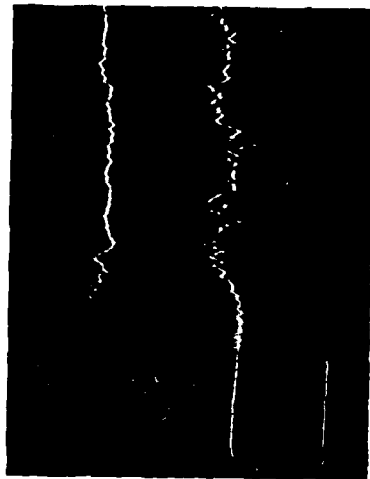
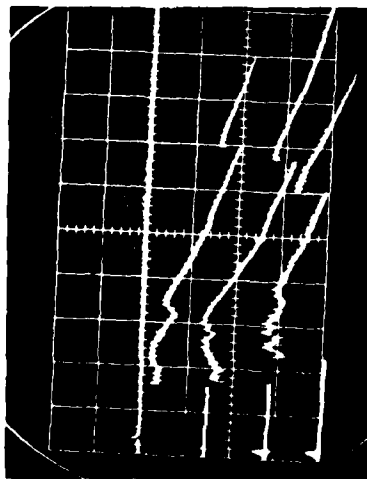


FIGURE B-13. PRESSURE SIGNALS FOR RUN 63.

TABLE B-13. OSCILLOSCOPE SETTINGS FOR RUN 60.

Polaroid	Source	Beam	Sensitivity (mv/psi)	Vertical (v/cm)	Horizontal (μ s/cm)
63-1	Pressure - D	U1	1.03	0.1	500.
	Pressure - F	U2	1.00	0.1	500.
	Pressure - R1	L1	1.03	0.1	500.
	Pressure - R2	L2	1.02	0.1	500.
63-2	Pressure - R3	U	1.02	0.05	500.
	Pressure - EW1	L	5.37	1.0	500.
63-3	Pressure - D	U	1.03	0.05	50.
	Pressure - R2	L	1.02	0.05	50.
63-4	Pressure - R1	U	1.00	0.05	50.
	Pressure - F	L	1.03	0.05	50.
63-5	Pressure - EW1	U	5.37	1.0	50.
	Pressure - EW2	L	4.75	1.0	50.
63-6	Pressure - EW3	U	5.22	1.0	50.
63-7	Pressure - R3	U	1.02	0.05	50.

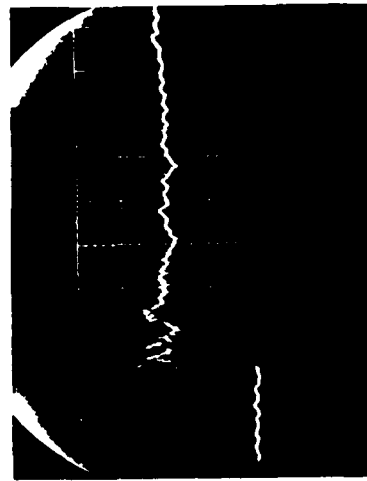
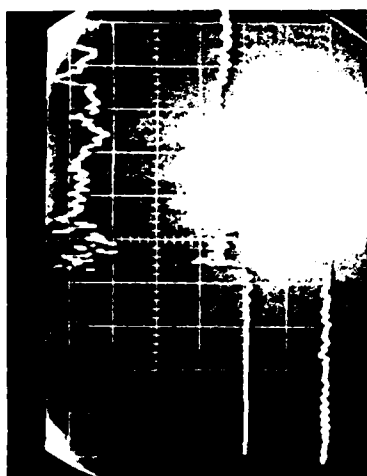
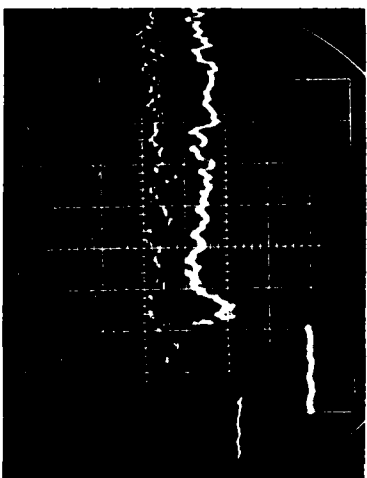
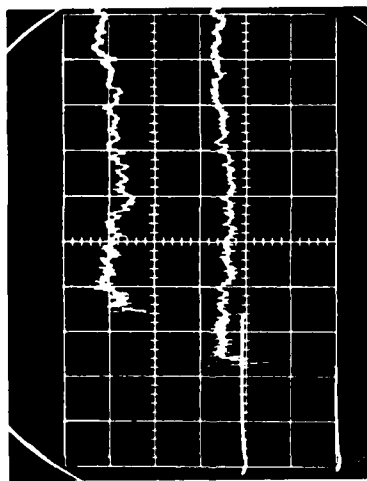
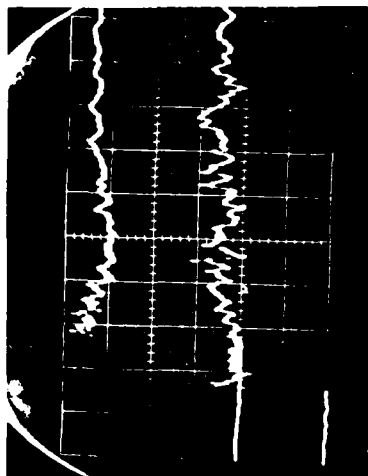
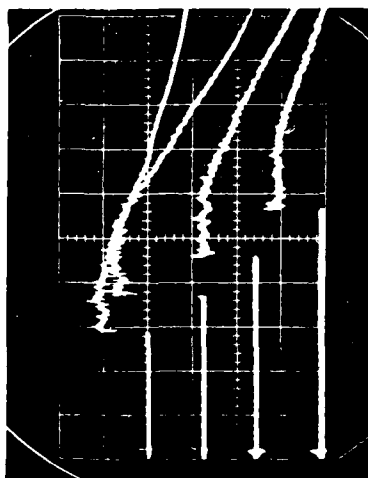
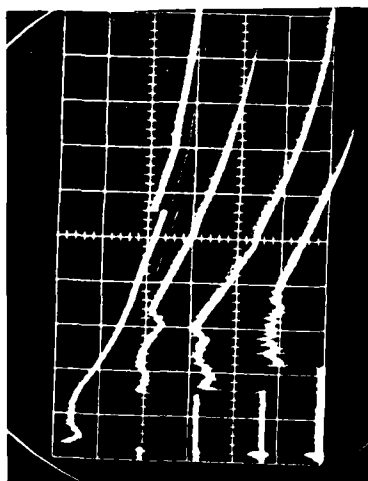
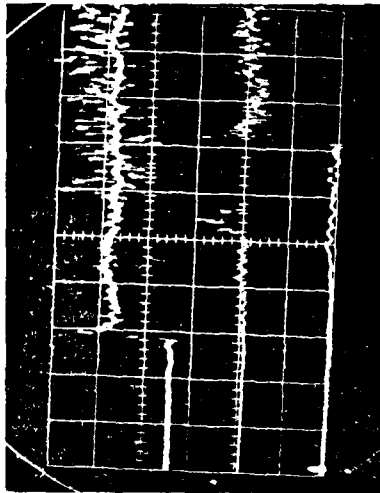


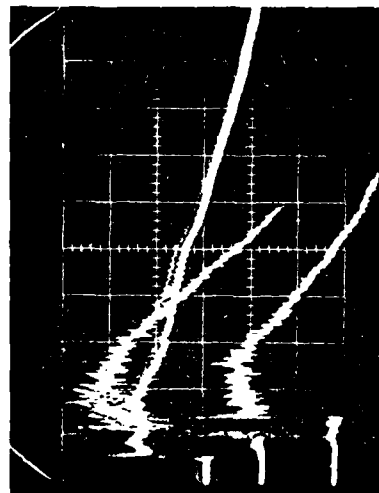
FIGURE B-14. PRESSURE SIGNALS FOR RUN 64.

TABLE B-14. OSCILLOSCOPE SETTINGS FOR RUN 64.

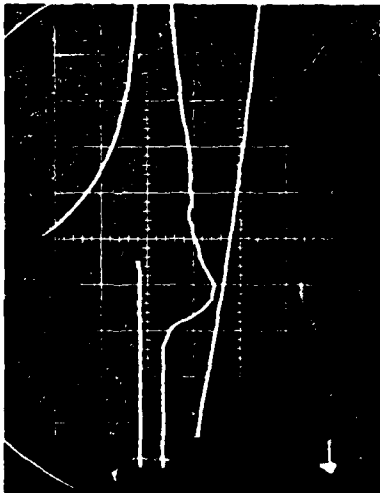
Polaroid	Source	Beam	Sensitivity (mv/psi)	Vertical (v/cm)	Horizontal (μ s/cm)
64-1	Pressure - D	U1	1.03	0.1	500.
	Pressure - F	U2	1.00	0.1	500.
	Pressure - R1	L1	1.03	0.1	500.
	Pressure - R2	L2	1.02	0.1	500.
64-2	Pressure - R3	U1	1.02	0.1	500.
	Pressure - R4	U2	5.37	0.2	500.
	Pressure - R5	L1	4.75	0.2	500.
	Pressure - R6	L2	5.22	0.2	500.
64-3	Pressure - D	U	1.03	0.05	50.
	Pressure - R2	L	1.02	0.05	50.
64-4	Pressure - R1	U	1.00	0.05	50.
	Pressure - F	L	1.03	0.05	50.
64-5	Pressure - V3	U	1.03	0.05	50.
	Pressure - R3	L	1.02	0.05	50.
64-6	Pressure - R4	U	5.37	0.10	50.
	Pressure - R5	L	4.75	0.1	50.
64-7	Pressure - R6	U	5.22	0.1	50.



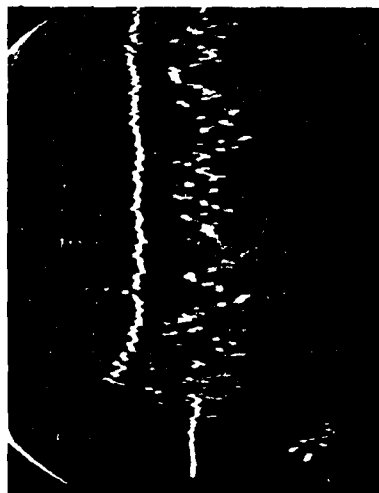
46-5



46-7



46-4



46-6

FIGURE B-15. PRESSURE SIGNALS FOR RUN 46.

TABLE B-15. OSCILLOSCOPE SETTINGS FOR RUN 46.

Polaroid	Source	Beam	Sensitivity (mv/psi)	Vertical (v/cm)	Horizontal (μ s/cm)
46-4	Laser Detector	U1	NA	0.5	200.
	Luminosity Detector	U2	NA	0.5	200.
	Laser Detector	L	NA	0.5	20.
46-5	Pressure - TS1	U1	5.37	0.50	100.
	Pressure - TS2	U2	4.75	0.20	100.
	Pressure - TS3	L	5.22	0.05	100.
46-6	Pressure - TS1	U	5.37	0.50	20.
	Pressure - TS2	L	4.75	0.20	20.
46-7	Pressure - TS1	U1	5.37	0.50	500.
	Pressure - TS2	U2	4.75	0.20	500.
	Pressure - TS3	L	5.22	0.05	500.

TABLE B-16. SHOCK FRONT PRESSURE RATIO DATA FOR SERIES 1.

Station	Location (Meters)	Pressure Ratio (P_{21})				
		Run 5	Run 56	Run 57	Run 58	Run 59
C	0.87	95.	101.	90.	100.	96.
D	2.01					
E	3.20					
F'	3.88					
Roughness Starts	4.00	87.	76.	76.	65.	76.
R1	4.06					
0	4.24					
V2	4.77					
R2	4.81					
F	5.18					
V3	5.71					
R3	5.75					
Load Cell	5.93	60.	64.	64.	42.	46.
G	6.38					
R4	6.69					
R5	7.63					
H	7.66					
R6	8.56					
Roughness Ends	8.80	20.	29.	25.	40.	41.
I	8.88					

TABLE B-17. SHOCK FRONT PRESSURE RATIO DATA FOR SERIES 2.

Station	Location (Meters)	Pressure Ratio (P_{21})		
		Run 10	Run 64	Run 63
C	0.87	105.	116.	112.
D	2.01			
E	3.20			
F'	3.88			
Roughness Starts				
R1	4.00	74.	89.	82.
0	4.06			
V2	4.24			
V2	4.77			
R2	4.81	68.	70.	68.
F	5.18			
V3	5.71			
R3	5.75			
Load Cell				
G	5.93	68.	67.	66. End Wall @ x = 6.29 M
R4	6.38			
R5	6.69			
R5	7.63			
H	7.66	68.	37.	P ₅₁ (Fig. 20)
R6	8.56			
Roughness Ends				
I	8.80			
I	8.88			

TABLE B-18. SHOCK FRONT PRESSURE RATIO DATA FOR SERIES 3.

Station	Location (Meters)	Pressure Ratio (P_{21})		
		Run 7	Run 54	Run 60
C	0.87	376.	377.	376.
D	2.01			
E	3.20			
F'	3.88		314.	282.
Roughness Starts				
R1	4.00			
0	4.06		249.	202.
V2	4.24			
R2	4.77			
F	4.81		233.	201.
V3	5.18	292.		
R3	5.71			
Load Cell	5.75		156.	187.
G	5.93			
R4	6.38			
R5	6.69		134.	128.
H	7.63		80.	107.
R6	7.66	286.		
Roughness Ends				
I	8.56	57.	74.	
	8.80			
	8.88			

TABLE B-19. SHOCK FRONT PRESSURE RATIO DATA FOR SERIES 4

Station	Location (Meters)	Pressure Ratio (P_{21})		
		Run 50	Run 52	Run 61
C	0.87			
D	2.01	635.	726.	826.
E	3.20			
F'	3.88	601.	747.	680.
Roughness Starts				
R1	4.00			
0	4.06		720.	660.
V2	4.24			
	4.77			
R2	4.81		606.	500.
F	5.18			
V3	5.71			
R3	5.75		440.	330.
G	5.77	576.		
Load Cell	5.93			
R4	6.69		230.	296.
R5	7.63		176.	250.
H	7.66			
R6	8.56		83.	163.
Roughness Ends				
I	8.80			
	8.88			

Blank

APPENDIX C

Optical Measurements

This Appendix presents a discussion of an optical investigation into the complex flow about the ribs in a model of the MX trench. Using holographic techniques, a pictorial description of the wave and flow structure has been compiled for various times after shock arrival. Photographs of the holographic images obtained using a variety of methods are included along with a discussion of interferometric density measurements.

An SAI custom built laser holography system was used to record several types of flowfield images including laser shadowgraphy, conventional inline and off-axis holography, and holographic interferometry. For this system, the source of coherent illumination was an Nd:YAG frequency doubled laser emitting 30 millijoules of 5230 Å light in 20 nanosecond pulses.

The optical system is shown schematically in Figure C-1. The holographic camera has the capability of focusing the image of the center of the test section into the hologram plane when laser shadowgraphy is employed; or optionally focusing the image into a plane upstream from the holograph plane when off-axis holography is employed. An optional off-axis reference beam provided the capabilities to perform off-axis holography. The laser was externally spatially filtered to provide a smooth beam, and the entire laser train was rail mounted for stability.

For laser shadowgraphy, a pulse laser provided an adequately short (20 nanosecond) exposure. Although it is not essential to focus an image of the central area of the flow into the film plane, auxiliary optics were used to obtain in-focus images (Figures C-2 thru C-4). These three shadowgrams show the shock as it appears within the window at three different times during the event. The corrugated shock tube walls

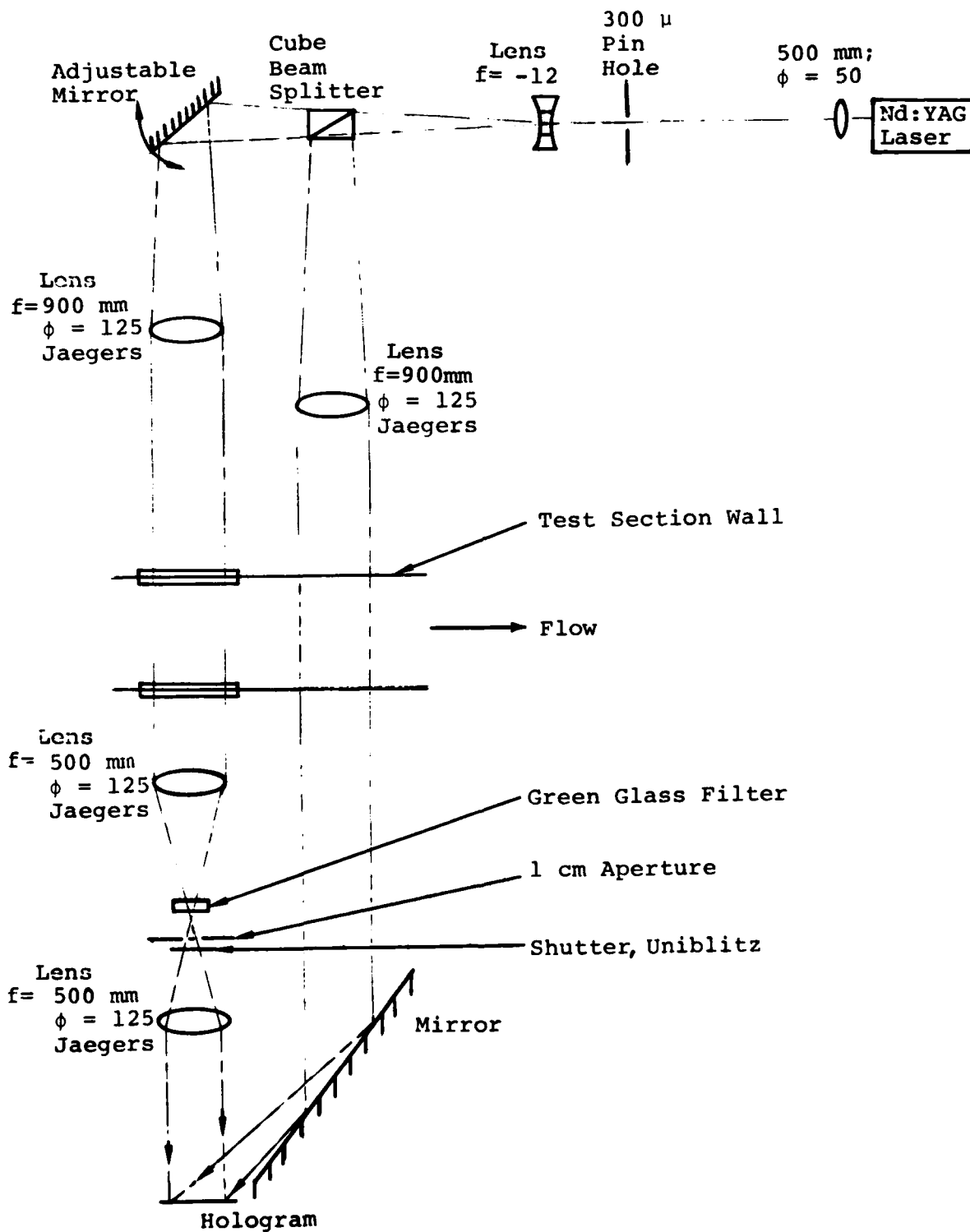


FIGURE C-1. HOLOGRAPHY SYSTEM.



FIGURE C-2. LASER SHADOWGRAPHY (RUN 38, $t = 12 \mu\text{SEC}$).



FIGURE C-3. LASER SHADOWGRAPHY (RUN 37, $T = 48 \mu\text{SEC}$).



FIGURE C-4. LASER SHADOWGRAPHY (RUN 40, $\tau = 176 \mu\text{SEC}$).

evident in the upper and lower portions of the photograph give rise to a complicated, symmetrical, regular, and relatively turbulence free shock structure. The photographs demonstrate that certain gross features of the shock can be obtained with simple laser shadowgraphy.

Laser shadowgraphy can be considered as a form of in-line holography. In-line holography uses a clean reference beam which is caused to interfere with the object transmitted light, and whose propagation direction is identical to the major portion of the object wave (i.e., no offset angle). In the shock tube configuration, the reference wave may be regarded as that portion of the illumination wave undiffracted or otherwise unaltered by the object. If this wave is of significantly greater amplitude at the film plane than the object modified portion of the illumination (a necessity for nonlinear recording), a useful hologram is constructed. An object field containing a dense cloud of particles will not do, nor will one in which the turbulence (through which the illumination beam must pass) is too great. Depending upon the ultimate measurement to be made from the hologram, the results (Figures C-2 through C-4) are either acceptable or unacceptable in line holograms. There are few particles in the field, but there is some turbulence near the tube walls. Upon closer examination, one would find that the illumination wave is diffracted in a complex manner by the shock wave. Another disadvantage in using in-line holograms is that a conjugate image overlaps the desired image when the hologram is reconstructed, thus often contributing to confusion in data interpretation.

The limitations of in-line holography prevent one from using the technique to measure the density profiles within the shock. Such measurements require the recording of the phase of the light for each point across the film plane, so that interferometry may be implemented.

Good quality holography is obtained only when the reference wave is clean. Holograms constructed with an off-axis holography system (Figure C-1) give rise to the reconstructed images shown in Figures C-5 and C-6. These photographs are interesting in that they show how well a duplication of the previous shock phenomena is achieved. They also demonstrate that the photographic plates used to record the events for Figures C-2 through C-4, were somewhat nonlinear when compared with the film results of Figures C-5 and C-6 which lack the contrasting dark and light lines.

Holograms constructed with the present system contain records of both the amplitude and phase of the object wave (the essence of holography), and the reconstructed image waves can be allowed to interfere with a reference wave to create interference fringes. The fringe structure contains information from which can be extracted details about the density for all points within the shock wave. Rather than attempt to carry out this procedure, a second method of interferometry was implemented which has both advantages and disadvantages over this post event method. This second method requires that one record two exposures on the single photographic plate. One of the exposures represents the reference, and thus, the interferometric structure is contained within the single holographic image. An obvious disadvantage of the method is that the interferometric fringe structure is frozen and cannot be altered during the reconstruction and interrogation steps. An advantage is that the effects of the distortions and aberrations caused by the optics in the construction apparatus are automatically cancelled from the resulting fringe structure.

An example of interferometry with zero offset in which the first exposure occurred prior to shock propagation and the second exposure occurred during shock propagation is shown in



FIGURE C-5. LASER HOLOGRAPHY (RUN 47, $\tau = 11 \mu\text{SEC}$).



FIGURE C-6. LASER HOLOGRAPHY (RUN 48, $\tau = 81 \mu\text{SEC}$).

in Figure C-7. The image is of an event which is similar to those of Figures C-2 and C-5. The complicated fringe structure is of such a nature that interpretation is difficult, if not impossible. It is not clear whether adjacent fringes represent regions of falling or rising density. A method which overcomes this problem is the following. Between the first and second exposures, the illumination wave (or alternatively the hologram construction reference wave) direction is slightly altered so that a residual vertical fringe structure overlays the holographic image and reduces the ambiguities. The degree of directional change determines the residual fringe spacing; too great a tilt causes fringes which are too fine to be useful while not enough tilt contributes little to reducing ambiguities. This procedure results in offset fringe interferograms with vertical fringes (Figures C-8 through C-11). Three of these (Figures C-8 through C-10) were recorded at approximately the same relative time as the laser shadowgrams.

Density profiles are derived from the fringe structure by relating fringe shift to index of refraction changes (which for gases is related to the density change). From the Lorentz-Lorenz formula (Reference C-1) the polarizability α of the gas within the shock volume is

$$\alpha = \frac{3}{4\pi N} \frac{n^2 - 1}{n^2 + 2} \quad (C-1)$$

in which the number of molecules per unit volume N and the index of refraction n are introduced. The index of refraction of a gas is close to unity even at high pressures; therefore, Equation C-1 reduces to

$$n - 1 = c\rho \quad (C-2)$$



FIGURE C-7. DOUBLE PULSE LASER HOLOGRAPHY WITH ZERO
OFFSET (RUN 49, $T = 24 \mu\text{SEC}$).

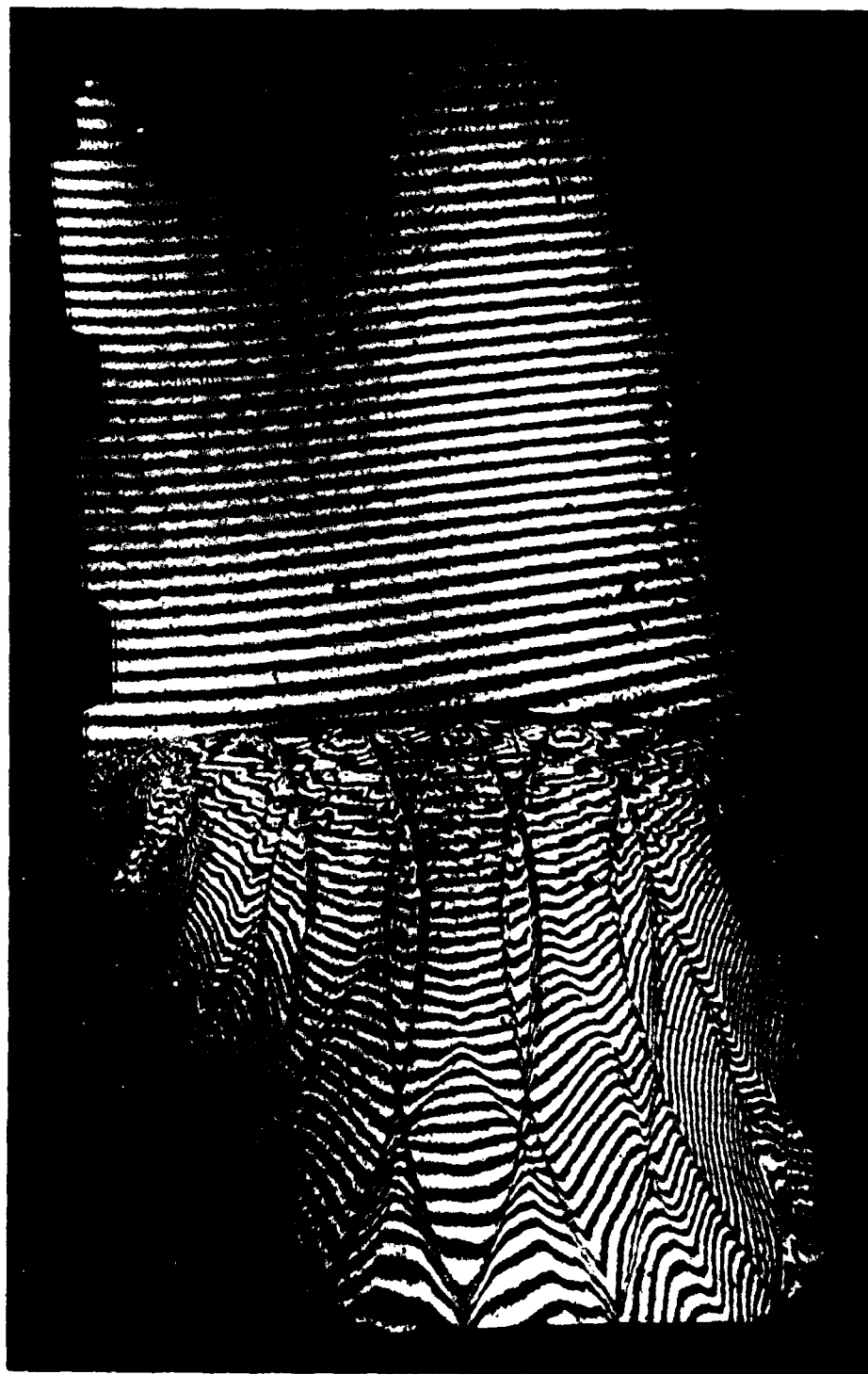


FIGURE C-8. DOUBLE PULSE LASER HOLOGRAPHY OFFSET
FRINGE (RUN 43, $T = 5 \mu\text{SEC}$).

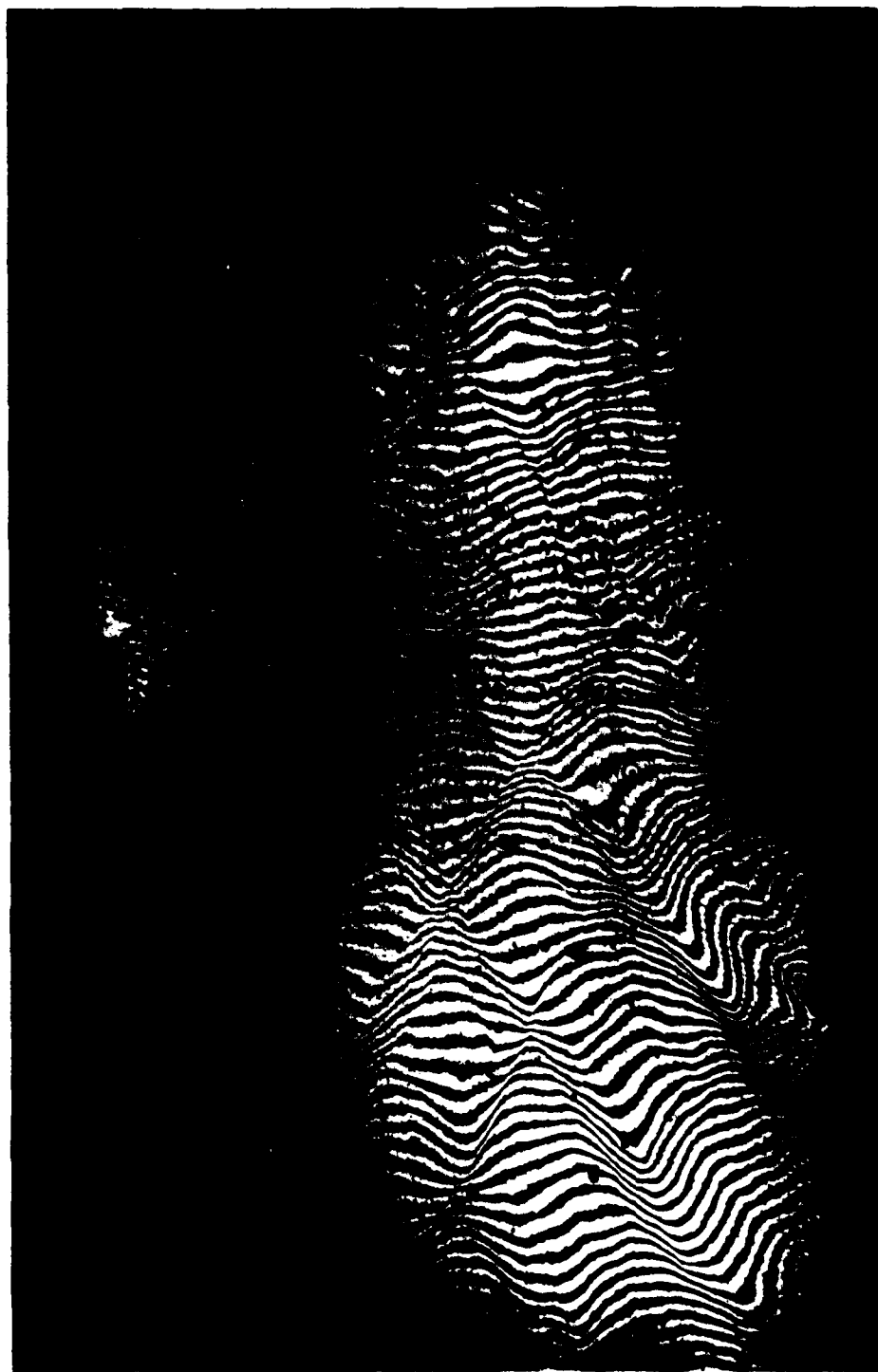


FIGURE C-9. DOURI F PIII SF LASER HOLOGRAPHY OFFSET
FRINGE (RUN 44, $T = 73 \mu\text{SEC}$).

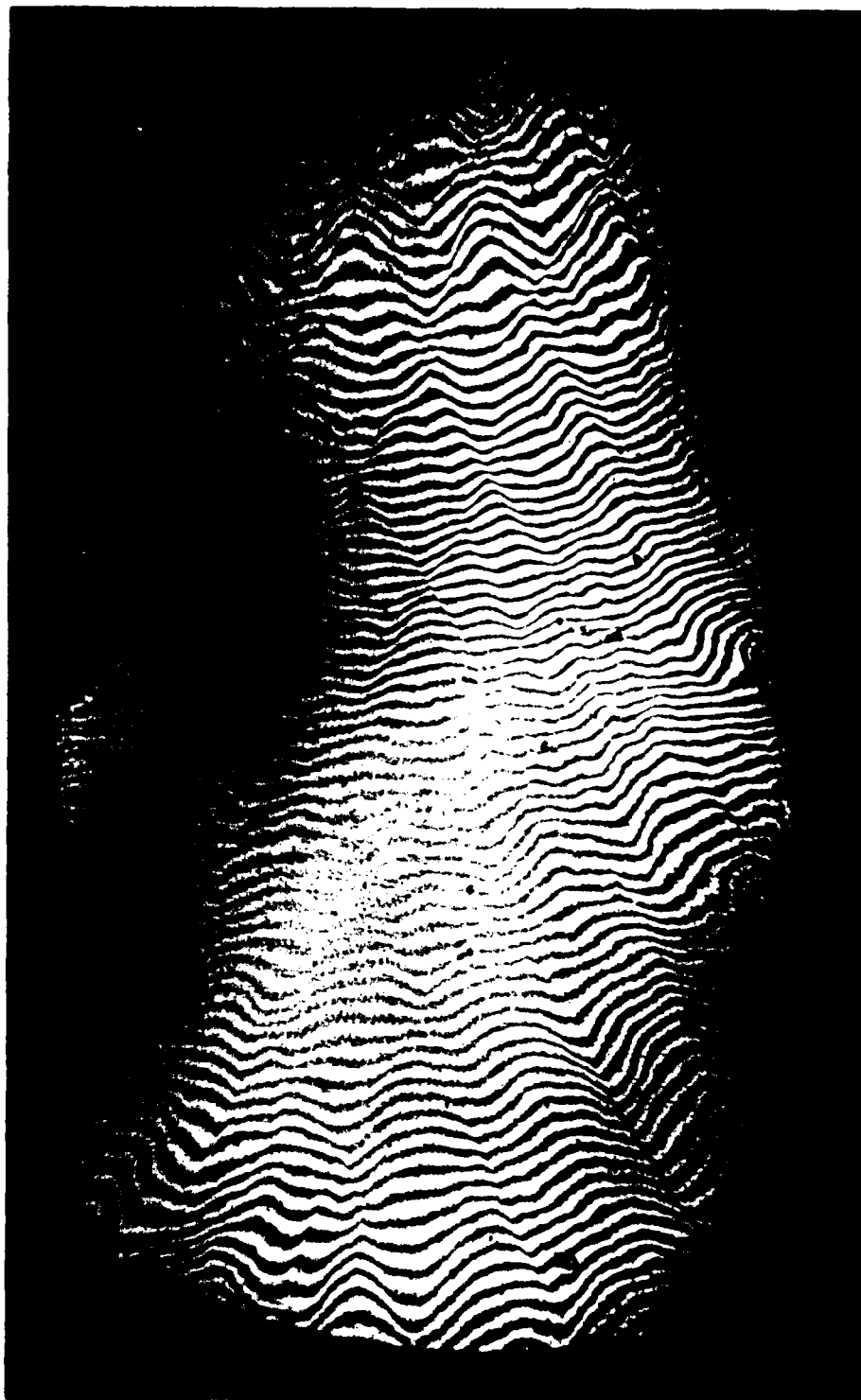


FIGURE C-10. DOUBLE PULSE LASER HOLOGRAPHY OFFSET
FRINGE (RUN 45, $t = 188 \mu\text{SEC}$).



FIGURE C-11. DOUBLE PULSE LASER HOLOGRAPHY OFFSET FRINGE (RUN 46, $T = 341 \mu\text{SEC}$).

in which the density ρ and a proportionality constant c with units of inverse density are introduced.

A nondimensional constant can be introduced by defining a standard density. This number is the familiar Gladstone Dale constant β . Equation C-2 is then

$$n - 1 = \beta \frac{\rho}{\rho_s} \quad (C-3)$$

where $\beta = 2.95 \times 10^{-4}$ and $\rho_s = 1.29 \times 10^{-3} \text{ gm/cm}^3$.

It remains however to relate the index of refraction to the interferometric fringe spacing. In the absence of an offset or tilting between the two exposures (or alternatively when calculating variations in a direction along a linear fringe direction, i.e., top to bottom in Figures C-8 through C-11), the index of refraction variation between adjacent fringes Δn is

$$\Delta n = \frac{\lambda}{D} \quad (C-4)$$

where the test section width D (the mean optical path through the test section) and the wavelength of the laser light λ are introduced.

The density change between adjacent fringes is related to the index of refraction change by

$$\Delta \rho = \frac{d\rho}{dn} \cdot \Delta n = \left(\frac{\lambda}{D\beta} \right) \rho_s \quad (C-5)$$

For these tests, the actual interferometer sensitivity is

$$\Delta \rho = \frac{1}{27.4 \text{ fringe}} \frac{\rho_s}{\text{fringe}} = 4.71 \times 10^{-5} \text{ gm/cm}^3\text{-fringe} \quad (C-6)$$

Density profiles were obtained by counting fringes outwards from the centerline of the test section. The absolute centerline

density was estimated from the shock speed and the initial density to be $9.03 \times 10^{-3} \text{ gm/cm}^3$, and the density profiles are plotted relative to the centerline value (Section 4.5).

REFERENCES

- C-1 "Principles of Optics," Born and Walt, 4th Edition, Pergoman Press, page 8.

Blank

DISTRIBUTION LIST

DEPARTMENT OF DEFENSE

Assistant to the Secretary of Defense
Atomic Energy
ATTN: Executive Assistant

Defense Advanced Rsch. Proj. Agency
ATTN: TIO

Defense Intelligence Agency
ATTN: RDS-3A

Defense Nuclear Agency
ATTN: DDST
ATTN: SPSS, G. Ullrich
ATTN: SPSS, E. Sevin
3 cy ATTN: SPSS, J. Galloway
4 cy ATTN: TITL

Defense Technical Information Center
12 cy ATTN: DD

Field Command
Defense Nuclear Agency
ATTN: FCTMD
ATTN: FCPR

Field Command
Defense Nuclear Agency
Livermore Division
ATTN: FCPRL

Joint Strat. Tgt. Planning Staff
ATTN: XPFS
ATTN: NRI-STINFO, Library

Undersecretary of Defense for Rsch. & Engrg.
ATTN: Strategic & Space Systems (OS)

DEPARTMENT OF THE ARMY

BMD Advanced Technology Center
Department of the Army
ATTN: ATC-T

Chief of Engineers
Department of the Army
ATTN: DAEN-RDM
ATTN: DAEN-RDL
ATTN: DAEN-MPE-T, D. Reynolds
ATTN: DAEN-ASI-L

Harry Diamond Laboratories
Department of the Army
ATTN: DELHD-N-P
ATTN: DELHD-I-TL

U.S. Army Ballistic Research Labs.
ATTN: DRDAR-BLE, J. Keefer
ATTN: DRDAR-TSB-S

U.S. Army Cold Region Res. Engr. Lab.
ATTN: Library

U.S. Army Construction Engrg. Res. Lab.
ATTN: Library

DEPARTMENT OF THE ARMY (Continued)

U.S. Army Engineer Center
ATTN: Technical Library

U.S. Army Engr. Waterways Exper. Station
ATTN: WESSD, G. Jackson
ATTN: Library
ATTN: WESSA, W. Flathau

U.S. Army Material & Mechanics Rsch. Ctr.
ATTN: Technical Library

U.S. Army Materiel Dev. & Readiness Cmd.
ATTN: DRXAM-TL

U.S. Army Nuclear & Chemical Agency
ATTN: Library

DEPARTMENT OF THE NAVY

Naval Construction Battalion Center
ATTN: Code L51, J. Crawford
ATTN: Code LOBA
ATTN: Code L53, J. Forrest

Naval Facilities Engineering Command
ATTN: Code 09M22C

Naval Postgraduate School
ATTN: Code 0142
ATTN: G. Lindsay

Naval Research Laboratory
ATTN: Code 2627

Naval Surface Weapons Center
ATTN: Code X211
ATTN: Code F31

Naval Surface Weapons Center
ATTN: Tech. Library & Info. Services Branch

Office of Naval Research
ATTN: Code 715

DEPARTMENT OF THE AIR FORCE

Air Force Institute of Technology
ATTN: Library

Air Force Systems Command
ATTN: DLWM

Air Force Weapons Laboratory
Air Force Systems Command
ATTN: NT, D. Payton
ATTN: DE, M. Plamondon
ATTN: DED-I
ATTN: DED-A
ATTN: SUL
ATTN: DES-S
ATTN: DES-G
ATTN: DEO
ATTN: DEY

DEPARTMENT OF THE AIR FORCE (Continued)

Assistant Chief of Staff
Intelligence
Department of the Air Force
ATTN: IN

Assistant Secretary of the Air Force
Research, Development & Logistics
ATTN: SAFALR/DEP for Strat. & Space Sys.

Ballistic Missile Office
Air Force Systems Command
ATTN: MNNX, W. Crabtree
ATTN: MNNXH, D. Gage

Deputy Chief of Staff
Research, Development, & Acq.
Department of the Air Force
ATTN: AFRDQA
ATTN: AFRDPN
ATTN: AFRD-M, L. Montulli
ATTN: AFRDQSM

Strategic Air Command
Department of the Air Force
ATTN: XPFS
ATTN: NRI-STINFO, Library

Vela Seismological Center
Department of the Air Force
ATTN: G. Ullrich

DEPARTMENT OF ENERGY CONTRACTORS

Lawrence Livermore Laboratory
ATTN: Document Control for D. Glenn

Los Alamos Scientific Laboratory
ATTN: Document Control for C. Keller
ATTN: Document Control for R. Sanford

Sandia Laboratories
ATTN: Document Control for Org. 1250, W. Brown
ATTN: Document Control for A. Chabai

OTHER GOVERNMENT AGENCY

Federal Emergency Management Agency
ATTN: Hazard Eval. & Vul. Red. Div., G. Sisson

DEPARTMENT OF DEFENSE CONTRACTORS

Acurex Corp.
ATTN: C. Wolf
ATTN: K. Triebes
ATTN: J. Stockton

Aerospace Corp.
ATTN: Technical Information Services
ATTN: H. Mirels

Agbabian Associates
ATTN: M. Agbabian

Applied Theory, Inc.
2 cy ATTN: J. Trulio

Boeing Co.
ATTN: Aerospace Library
ATTN: S. Strack

DEPARTMENT OF DEFENSE CONTRACTORS (Continued)

California Research & Technology, Inc.
ATTN: Library
ATTN: M. Rosenblatt

Civil Systems, Inc.
ATTN: J. Bratton

Civil Systems, Inc.
ATTN: S. Melzer

Eric H. Wang
Civil Engineering Rsch. Fac.
ATTN: J. Kovarna
ATTN: P. Lodde

General Electric Co.—TEMPO
ATTN: DASIAC

H-Tech Labs., Inc.
ATTN: B. Hartenbaum

Higgins, Auld & Associates
ATTN: N. Higgins
ATTN: H. Auld

IIT Research Institute
ATTN: Documents Library

J. H. Wiggins Co., Inc.
ATTN: J. Collins

Merritt CASES, Inc.
ATTN: Library

Nathan M. Newmark Consult. Eng. Svcs.
ATTN: N. Newmark
ATTN: W. Hall

Pacific-Sierra Research Corp.
ATTN: H. Brode

Mission Research Corporation
ATTN: C. Longmire
ATTN: G. McCartor

Pacifica Technology
ATTN: Library
ATTN: R. Allen

Physics International Co.
ATTN: Technical Library
ATTN: J. Thomsen
ATTN: F. Sauer

R & D Associates
ATTN: J. Lewis
ATTN: Technical Information Center
ATTN: C. MacDonald
ATTN: R. Port
ATTN: J. Carpenter

Science Applications, Inc.
ATTN: Technical Library
ATTN: R. Schlaug
ATTN: H. Wilson

Science Applications, Inc.
ATTN: D. Hove
ATTN: E. Craig

DEPARTMENT OF DEFENSE CONTRACTORS (Continued)

Science Applications, Inc.
ATTN: B. Chambers III

SRI International
ATTN: G. Abrahamson
ATTN: Library
ATTN: J. Colton

Systems, Science & Software, Inc.
ATTN: Library
ATTN: J. Barthel
ATTN: K. Pyatt
ATTN: C. Dismukes

Systems, Science & Software, Inc.
ATTN: J. Murphy

Systems, Science & Software, Inc.
ATTN: C. Hastings

Systems, Science & Software, Inc.
ATTN: C. Needham

DEPARTMENT OF DEFENSE CONTRACTORS (Continued)

Terra Tek, Inc.
ATTN: Library
ATTN: A. Abou-Sayed

TRW Defense & Space Sys. Group
ATTN: Technical Information Center
ATTN: N. Lipner

TRW Defense & Space Sys. Group
ATTN: G. Hulcher

Weidlinger Assoc., Consulting Engineers
ATTN: I. Sandler

Weidlinger Assoc., Consulting Engineers
ATTN: J. Isenberg

Blond

